INFORMATION TO USERS

This manuscript has been reproduced from the microfilm master. UMI films the text directly from the original or copy submitted. Thus, some thesis and dissertation copies are in typewriter face, while others may be from any type of computer printer.

The quality of this reproduction is dependent upon the quality of the copy submitted. Broken or indistinct print, colored or poor quality illustrations and photographs, print bleedthrough, substandard margins, and improper alignment can adversely affect reproduction.

In the unlikely event that the author did not send UMI a complete manuscript and there are missing pages, these will be noted. Also, if unauthorized copyright material had to be removed, a note will indicate the deletion.

Oversize materials (e.g., maps, drawings, charts) are reproduced by sectioning the original, beginning at the upper left-hand corner and continuing from left to right in equal sections with small overlaps.

Photographs included in the original manuscript have been reproduced xerographically in this copy. Higher quality 6" x 9" black and white photographic prints are available for any photographs or illustrations appearing in this copy for an additional charge. Contact UMI directly to order.

ProQuest Information and Learning
300 North Zeeb Road, Ann Arbor, MI 48106-1346 USA
800-521-0600

UMI®

Molecular Growth, Aerosol Formation and Pyrolytic Carbon Deposition During the Pyrolysis of Ethane at High Conversion

By

Greg F. Glasier

Submitted in partial fulfillment of the requirements
for the degree of Doctor of Philosophy

at

Dalhousie University
Halifax, Nova Scotia
September 2000.

0-612-66664-6

DALHOUSIE UNIVERSITY

FACULTY OF GRADUATE STUDIES

The undersigned hereby certify that they have read and recommend to the Faculty of Graduate Studies for acceptance a thesis entitled "Molecular Growth, Aerosol Formation and Pyrolytic Carbon Deposition During the Pyrolysis of Ethane at High Conversion"

by Greg F. Glasier

in partial fulfillment of the requirements for the degree of Doctor of Philosophy.

Dated: October 20, 2000

External Examiner

Research Supervisor

Examining Committee

[redacted]

Dalhousie University

Date: 09/07/2000

Author: Greg F. Glasier

Title: Molecular Growth, Aerosol Formation and Pyrolytic Carbon Deposition During the Pyrolysis of Ethane at High Conversion

Department: Chemistry

Degree: Ph.D. Convocation: spring Year: 2001

[redacted]

To Brittany and Norma.

Table of Contents

List of Figures

List of Tables

ABSTRACT

When hydrocarbons are placed in a high temperature environment, energy is introduced into the individual molecules. Redistribution of this energy often results in the "cracking" of C-C bonds, the formation of radicals, and a general reduction in the size of the molecules. A small fraction of these molecules react with one another, growing into large, stable species including carbon. The accumulation of carbon on heated reactor surfaces when in the presence of hydrocarbons is a serious industrial problem. The deposits are complicated, generally containing a number of distinct, carbon-rich materials. Available evidence suggests pyrolytic carbon deposits directly on the reactor surface as a small hydrocarbon or that polymerization and condensation reactions may play an important role. However, there is insufficient evidence to distinguish which mechanisms dominate. This thesis examined the role of molecular growth and aerosol formation in carbon formation during the pyrolysis of ethane.

New sampling techniques were developed and used to obtain samples from a flow reactor for the pyrolysis of ethane at 1185 K. Gaseous samples were analyzed by gas chromatography and mass spectrometry. Liquid samples were analyzed by gas chromatography, liquid chromatography and mass spectrometry. Solid samples were analyzed *in-situ* by gravimetric analysis and externally by electron microscopy. Aerosols were analyzed *in-situ* by laser extinction and externally by electron microscopy.

Gas phase analyses were consistent with three acetylene molecules reacting to form benzene. The rate of carbon deposition was found to be directly proportional to the concentration of benzene in the system. Aromatic species were observed in the 100-700 amu range. The observation of these species was consistent with the hypothesis that polycyclic aromatic hydrocarbon (PAH) condensation and dehydrogenation were partially responsible for the deposition of carbon. These results also indicated that there were sufficient PAHs present in the system to allow for formation of the observed amount of carbon by one or both of the following routes: direct decomposition on the surface from the gas phase or condensation as a liquid followed by deposition. It was shown for the first time that ethane can also be transformed in part, at high temperatures and long residence times, to form an aerosol. These results were consistent with the presence of a carbon precursor which was neither a discrete aromatic unit nor a soot particle but had a structure that was somewhere in between. The study indicated that 30 % of the deposited carbon in the ethane pyrolysis system could have been due to deposition of the observed aerosol.

Metal surfaces were shown to initially accelerate deposition, indicating a surface catalyzed decomposition. This acceleration was shown to level off after a short period of coking. The reduction in rate was correlated to a change from filamentous carbon to pyrolytic carbon, indicating the carbon precursors examined in this study are also relevant to coking in industrial metal reactor tubes.

Acknowledgments

I wish to thank Dr. P. D. Pacey for his valuable advice, constant encouragement and patience throughout this work. His commitment to the education of his students is only surpassed by his knowledge of the field of chemical kinetics.

I would like to thank Dr. S. Dimitrijevic for his help in setting up the apparatus and many useful conversations on the subject of carbon formation.

I would also like to thank Dr. Hiroshi Furue for his help and patience throughout this work.

I would like to thank Rana Filfill for her help in the analysis of liquid products. Rana's long hours spent in front of the LC were greatly appreciated.

Thanks to Dr. L. Ramaley for his assistance with mass spectrometry and the use of equipment.

Special thanks to Dr. Robert Guy for his help in the identification and analysis of liquid products. The time spent in analyzing the compounds and training both Rana and I in the use of his equipment is gratefully acknowledged.

I wish to thank the Faculty of Graduate Studies, Dalhousie University and the Walter P. Sumner foundation for financial assistance.

Thanks to Imperial Oil for their generous contributions, which helped to start this work, and their renewed financial support, which will help continue it.

1. Introduction

1.1 Introduction to Thermal Processes and Carbon Formation

Thermal processes have been used for making the chemical building blocks ethylene, propylene, butenes, butadiene, and aromatics since the petroleum industry began. When hydrocarbons are placed in a high temperature environment, energy is introduced into the individual molecules. Redistribution of this energy often results in the "cracking" of C-C bonds, the formation of radicals, and a general reduction in the size of the molecules. A small fraction of these molecules will react with one another, growing into large, stable species including carbon. Ever since the pioneering work of Parker and Wolfhard, Grisdale and others (1-3), there has been discussion about the nature of the chemical pathway leading at high temperatures from small gaseous hydrocarbons to solid carbonaceous products. Some suggest the source of solid carbon is small hydrocarbons such as acetylene or polyynes ($C_{2n}H_2$) (3, 4); others say it is formed from large stable polycyclic aromatic hydrocarbons (PAHs) (5-9).

Ascertaining the nature of the precursors to carbon is important. It is suspected that precursors to carbon are formed in fuel-rich regions of combustion systems. Therefore the processes resulting in particulate carbon formation during pyrolysis may also be important in soot formation during combustion. Carbon formation robs combustion systems of their optimal energy efficiency. If the carbon particles escape from the combustion system, soot is formed, which can deposit and disturb natural systems (10). Soot also affects the planetary energy balance (10). Carbonaceous solids observed in interstellar space are thought to be formed in outflows from giant stars in a similar process (11). In the commercial production of carbon black (12) and in the chemical vapour deposition of carbon coatings on or in solid objects (13,14), carbon formation from hydrocarbons at high temperatures is necessary and desirable. Thus, the investigation of the formation of carbon at high temperatures is associated with a number of fields, including combustion chemistry, environmental and atmospheric chemistry, astronomy and chemical engineering.

The accumulation of carbon on reactor surfaces when heated in the presence of hydrocarbons is a serious industrial problem. The deposits are complicated, generally containing a number of distinct, carbon-rich materials. These materials have been grouped under a number of headings: particulate carbon or soot, metal catalyzed carbon or catalytic coke and amorphous or pyrolytic carbon (18-24). Particulate carbon or soot is formed by homogeneous nucleation and growth of carbon particles in the gas phase and may deposit on reactor surfaces or be removed in the gas stream. Metal-catalyzed carbon formation, in which the reactor material catalyses the formation of carbon, is important in coke formation on metal surfaces. Metal-catalyzed carbon results in the formation of a number of structures, including tubes and platelets of various shapes and sizes, growing from a metal crystallite. Amorphous or pyrolytic carbon does not depend on the substrate. Available evidence suggests either that pyrolytic carbon deposits directly on the reactor surface as a small hydrocarbon or that polymerization and condensation reactions may play an important role. However, there is insufficient evidence to distinguish which mechanism may dominate.

This thesis will examine the role of molecular growth and aerosol formation in carbon formation during the pyrolysis of ethane. In the following literature summary certain aspects of the mechanisms of formation and surface structure of each of these forms of carbon will be examined in order to consider their relationship to pyrolytic carbon and coke formation. Consideration of each of these vast topics would require more space than is reasonable and only certain aspects of metal-catalyzed and particulate carbon formation will be considered. Initially the pyrolysis of ethane and pyrolytic carbon formation will be addressed. Next relevant work from the field of combustion and soot formation will be discussed. Finally, the relationship between metal-catalyzed coke and the deposition of pyrolytic carbon will be considered.

1.2 Ethane Pyrolysis and Carbon Formation

The pyrolysis of ethane is an important industrial process (15-17). In the industrial steam cracking of ethane to produce ethylene, carbon or coke forms deposits on the walls of reacting tubes, limiting heat transfer and ultimately blocking flow (15-18). It is estimated that more than 25 billion kilograms of ethylene are produced annually in the United States and world production reached 56 billion kg in 1999 (16, 17). Assuming undesirable by-products constitute even a small fraction of the total products, this results in a large economic and environmental problem. It is important to investigate and understand the formation of carbon in order to optimize the industrial process.

The early stages of the gas phase pyrolysis of ethane and of its principle product, ethylene, have been investigated thoroughly (28-31). The main features of the pyrolysis at low conversion are consistent with the long-chain free-radical mechanism shown below (reactions 1-1 to 1-12).

$$C_2H_6 \rightarrow 2CH_3 \tag{1-1}$$

$$CH_3 + C_2H_6 \rightarrow CH_4 + C_2H_5 \tag{1-2}$$

$$C_2H_5 \rightarrow C_2H_4 + H \tag{1-3}$$

$$H + C_2H_4 \rightarrow C_2H_5 \tag{1-4}$$

$$H + C_2H_6 \rightarrow H_2 + C_2H_5 \tag{1-5}$$

$$CH_3 + H_2 \rightarrow CH_4 + H \tag{1-6}$$

$$H + C_2H_4 \rightarrow C_2H_3 + H_2 \tag{1-7}$$

$$C_2H_3 \rightarrow C_2H_2 + H \tag{1-8}$$

$$CH_3 + CH_3 \rightarrow C_2H_6 \tag{1-9}$$

$$CH_3 + C_2H_5 \rightarrow C_3H_8 \tag{1-10}$$

$$CH_3 + C_2H_3 \rightarrow C_3H_6 \tag{1-11}$$

$$2\,C_2H_5 \rightarrow C_4H_{10} \tag{1-12}$$

There is insufficient experimental data regarding carbon formation in this system (18-24). Numerous studies involving the inhibition of coke formation on metal surfaces have been performed (18-27). Researchers have shown that metal surfaces enhance coke formation but deposition is also significant on inert surfaces (20-24). This study will focus on the formation and inhibition of carbon on a quartz surface.

Previous studies of the pyrolysis of other hydrocarbons, during the formation of pyrolytic carbon, show the products are complex combinations of gaseous and liquid hydrocarbons as well as various solid products composed primarily of carbon (3, 19-23, 32-53). A fundamental problem in the formation of carbon from gases is the elucidation of a mechanism whereby reactant molecules containing only a few carbon atoms are converted into carbon-rich solids which contain tens or hundreds of thousands of carbon atoms and relatively little else (36). In this context the term carbon is used to describe a wide variety of solid materials, which may or may not contain appreciable amounts of hydrogen. The properties of the material change markedly with the conditions of formation (3, 13, 14, 34, 39, 44, 49, 54). One of the most important differences depends on whether carbon is formed in a homogenous vapor phase reaction (soot, particulate carbon, carbon black) or is deposited on solid surfaces that may be present in the reaction zone (coke, pyrolytic carbon) (3). The term pyrolytic carbon (*pyc*) will be used to refer to the collection of carbon rich species which are deposited on surfaces. Gas phase or particulate carbon will refer to carbon formed in the vapor phase and soot will refer to the to particulate carbon formed during combustion. The word carbon will be used as a general term for all species.

Over the past thirty years many studies of the formation of *pyc* have been performed during the pyrolysis of gaseous and liquid hydrocarbons. The complex process leading to carbon may involve series of parallel and consecutive homogeneous gas phase reactions, heterogeneous reactions, physical condensation and dehydrogenation of the carbon rich solid product (3, 18-23, 32-57, 76). The mechanisms leading to carbon formation and the key intermediates involved are still the subjects of controversy. Some authors suggest that the mechanisms leading to carbon formation differ depending on the conditions of pyrolysis (temperature and pressure, starting material and extent of conversion) (3, 34-37).

Many studies have attempted to correlate pyrolysis conditions and starting material with the structure of the solid carbon product (3, 39, 44, 47, 54). While this reasoning has been useful in developing carbon materials it has not proved successful in establishing mechanisms for carbon formation during pyrolysis. Other studies have attempted to correlate initial hydrocarbon partial pressure directly to deposition rate (56, 59-67). More recent studies have attempted to correlate liquid and gas phase products of pyrolysis to the rate of carbon formation or to the structure of the final product (13, 14, 34, 36-38, 40, 42, 46, 48-53). In most cases particular aspects of the reaction systems were studied and complete mass balances were not attempted. The relationship between molecular growth and carbon formation has been examined for combustion systems (68-103), but has not been adequately addressed for the pyrolysis of small hydrocarbons.

The formation of carbon in the gas phase has received much attention. However with respect to carbon formation on surfaces, very little has been reported that could give a quantitative description of the phenomenon or explain the mechanism. In the early years, many qualitative chemical models describing mechanisms of carbon formation were suggested and were summarized by Palmer (3). The purpose here is not to consider all these in great detail, but only those that may be directly relevant to industrial steam cracking and those which are consistent with more recent results.

Two basic ideas are relevant to carbon formation during the industrial steam cracking of ethane: hydrocarbon polymerization theories and surface decomposition theories. Hydrocarbon polymerization theories are all variations on the theme that polymerization of the hydrocarbon or some product of the pyrolysis occurs, followed by dehydrogenation, with solid carbon being the end product. Various species, including acetylene and a number of aromatics, have been suggested as key intermediates in the process. The essence of the acetylene polymerization theory is that hydrocarbon fuels are initially degraded to acetylene and that carbon is formed from acetylene by simultaneous polymerization and dehydrogenation. There is evidence indicating higher molecular weight hydrocarbons with acetylenic bonds are important precursors to gas phase carbon formation during very high temperature combustion (3,4). However, there is no evidence to indicate acetylenic compounds are fundamental in the lower temperature pyrolysis of hydrocarbons (3,55) and in fact aromatics appear more important in pyrolysis (33, 36-41). In pyrolysis acetylenic compounds may be reactive intermediates which do not build up to measurable yields but which provide a route to carbon formation (38, 55).

The surface decomposition theory suggests carbon particle growth occurs through direct decomposition of hydrocarbons on the surface. Tesner has been the principal advocate of the surface decomposition model (56). Recently, Huttinger and coworkers have also suggested that the products of pyrolysis decompose directly on the carbon surface (46, 50-53).

Tesner and coworkers have made more strenuous efforts than any other researchers to measure the kinetics of carbon deposition and particle growth. They have performed many pyrolysis experiments involving the flow of gases through heated cylindrical reactors packed with various materials including carbon felts and quartz fibers (56). Commonly, they worked with temperatures of 700-1200°C, at low conversions of reagent to products, with high surface to volume ratios, and under conditions where laminar flow was not possible (56). They have studied the decomposition of numerous hydrocarbons including methane (59, 61), ethane (56), ethylene (60), acetylene (61, 62), propylene (63), butadiene (64), benzene (64-66), toluene (66) and others (56). Generally, they reported that the rates of carbon formation were directly proportional to the initial concentration of the hydrocarbon pyrolysed. They assumed that homogeneous gas phase reactions were not significant and that direct decomposition of the hydrocarbon reactant dominated the deposition process. A model based on a Langmuir isotherm with competitive inhibition by hydrogen was applied (56).

Subsequent work performed by Benzinger, Becker and Huttinger (BBH) (13, 46, 50-53), under conditions of low surface area and laminar flow, showed that the rate of pyrolytic carbon deposition was not directly proportional to the initial concentration of the reagent. Close examination of Tesner's results also reveals that in many experiments first-order kinetics was not observed. Certainly for the pyrolysis of acetylene, where rates increased exponentially with increases in initial concentration (61), and methane (67), where an exponential decrease in rate was observed, the oversimplified assumption of first-order kinetics was not justified.

BBH (13, 46, 50-53), measured deposition rates and yields of gaseous products during the pyrolyses of methane, ethylene, acetylene and benzene. They found the deposition rate was directly proportional to the concentration of the reactant hydrocarbon for benzene pyrolysis, but in all other cases deposition rates were not directly proportional to the concentration of the reactant hydrocarbon. This study contradicted some of Tesner's (56) results and confirmed the work of Lahaye and Prado (36,37). It is difficult to rationalize how these experiments, performed under apparently similar conditions, provided different results. One simple explanation could be related to the large surface area present in the reaction zone in Tesner's work. BBH developed and tested a model including the decomposition of pyrolysis products as well as that of the initial reactant. This description considered the complex, gas-phase chemistry (50-53). In this model a seven-parameter equation, fit to the two observables, R_c and residence time (50-53), was used to quantitatively describe the deposition rate, R_c. Their work indicated that direct decomposition of the original hydrocarbon is likely important at low conversions of reactant to products but, as more products are formed, R_c is a complex function of the concentrations of many products.

In an early study, Pierson and Leiberman correlated pyrolysis products with the structure of the *pyc* deposited, and obtained an empirical correlation between the structure of the solid carbon product and the acetylene/benzene ratio (a/b) in the hydrocarbon product (34). Furthermore, Pierson and Leiberman developed a thermodynamic model empirically relating a/b to the structure (34). Unfortunately, this result was virtually ignored until recently, when Benzinger *et al.* (42) suggested a rationale for the a/b correlation and Lewis *et al.* (45) applied a similar model to describe a chemical vapor infiltration system. Lewis *et al.* (49) and Benzinger *et al.*(46) argued that the assumption of thermodynamic equilibrium may not be warranted under these conditions and that consideration of the kinetics is of particular importance. Benzinger and Huttinger (13) and others (13, 14, 49) also applied direct decomposition models in order to rationalize the observation of changes in the carbon microstructure with the gas phase product composition. Changing microstructures were rationalized on the assumption that, under certain conditions, chemisorption of small gaseous species is important and under different conditions, deposition of heavy polymeric species dominates. However, in most pyrolysis work, the existence of high molecular weight species was not established, let alone the relative proportions of these species.

Palmer summarized studies which argued that polymerization reactions produce polycyclic aromatic hydrocarbons (PAHs) as intermediates in carbon formation (3). It was suggested that the initial hydrocarbon was transformed by gas-phase reactions into macromolecules, PAHs. The size of the molecules was postulated to be large enough that their vapor pressure was low, even at high temperatures (38). As a result, PAHs may have existed in the reactor as liquid droplets, which may have converted into carbon in the gas phase or on the surface (37). There have been several suggestions as to how this increase in molecular size may occur (33, 57). The easiest way to envision the reaction is in terms of Diels-Alder reactions. However, this is probably too simplistic a picture to account for the total production of aromatics.

A key intermediate, about which there is still much controversy, is the precursor to solid carbon, formed by condensation of gaseous hydrocarbons, but which has not yet progressed to carbon. In an early study, Grisdale (2) reported evidence for the condensation theory. In this work, carbon was deposited onto silica spheres in a rotating furnace by pyrolysing methane at 1272 K. Electron microscopic images of the edges of the silica substrates indicated the presence of agglomerates or chains of carbon spheres attached to a smooth layer of *pyc* covering the silica surface. The fact that these species were not observed upon tumbling during pyrolysis was stated to indicate these species were fluid. It was also stated, "The droplets create an opaque fog over most of the coating zone cross section in the pyrolyzing furnaces when the hydrocarbon concentration is high.". However, whether this fog was present in the hot zone or could have occurred in cool regions of the furnace is not clear from this work.

Fogs have been observed in the exit channels of pyrolysis reactors at low or intermediate temperatures (32, 36), but these fogs were reported to be absent in the hot zone, and could have been formed at the exit by the sudden chilling of the gases. More recent transmission electron microscopic images have indicated the presence of agglomerates and chains of carbonaceous materials in the pyrolysis zone, but these species have generally been associated with particulate carbon, not a precursor material. Most recent studies of precursor material have involved studies of soot formation in flames and will be discussed in section 1.3.

In a study involving the thermal decomposition of benzene at 1373 K, Lahaye and Prado (35) measured the yields of carbon and liquid products as a function of the reaction time. It was observed that the liquid yields reached a maximum at the beginning of the formation of gas-phase carbon and rapidly decreased thereafter. Based on this observation and speculation from previous work (33, 36), Lahaye and Prado (36) suggested that liquid products of high molecular weight were precursors to solid carbon.

Chen and Back studied the pyrolysis of methane in a static reactor at 1118 K and considered the yield of products as a function of time (38). The method of analysis permitted the measurement of products covering a range from ethane to fluoranthene. They showed that the growth of carbon was very rapid and tended to reach a constant rate at the same time as the higher aromatic products passed through a maximum in yield. This result was supported by the later work of Lucas and Marchand (40) and led to the conclusion that carbon is the final stable product in a series of consecutive and parallel reactions in which aromatic intermediates reach steady-state or maximum values. It was suggested, on the basis of an exponential relationship between the number of carbon atoms in a product molecule and the time required for its formation, that the rate of growth was proportional to the number of carbon atoms in the molecule, which in turn suggests molecular addition processes involving large molecules (39). A possible mechanism for the formation of benzene was the Diels-Alder condensation of ethylene and butadiene to form cyclohexene, followed by rapid elimination of hydrogen to form benzene. An estimate of this rate showed it was too slow to account for the quantities of benzene formed and it was concluded that radical processes were more important in the formation of benzene. This is consistent with other work (57).

Studies of electron micrographs of carbon deposits also supported the theory of carbon formation through the nucleation of small liquid droplets of aromatic compounds followed by dehydrogenation and deposition on the surface (18, 20, 37, 39, 41, 47). Chen and Back (38) took an empirical approach to test the validity of this hypothesis. The amount of liquid material required to account for the yield of carbon observed was estimated. An estimate was made of the size of the molecules expected to form liquid droplets at the temperature of the reaction vessel. An empirical relationship was established between the vapor pressures of PAHs and the temperature. By extrapolation it was shown that molecules having sixty or more carbon atoms could account for the observed yields of carbon. From the empirical relation between the molecular weight of the product and the time required for its formation, it appeared that molecules of molecular weight sufficiently high to condense to liquid droplets could have formed during the time interval of the reaction. This approach was admittedly approximate, nevertheless the results of Back's study were consistent with the liquid droplet theory suggested previously (3).

Blekkan *et al.* studied the pyrolysis of methane at 1473K in a tubular flow reactor (41). The study provided semi-quantitative data for one of the most thorough analyses of liquid products from pyrolysis. The results indicated benzene, naphthalene, anthracene, phenanthrene, acenaphthylene, pyrene, and fluoranthene were the most important constituents in the liquid products; this was consistent with the work of Chen and Back (38) and Lucas and Marchand (40). Minor components included five- and six-ring condensed aromatics. This provided evidence supporting the idea that the aromatics build further in size during pyrolysis.

Murphy *et al.* reported that the composition of PAHs in the pyrolysis product mixture was independent of the hydrocarbon reactant (42, 48). They suggested that PAHs are formed parallel to carbon and that they result from the adsorption and polymerization of acetylene molecules on the carbon surface, followed by cyclization and desorption to form the large aromatics found in the gas phase.

In an attempt to study the early stages of particulate carbon formation during the pyrolysis of allene, Pfefferle *et al.* used a microjet reactor coupled to a vacuum-UV photoionization time-of-flight mass spectrometer (49). When the temperature was increased from 300 to 1200 K, species lighter than 100 amu were observed in a few milliseconds. Increasing the temperature and reaction time to 1495 K and 6 s resulted in the formation of multiple ring aromatics. Growth in the 150- to 350-amu range was consistent with successive acetylene addition to PAH radicals, whereas a few species observed in the 400 to 600 amu range were attributed to the dimerization of smaller PAH radicals. This study is interesting because it indicates the presence of large aromatic species in a pyrolysis system. However, the results indirectly support the direct decomposition model, since large aromatics were not observed at the lower temperatures (< 1200 K) associated with *pyc* formation.

1.3 Combustion and Particulate Carbon Formation

The formation of large PAHs has been investigated thoroughly in combustion systems and here molecular growth and carbon formation have been well documented. In combustion systems, the most highly developed theory argues that soot is formed from PAHs (5-9). It is postulated that a hydrocarbon fuel breaks down to form free radicals, which react according to a chain mechanism. Hydrocarbon radicals with at least six consecutive carbon atoms can cyclize to form a phenyl radical, which can then add to an unsaturated hydrocarbon to form a larger aromatic compound, such as styrene or phenylacetylene. Further addition, abstraction and dimerization steps can lead to larger, fused-ring aromatic compounds, like naphthalene, phenanthrene, pyrene, etc. Ultimately, the partial pressure of heavy PAHs could exceed their equilibrium vapour pressure, and the PAHs could begin to condense as liquid droplets or as solid particles. If ions are present, the condensation could be assisted by charge-induced-dipole forces. Further reactions of consolidation and dehydrogenation could occur in the liquid droplets to transform them into soot or carbon black particles.

Various aspects of this mechanism have been tested, but others remain unconfirmed. Some radicals have been detected in hydrocarbons at high temperatures (68-70). Rate constants for some reactions have been measured experimentally and others have been calculated theoretically (8, 71, 72). PAHs are observed as intermediates and as ultimate products (73-75). Models have been simulated by computer and the results have been compared to experimental measurements of soot production (58,76-77).

Frenklach *et al* developed a detailed kinetic model of gas phase carbon formation under conditions used in the shock tube pyrolysis of acetylene, at temperatures between 1200 and 2500 K (57,71). The objective of their study was to discover the main chemical reaction pathways to gas phase carbon by investigation of a detailed kinetic model and by comparing the results to experimental work (78). The reaction mechanism developed consisted of three components, a set of reactions describing acetylene pyrolysis, a set of reactions describing the formation of larger radicals, and a description of the further growth of aromatic rings. Approximately 600 elementary reversible reactions involving 180 species were considered in the original study (57). The acetylene pyrolysis model was based on the experimental work of Tanzawa and Gardiner (79). In the original model, rate coefficients were taken from experiment when possible and approximated by reasonable upper limits based on collision theory when necessary. Group additivity methods were used to estimate a large fraction of the necessary thermodynamic data (80).

It was initially hypothesized that twenty-six different cyclization pathways would account for the overall cyclization rate. The computational results indicated one pathway dominated for the formation of the first aromatic ring. The mechanism shown in Figure 1-1 indicated that a series of addition and abstraction reactions involving acetylene and hydrogen resulted in the formation of a 1-buten-3-yn-1-yl radical which subsequently reacted with acetylene and cyclized to form the phenyl radical. Under certain conditions addition of acetylene to vinyl acetylene was also shown to be important.

It was found that a single route, shown in Figure 1-2, appeared to dominate formation of the second ring. The addition of phenyl to acetylene led to a 2-phenylvinyl adduct. Hydrogen elimination from the energized adduct, followed by hydrogen abstraction to produce 2-ethynylphenyl and subsequent addition of acetylene followed by cyclization, resulted in the formation of 1-naphthyl.

It was postulated that the reaction kinetics of larger PAHs were analogous to phenyl. As indicated in Figure 1-3, growth could occur through a series of steps involving acetylene addition to form substituted, fused PAHs. These could be reactivated by hydrogen abstraction. This alternating H abstraction, C_2H_2 addition (HACA) route resulted in successive growth of large PAHs. The unsubstituted, fused molecules, like pyrene, were considered to be relatively unreactive side products. Computational results also indicated that the addition of acetylene to the 1-naphthyl radical may have been responsible for the production of five-membered ring aromatic species, such as acenaphthalene. Subsequent reactivation of acenaphthalene by hydrogen abstraction was also considered a reasonable route to PAH growth.

Although in Figure 1-3 the pathway stops at pyrene and cyclopenta[cd]pyrene, both routes were continued in the computer experiments to benzo[ghi]perylene, which was followed by the formation of coronene. It was assumed that further growth of the fused PAHs proceeded in a similar manner. For modeling purposes, gas-phase carbon was arbitrarily chosen as a collection of species above a certain size. This list of species was arbitrarily chosen to begin at coronene.

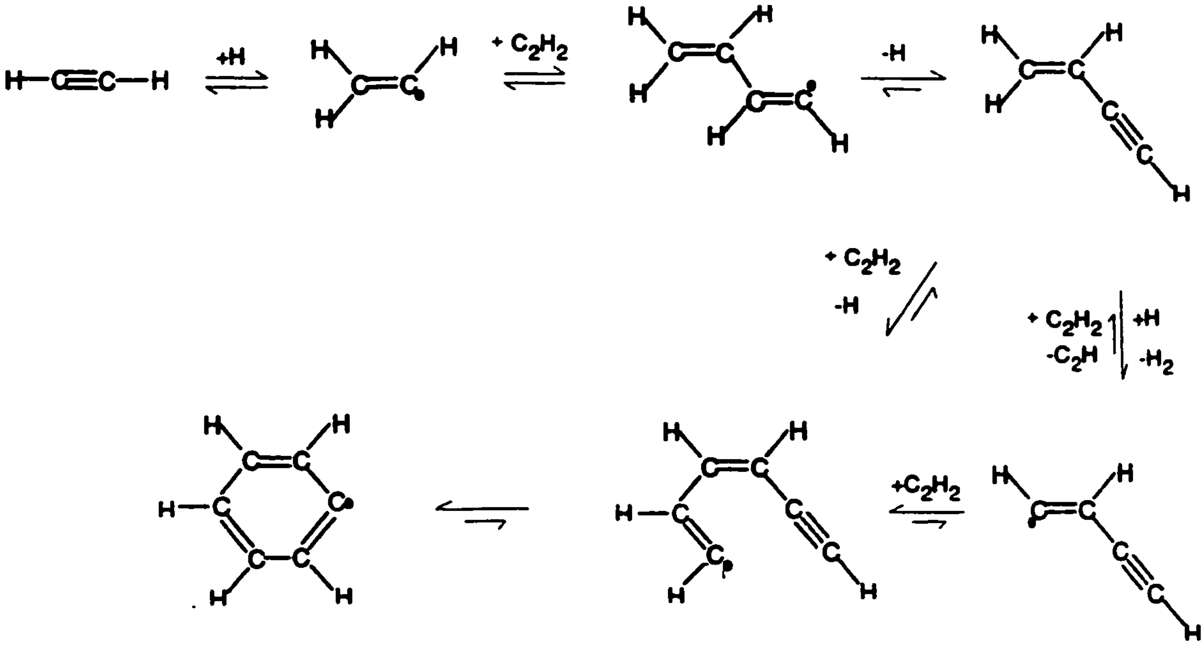

Figure 1-1: Schematic diagram of the principle reaction pathway for the formation of the first aromatic from Reference 57.

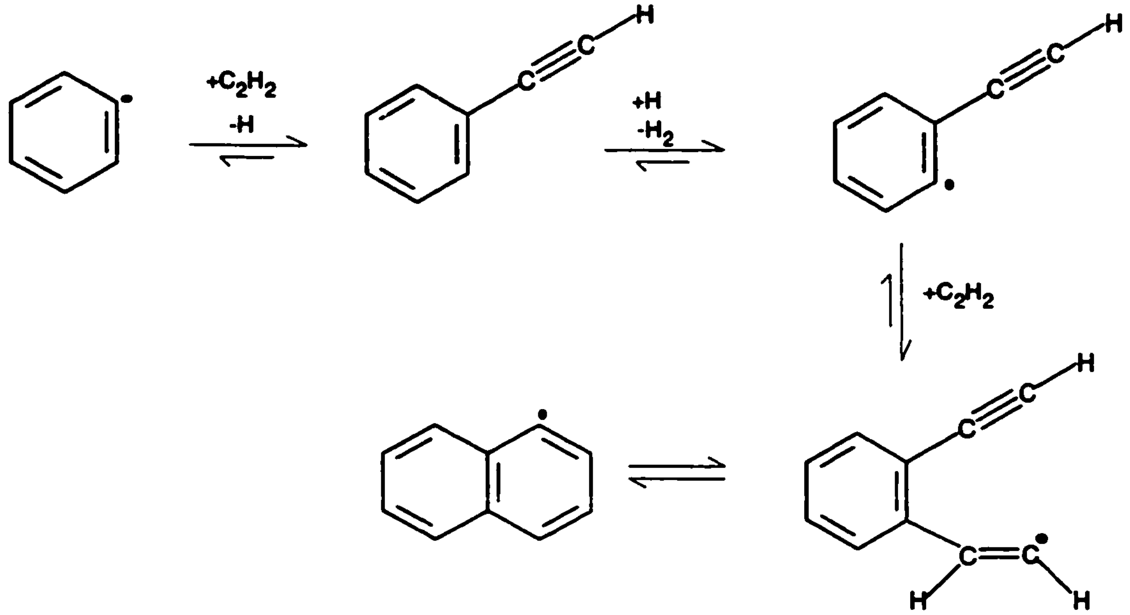

Figure 1-2: Principle reaction pathway for the formation of the second ring from Reference 57.

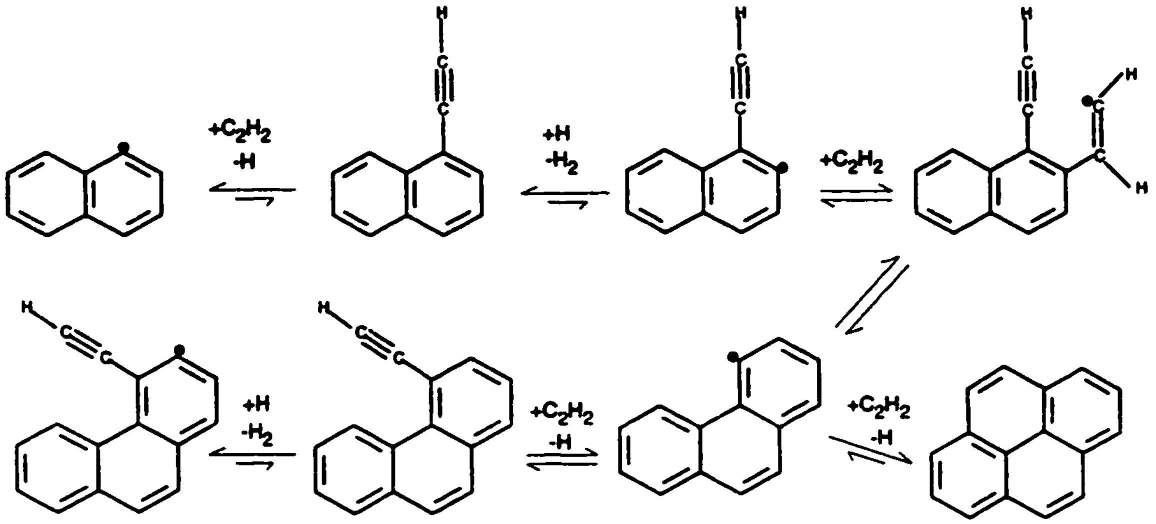

Figure 1-3: Hypothetical reaction pathway for the formation of PAHs from Reference 57.

The model was in qualitative agreement with experimental results, in that it predicted an induction time for carbon formation and that, as temperature increased, the carbon yield reached a maximum and then decreased. At low temperatures, the model predicted the pyrolysis reactions were rate controlling and as the temperature increased the thermodynamic stability of small aromatic radicals decreased and eventually limited the carbon yield. The computational results indicated the formation of the first aromatic ring was the bottleneck for the growth rate of PAHs. In later work Frenklach *et al.* considered the driving force for PAH production (81). They hypothesized two kinetic factors were responsible for the forward flux - irreversible formation of particularly stable PAHs and reactivation of aromatic molecules by hydrogen abstraction. In this work he stressed the importance of the hydrogen concentration in the inhibition of PAH formation. Frenklach's later work involved modeling of the pyrolysis of other compounds, including benzene, 1,3-butadiene, and ethylene (82). In all hydrocarbons, considered the pathway leading to large PAHs was the acetylene-addition mechanism presented in Figure 1-3.

This model was later tested by performing more rigorous calculations (71) and modeling combustion systems (78). The purpose of the later work was to systematically investigate the reaction of acetylene with a series of single- and multi-ring aromatics. The analysis was performed by employing semi-empirical and *ab initio* calculations to obtain the molecular geometries and vibrational frequencies and then by rate coefficient calculations, based on unimolecular Rice-Ramperger-Kassel-Marcus theory. The calculated rate coefficients were calibrated against experimental data when available. These calculations supported the hypothesis that reactions of multi-ring aromatics are, in principle, similar to those of benzene and phenyl. This approach did not really affect the basic conclusions of Frenklach's early work but did alter some of the specific rate constants chosen in Frenklach's original model.

There is some controversy regarding the actual route to aromatics in acetylene pyrolysis. The rate of benzene formation has been shown experimentally to be third order with respect to the acetylene concentration. Kern and Chen suggested one of the more efficient pathways to benzene involves reactions of the propargyl radical, C_3H_3 (83). Others, on the basis of shock tube experiments, have proposed a 1,3-butadienyl ($1\text{-}C_4H_5$) pathway (82). Westmoreland *et al*, on the basis of experimental work involving acetylene/oxygen flames and computational results, argued that only additions of vinylic radicals ($1\text{-}C_4H_5$ and $1\text{-}C_4H_3$) to C_2H_2 were fast enough to account for the observed rates of benzene formation (85). Regardless of the disagreement, Westmoreland has pointed out the significance of Frenklach's HACA model as a logical, comprehensive scheme. Even though certain aspects of the model are unconfirmed, Frenklach's work is interesting in that it is the first significant attempt to discover, in detail, the main chemical pathways to carbon formation.

Recently, Bohm and Jander have pointed out that the HACA route alone cannot produce large PAHs as fast as has been observed experimentally. They combined the work of others in an attempt to establish a reaction path for the fast growth of heavy PAHs before soot inception (58). The work of a number of researchers was combined to describe the C_1 to C_6 chemistry and the formation of larger PAHs was described by combining a number of molecular growth models. The successive-growth pathway described by the HACA model of Frenklach was combined with alternative, successive- and combinative-growth pathways. In this case the term *successive* is used to describe reaction sequences which involve small species adding to larger molecules to form benzenoid ring structures and the term *combinative* is used to describe reaction sequences in which the phenyl radical or some larger PAH radical is added. A number of these alternatives are illustrated in Figure 1-4 for pyrene. In Figure 1-4a the HACA model is illustrated for comparison. The sequence was extended to circumcoronene ($C_{54}H_{18}$), but species containing more than twenty-four carbon atoms were lumped. Figure 1-4b shows an alternate route involving C3 addition, reactivation and cyclopentadienyl recombination to form a PAH of higher molecular weight. Figure 1-4c illustrates another route involving the addition of a methyl radical followed by C_3 addition and C_4 addition. In Figure 1-4d it is shown schematically that a similar result can be obtained by the addition of C_4H_2, C_4H_3 or C_4H_4 and that CH_3 addition results in the formation of a C_5 ring.

A few of the combinative growth routes are illustrated in Figure 1-5. The reaction of phenyl with a PAH (pyrene) is used to illustrate the pathway. Figure 1-5a illustrates addition of the phenyl radical followed by acetylene addition and Figure 1-5c and d illustrate alternate combinative routes leading to the same species. Figure 1-5b shows a combinative pathway which does not require the addition of small radicals for molecular growth.

Results of the model were compared to the induction period for soot formation. A comparison of the successive- and combinative-growth sequence indicated successive growth alone could not produce large PAHs within the induction time for soot formation. This showed the limiting step in the successive reaction sequence was the formation of PAHs with four-carbon bays. Addition of combinative-growth routes which involved ring-ring condensation steps of aromatics allowed the model to produce large PAHs within

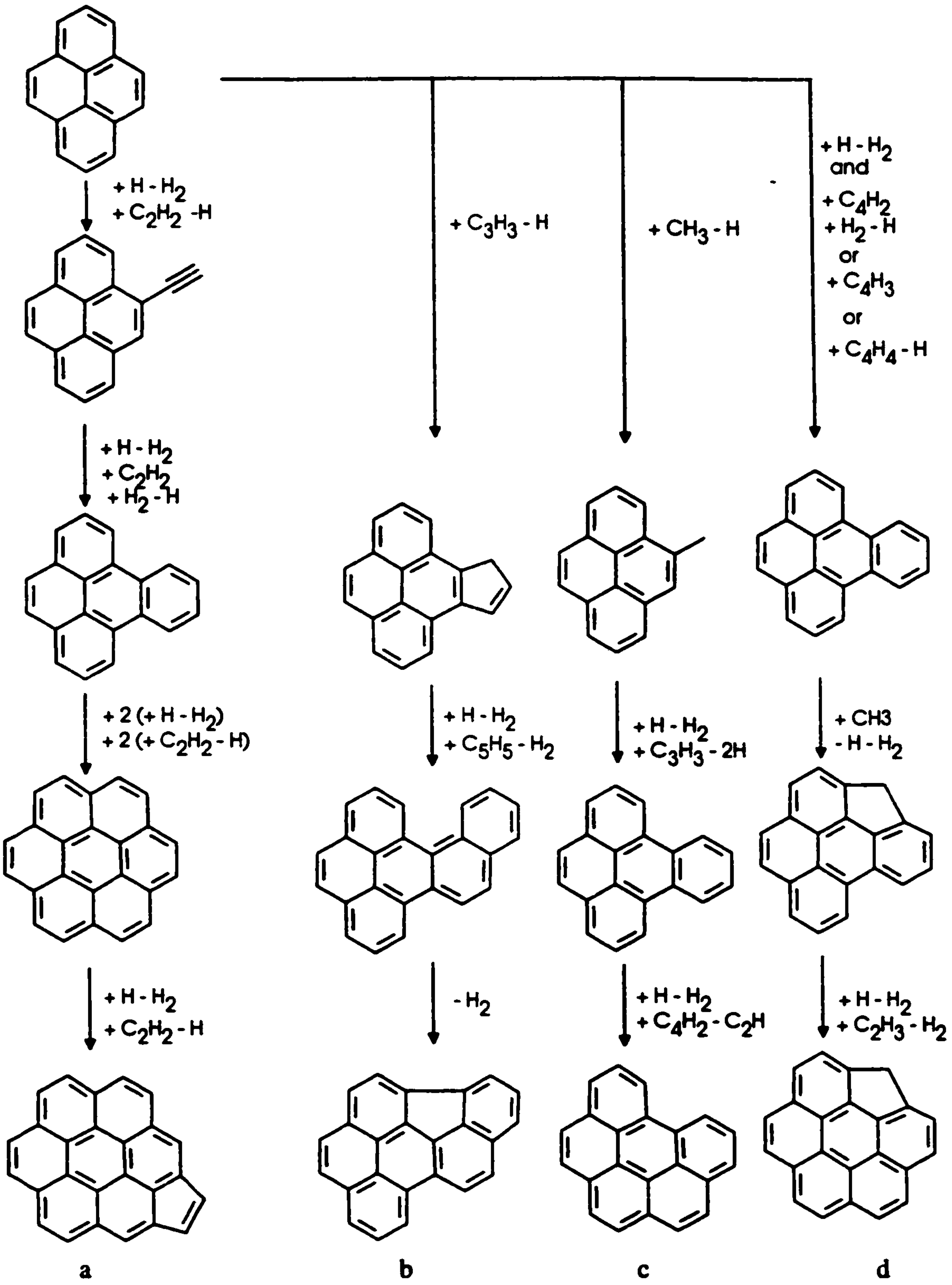

Figure 1-4: Several successive pathways for PAH growth from Reference 58.

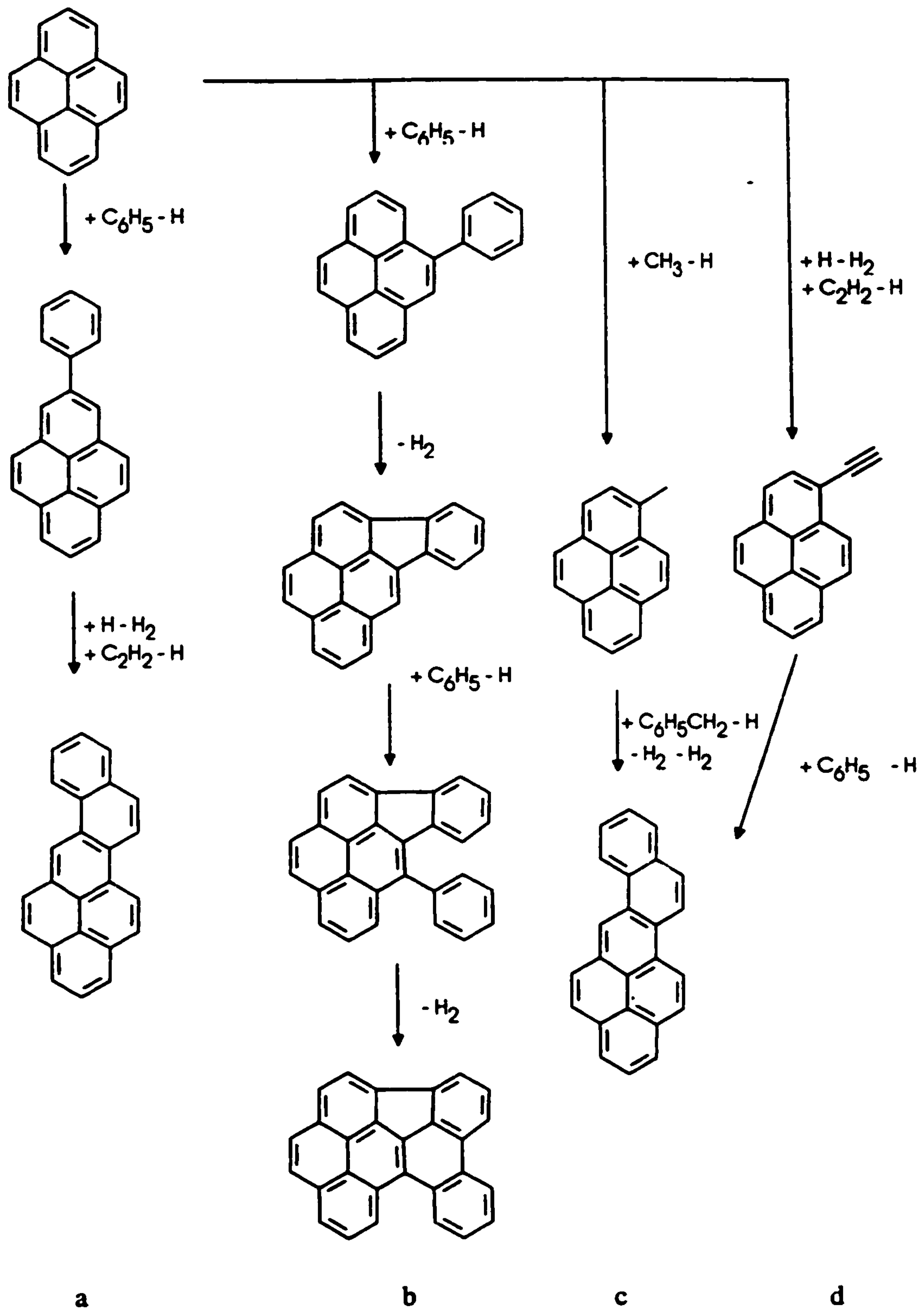

Figure 1-5: Several combinative growth pathways involving aromatic hydrocarbons from Reference 58.

the induction time for soot formation. These results indicated that the HACA pathway, which is favoured in the literature, cannot account for all of the molecular growth.

A large number of researchers have characterized the effluent from combustion processes (43, 73-75, 86-88). The literature on this subject is extensive, reaching into a number of fields, and only a few examples will be presented here. Lafleur *et al.* characterized complex mixtures of PAHs generated from the combustion of ethylene-naphthalene mixtures using chromatography and mass spectrometry (73). Homann *et al*, on the other hand, observed large molecules, ions, radicals and small hydrocarbons in hydrocarbon flames linked directly to a mass spectrometer (75,86).

Lafleur *et al.* adopted techniques previously developed for the identification of fullerenes (89,90) to search for large PAHs in a combustion system at 1630 K. Samples were quantitatively trapped at the reactor exit for analysis by gas chromatography-mass spectrometry, (GC-MS); high pressure liquid chromatography - atmospheric pressure chemical ionization - mass spectrometry, (HPLC-APCI-MS); and direct liquid injection into the APCI source, (DLI-APCI-MS). The GC-MS analysis provided separation and identification of known species from 128 to 324 amu, indicating the presence of species ranging in size from naphthalene to cyclopenta[bc]coronene. The analysis was extended by interfacing the HPLC to the MS using the APCI interface. This method revealed species in the 152- to 448-amu range. Direct liquid injection of the hydrocarbon mixture into the APCI source showed that molecules comparable in size (1792 amu) to "nanoparticles" of soot were present in the reactor effluent. The mass spectrum revealed clusters of peaks occurring from 400 to 2000 amu. Peaks corresponding to species with an even number of carbons dominated the structures below 1000 amu. Species in the

128- to 398-amu range made up the majority of the sample. However, in the 400- to 1000-amu range the maximum peak intensity was at 598 amu and the ion intensity for larger mass species generally decreased with increasing mass. Based on analysis of these results the authors suggested that a mechanism involving C_2 addition, producing even-numbered species, dominated the growth process and less important secondary processes resulted in species with odd numbers of carbon atoms.

Homann and coworkers performed a detailed analysis of the species formed during combustion (75). Sampling directly from a flame was achieved by using a molecular beam, interfaced with a time-of-flight mass spectrometer. They were able to detect neutral and charged molecules and radicals ranging in size from 2 to 3000 amu. Molecular formulas for large PAHs were suggested for species observed up to approximately 2000 amu. A background composed of large, not necessarily planar, PAHs and fullerenes were observed well into the 3000-amu range. The PAH ions were dominated by species with odd numbers of carbon atoms, whereas neutral PAHs with even numbers of carbon atoms were prominent. A consideration of the mole fraction of PAH ions and neutral species indicated that the ions were orders of magnitude lower in concentration. The degree of ionization depended on the ionization potential of the particular species. For example, the degree of ionization increased from 2×10^{-5} for $C_{20}H_{12}$ to 5×10^{-4} for $C_{59}H_{19}$. It was also shown that the profiles of neutrals and ions paralleled one another. It had been suggested that ions would polymerize faster than neutral species. This suggestion was not supported by these results.

Stein and Fahr (80) calculated PAH concentrations in equilibrium with acetylene and hydrogen based on thermodynamic properties estimated using a variation of Benson's group-additivity methods. A consideration of the increasing carbon and hydrogen content of the species observed in Homann's work indicated that growth occurred through large, thermodynamically stable, aromatic, species. Based on the observed growth of large PAHs, both successive- and combinative-growth mechanisms were suggested.

A key intermediate, about which there is still much controversy, is a precursor to solid soot, formed by condensation of gaseous hydrocarbons, but which has not yet progressed to soot. A number of the pyrolysis studies discussed in section 1.2 introduced the subject with respect to particulate carbon formation. However, most such studies were performed in combustion (36, 92-102).

Material sampled from flames in or on cold probes has been characterised using transmission electron microscopy (36, 92-97) and mass spectrometry (95, 101, 102). Lahaye and Prado sampled a flame using a cold probe. A TEM examination of the sampled material revealed discrete spherical species, which they postulated to represent soot precursors (36). Dobbins *et al.* also sampled material *thermophoretically* or from a hot flame onto a cold probe (93-97). The probe consisted of a metal arm which held a carbon coated TEM grid and which was inserted in and out of the flame mechanically with exposure times of 30 ms. Here aggregates of primary particles were observed. Early in the flame the size of the primary particles and the number of primary particles was smaller and independent spherical species, which were more transparent than the agglomerates, were also observed. This agreed with the pyrolysis work of Lahaye and Prado (36) and was attributed to a precursor material that was less dense than mature soot (93-95).

Dobbins *et al.* also analyzed material sampled thermophoretically by laser-desorption mass spectrometry (95,96). The MS analysis indicated ions with m/z ratio in the 200- to 300-amu range dominated and a small amount of ions were present in the 418- to 444-range. However, these results have been criticised because the cold probe could have caused the condensation, instead of collecting droplets which had already condensed (103).

Attempts at observing and characterising this material *in-situ* have been reported using laser-induced incandescence (92), ultraviolet absorption, laser induced fluorescence and laser scattering (92, 99-102). Vander Wal *et al.* used laser-induced fluorescence and incandescence to study the early regions of a sooting flame (92). Early in the flame they observed laser-induced fluorescence, which they attributed to the presence of large PAHs. Later in the flame they observed laser-induced incandescence, which they attributed to the presence of soot. A "dark region", between the early and late emission, was associated with the presence of a soot precursor, which was postulated to be a collection of large molecules which could have lost their absorbed energy by rapid, intramolecular, nonradiative decay rather than by fluorescence. Also, material was sampled thermophoretically from this "dark" region. TEM analysis indicated that along with commonly observed soot, tiny spherical species 2 - 5 nm in diameter were also present. These species were assumed to be soot precursor material.

D'Alessio *etal.* used absorption, fluorescence and scattering measurements in both the UV and visible to study sooting and nonsooting flames. Samples were extracted from the flame onto a fiber-glass filter using a water-cooled probe. Dichloromethane-soluble-material was analyzed by GC-MS for identification and by GC-FID for the quantitative determination of the main PAHs (2 - 7 ring species). Early in the flame, where no soot was expected, the absence of absorption in the visible region and the prevalence of a fluorescence peak at 330 nm was ascribed to aromatic structures with no more than two rings. The absorption coefficient calculated from the estimated concentration and molar absorptivity of two ring species was about two orders of magnitude lower than that measured from the flame. Since no soot was expected in this region it was assumed the UV absorption was due to an unidentified species. It was also suggested that the observed elastic scattering in this region was higher than that calculated from gaseous species and was due to the same unidentified species. By assuming these species were spherical and in the Rayleigh region their average diameter was calculated to be 2 nm. These so called transparent species, which did not absorb in the visible but fluoresced in the UV, were postulated to be soot precursors.

Minutolo *et al.* (100) also employed UV-visible light absorption, laser-induced fluorescence, laser-induced incandescence and light scattering to study sooting and non-sooting flames. In this work it was assumed, based on D'Alessio's work, that absorption was due to three components: sp^2 carbon atoms, two-ring aromatics and soot like material. From this assumption then the absorption coefficient was suggested to be made up of 3 components. The first was assumed to involve absorption due to two ring PAHs and was estimated from the fluorescence emission. Another component was evaluated from the measurement of light absorption in the visible where it was assumed only soot would absorb. The final, nonemitting component was evaluated by difference from the total absorption. Each of these components was considered as a function of the height above the burner. It was argued that this nonemitting component represented a soot precursor which was neither a discrete aromatic nor mature soot.

A number of factors may have introduced errors in these results. Scattering calculations are very sensitive to the (usually unknown) high temperature spectral properties of all the gases, liquids and solids present. The estimation of concentrations in the flame was also sensitive to the sampling procedure. Therefore these results did not provide conclusive evidence for an intermediary species between hydrocarbons and mature soot.

1.4 Metal-Catalyzed Carbon Formation and Deposition

Industrial steam cracking of hydrocarbons has generally been performed in high temperature stainless steel reactors. The formation of metal-catalyzed carbon from the interaction of hydrocarbons with metal surfaces has been studied extensively (18-27, 104-115). The discovery of interesting carbon structures, including fullerenes and nanotubes, from arc discharges has renewed interest in the subject of filamentous carbon, resulting in a tremendous amount of work in this field (107). The following discussion serves to introduce the topic and indicate some of the work which is most relevant to that presented in this thesis, but does not attempt to examine all the work performed in this field.

It has been suggested that the first metal-catalyzed filaments were observed over a century ago (104, 107). However, the lack of analytical instrumentation would have made characterization difficult (107). Work presented over two decades ago indicated that, when hydrocarbons were passed over hot (> 873 K) metal surfaces, wires or filaments, composed primarily of carbon, were formed. These fibers may be hollow tubes consisting of hexagon-rich cylinders made up of sp^2 hybridized carbon (nanotubes), as in graphite (107), or may be formed from stacks of graphite platelets (nanofibers).

Baker and others have shown a wide variety of structures can be obtained by decomposing hydrocarbons over a variety of metal surfaces (Co, Ni, Fe, Pt, and Cu) (105, 107-114). It has been shown that filament formation does not poison catalyst surfaces and in some instances may enhance the catalytic effect. It has been shown that small catalyst particles (<25nm) will often result in nanotubes whereas larger particles will generally produce nanofibers. Further, the shape of the catalyst particle tends to have an effect on the direction of the stacks of graphite platelets making up the fiber. Depending on the orientation of the metal crystallite, the platelets may be stacked in a direction perpendicular to the fiber axis, parallel to the fiber axis or in a herring-bone arrangement. Growth may occur on one end of the catalyst surface, resulting in a fiber with a catalyst cap, or on two ends of the catalyst surface, resulting in a fiber with the catalyst particle located in the center. Under certain conditions, graphite platelets may form in which growth results from all planes of the catalyst particle.

The most widely accepted model for filament growth involves direct decomposition of the hydrocarbon on the metal surface. Baker *et al.* (105) postulated that decomposition of hydrocarbons on exposed surfaces of the metal catalyst resulted in gaseous hydrogen and carbon. It was suggested that the carbon could diffuse through a metal particle and precipitate at the other end, lifting the catalyst particle away from the metal surface. It was suggested that the exothermic nature of the surface decomposition resulted in a temperature gradient across the particle and that the carbon precipitated at the cooler end allowing the particle to continue to grow.

A number of studies have examined metal-catalyzed carbon formation as a function of reaction time and temperature(18-24, 114, 115). These studies indicated that the structure of the carbon deposited onto metal surfaces changed with increased reaction temperature and time. McCarty *et al.* used SEM, TEM and temperature-programmed surface reaction to establish the presence of several forms of carbon on catalysts (21). These studies indicated metal-catalyzed filamentous carbon was overlaid with layers of *pyc*. It has been hypothesized that the *pyc* encapsulated the surface, resulting in deactivation of the catalyst, whereas filamentous carbon involved diffusion through the particle, leaving the catalyst exposed (21, 111). Recent studies involving the surface morphology of coke deposited on metal surfaces, have confirmed this earlier hypothesis. Wu *et al.* have shown that, during the pyrolysis of propane, filamentous carbon is present at 1023 K but, when the temperature is raised to 1173 K, the filaments are covered by spherules of coke (115). It was also demonstrated that prolonging the coking time at 1073 K resulted in a similar morphology to that observed at 1173 K (115).

A number of researchers have shown that the deposition rate onto metal surfaces is initially high and eventually levels off (19-22). Figueiredo has correlated the surface morphologies with initial and final rates of deposition (22). For a metal which does not catalyze the formation of filamentous carbon, the rate of deposition was shown to remain constant. For metals that acted as catalysts for the formation of filamentous carbon, the rate was initially high and then relaxed to a steady value. It was found that the rate on all metals eventually relaxed to the same value, regardless of the substrate material. SEM analysis and temperature controlled oxidation studies were used to characterize and determine the relative amounts of catalytic coke and *pyc*. These results indicated that a constant rate was established once the catalytic coke was covered with *pyc* (22). The results of these studies lead one to believe that, in cracking reactors, initially catalytic coke may be important but, over time, pyc will dominate the deposition process.

1.5 Objectives

Many researchers have considered deposition of carbon from the pyrolysis of a wide variety of compounds. In many studies, particular aspects of a reaction system were examined and investigators proposed mechanisms to describe their individual results. The mechanisms for deposition near industrial steam cracking conditions fall into two categories: hydrocarbon adsorption or formation of an aerosol. The detailed gas composition in higher temperature combustion has been established. However, the extent of molecular growth corresponding to the pyrolysis of ethane under industrial cracking conditions has not been published. The purposes of this study are two fold: first to measure the deposition rate as a function of residence time and initial ethane concentration and secondly to identify and estimate the concentration of the species present in the flowing gas at the same residence time and extent of conversion. A consideration of the rate of *pyc* deposition, with respect to the gas composition, would serve to extend the conclusions of research on other hydrocarbons to the pyrolysis of ethane and to provide new insight into the problem.

Characterization and estimation of the relative proportions of each class of species in the system should allow one to demonstrate the possible importance of each class. For ethane pyrolysis, the light gas composition had not previously been correlated to the deposition rate; this was the starting point for this study. Numerous studies point out the significance of molecular growth but few provide experimental evidence for molecular growth in low temperature pyrolysis. In this study a detailed chromatographic and mass spectrometric analysis of the large molecular products was undertaken. A key intermediate, about which there is still much controversy, is a precursor to solid carbon, formed by condensation of gaseous hydrocarbons, but which has not yet progressed to soot or coke. Because of the possible, important role of this carbon precursor, we decided to seek evidence for it in the absence of oxygen and at lower temperatures. A pyrolysis system is expected to provide a less severe environment in which to attempt to observe soot precursors. In the present work we used novel techniques in an attempt to detect and quantify a fog directly in the hot zone.

2 Experimental

2.1 Linear Flow Technique

The linear flow technique has been used by various workers for investigating pyrolysis reactions (3, 13, 14, 19, 29, 38, 56, 50-53) and was the central experimental technique used in this investigation. In this technique the reagent is passed at a constant flow rate through a heated cylindrical reactor and the products coming out of the reactor are analyzed. The reactor residence time can be calculated by dividing the amount of gas in the reactor by the amount of gas entering per unit time. The following sections provide a description of the apparatus and the analytical methods used in this study and deal with some of the potential errors in the flow method at high conversion.

2.2 The Flow System

The experimental apparatus used in this investigation was a flow system. The overall flow system can be divided into three parts: the supply system which contains reagent flow measurement and control units, the reactor section which can be modified for several different experiments and the pressure controlling, pumping, sampling and analysis section.

2.2.1 The Supply System

An existing flow system (29) was modified for the purposes of this work. The system shown in Figure 2-1 consisted of a series of gas inlets, pressure regulators (Matheson, model 4473) , Teflon valves, mass flow controllers (MKS, model 1159B, 0-500 sccm), a common pumping system, and a common pressure transducer (Bell and

Howell model CEC 1000, 0-50 psi). Reagents were taken directly from cylinders, through pressure regulators (approximately 2 atm), and into the flow controllers. Reagent (ethane) and other gases (argon, hydrogen, hydrogen sulfide, carbon dioxide, acetylene, benzene and propylene) were tested for purity as described in section 2.4.1. Two lines connected the supply system to the reactor. One was connected to the micro-balance casing. The other connected directly to the reactor entrance or alternatively to the liquid injection system and then to the reactor entrance. The liquid injection system consisted of a heated chamber, in which water could be placed, and a temperature controlled condenser. For steam dilution experiments gases were diverted through the condenser to the reactor entrance.

Reagent pressure in any section of the supply system could be measured, to within 0.2 kPa, using the common pressure transducer, which was calibrated against atmospheric pressure and against a vacuum before each experiment. A Pirani gauge was also used to ensure a vacuum (less than 10^{-2} kPa) was achieved before performing experiments. Reagent flow rates were measured and controlled, to within 0.1 standard cubic centimeters per minute (sccm), with the mass flow controller and a mass flow controller power supply readout (MKS, model 247C, 4 channel read-out). Temperature control in the condenser was achieved by connecting the insulating jacket to an external circulating bath (Lauda, RCS-6, -20°C to 150 °C). Condenser temperature was measured internally through a thermocouple well positioned in the top of the condenser. A vacuum system with a Pyrex oil diffusion pump and a rotary pump (Welch, model 1405) was connected to the main supply system for evacuation purposes.

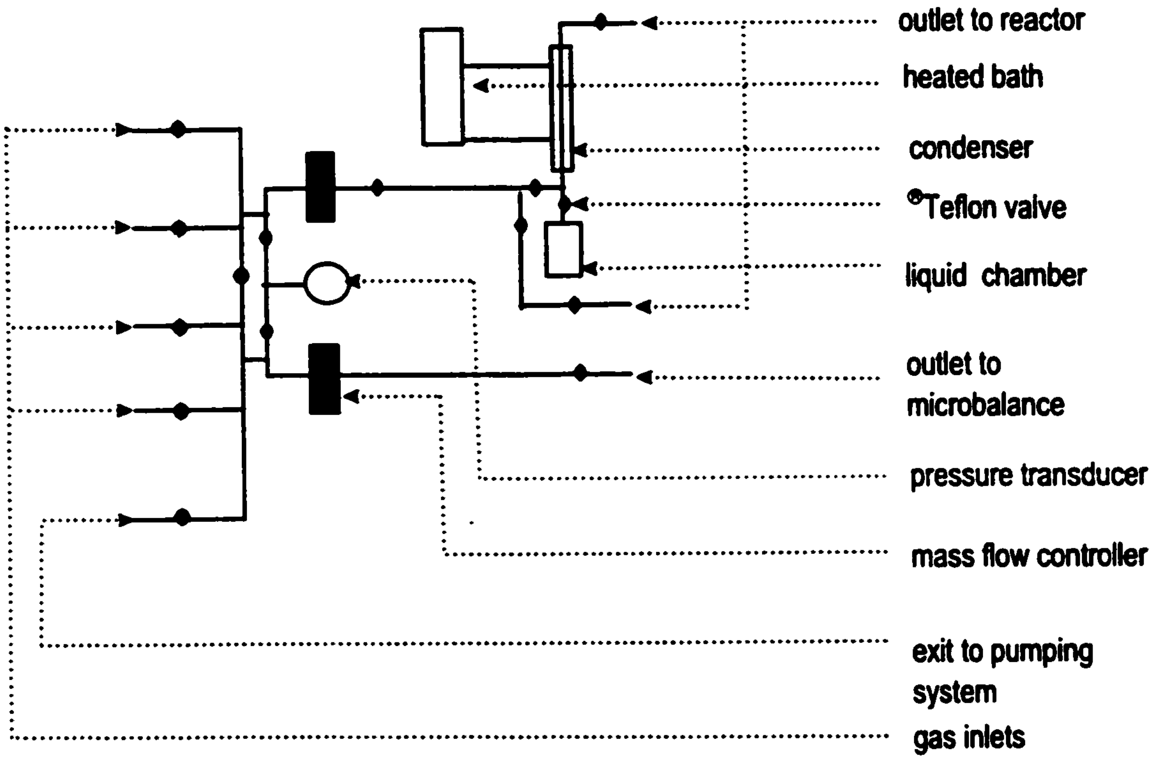

Figure 2-1: Schematic of the supply system (not to scale).

2.2.2 The Reactor

2.2.2.1 Reactor 1, Conventional Flow

The reactor, shown in Figure 2-2 for conventional flow, was constructed to allow for *in-situ* measurement of materials deposited on the reactor surface. The reactor section consisted of three inlets, a vertical tubular furnace, a cylindrical reactor (1.01 cm inside diameter) constructed of quartz, a micro-balance (Cahn, model RG2000, 0.1-1000 μg) encased in a vacuum tight casing (Cahn, model 2580), and a quartz substrate (5.0 cm length and .31 mm diameter) suspended, by a quartz thread, from the micro-balance into the hot zone of the reactor.

Initially, a commercial furnace (Marshall, model 1522)(furnace 1) was utilized. However, due to failure of the commercial furnace, a Nichrome wire resistive furnace (furnace 2) was designed and built to provide a similar temperature profile. Heating of the reactor was achieved by connecting the furnace to a temperature controller and a power supply (Omega, model CN7000). The temperature controller utilized a thermocouple (platinum-13% rhodium) which was placed in a quartz tube of 4mm outside diameter attached to the outside of the reactor, in the hot zone. A second thermocouple (platinum-13% rhodium), used for temperature measurement, was placed in another quartz tube attached to the outside of the reactor. Temperature profiles, as shown in Figures 2-3, were obtained by measuring the temperature at constant intervals down the length of the reactor.

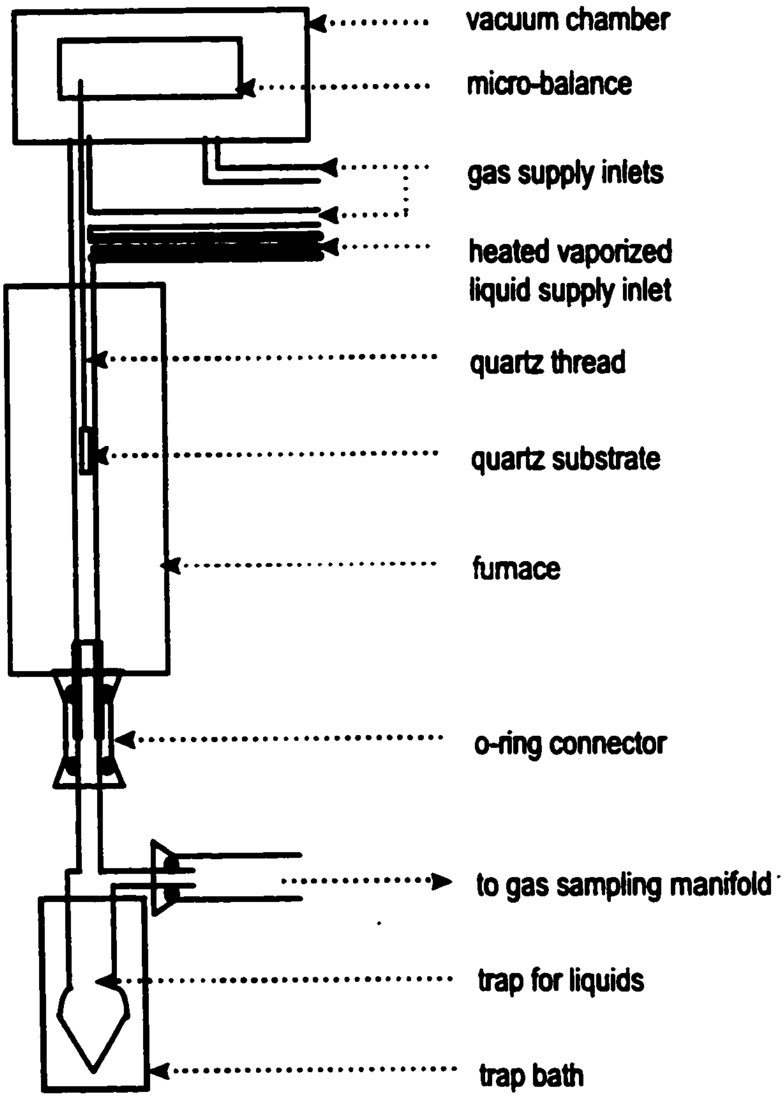

Figure 2-2: The conventional flow reactor and associated apparatus (not to scale).

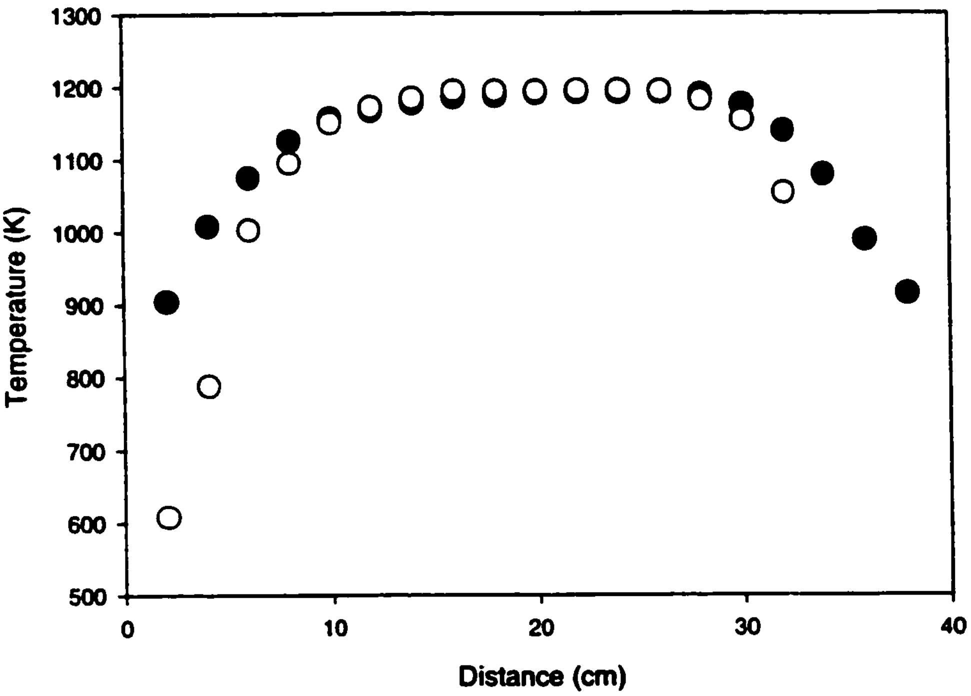

Figure 2-3: The temperature profiles from furnaces 1 (open circles) and 2 (closed circles).

2.2.2.2 Reactor 2, Counter Flow

The reactor used for counter flow experiments was also constructed of quartz and is shown in Figure 2-4. Flow of ethane entered the reactor at the top and exited at a T-joint halfway down the heated section. A similar flow of argon entered the reactor at the opposite end and also exited at the T-joint in the middle. Light from a diode laser (Alpec, 670 nm) was directed through a quartz window, down the axis of the reactor, out a quartz window, through an aperture and onto a photodiode (Texas Instruments, TSL 220) which produced a frequency. Data acquisition was done under control of a personal computer (80-386). The detector output was converted into digital form and a data acquisition program, developed in the departmental electronics shop, was used for data analysis.

For experiments in which substrates were placed in the reactor, the top section of the reactor was replaced with a removable substrate holder shown in Figure 2-5. The flow of ethane entered the reactor at the bottom and exited at a T-joint halfway up the heated section. A similar flow of argon entered the reactor at the top end and also exited at the T-joint in the middle. The substrate was suspended in the argon-filled region of the hot zone.

2.2.3 Pressure Controlling, Pumping and Sampling Section

Gases from the conventional reactor exited into a trap, connected through an o-ring seal, which was used for collecting liquid products (Figure 2-2). Flow exited from the trap, through another o-ring seal, into a manifold (Figure 2-6) containing a valve for sampling of product gases and a pressure transducer (MKS, model 122A, 0-133 kPa) which was connected to a pressure controller (Omega, model CN-2000). Gases exited

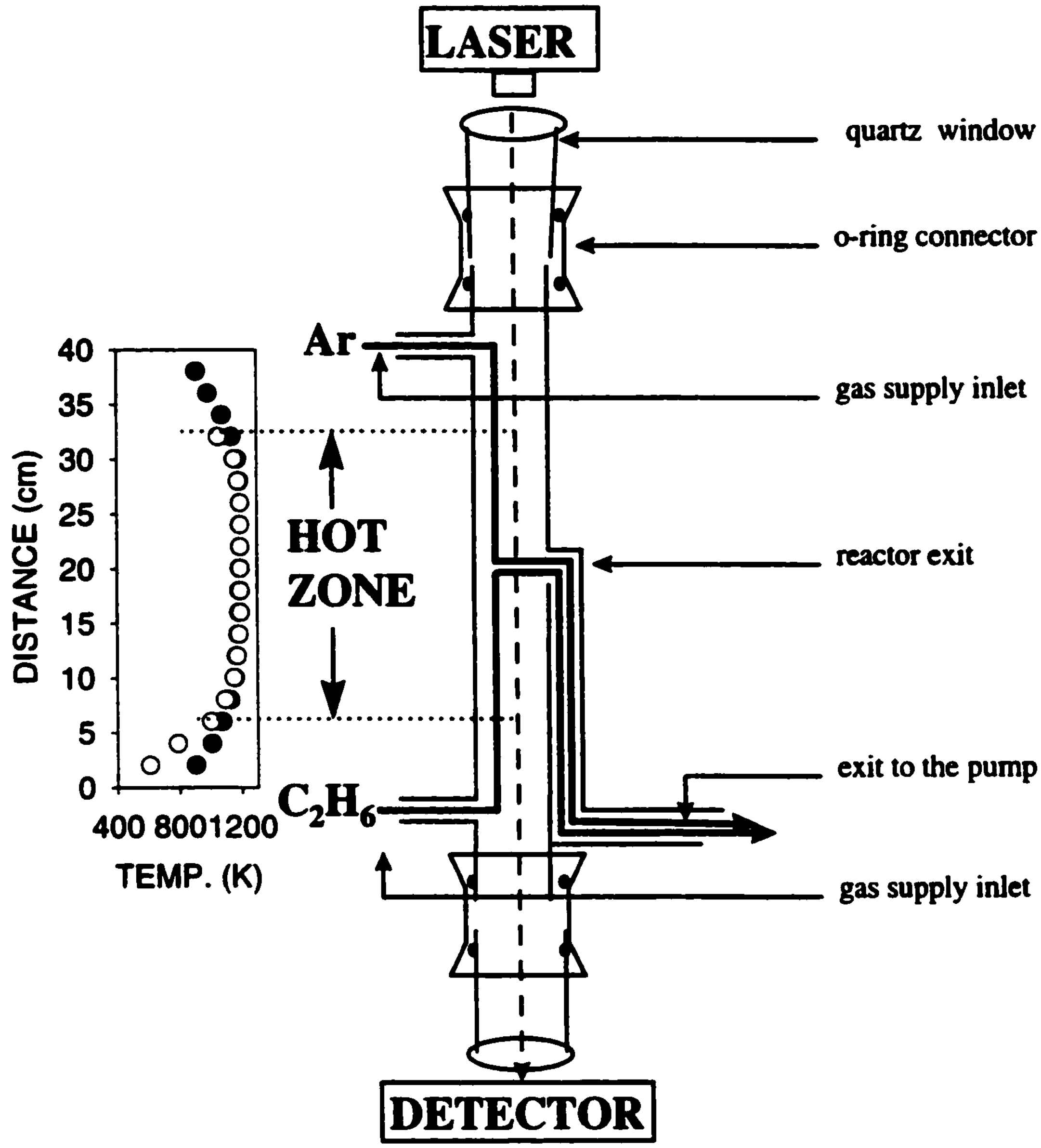

Figure 2-4: The counter-flow reactor and associated apparatus (not to scale) and the temperature profiles indicating that the gases exited in the centre of the hot zone.

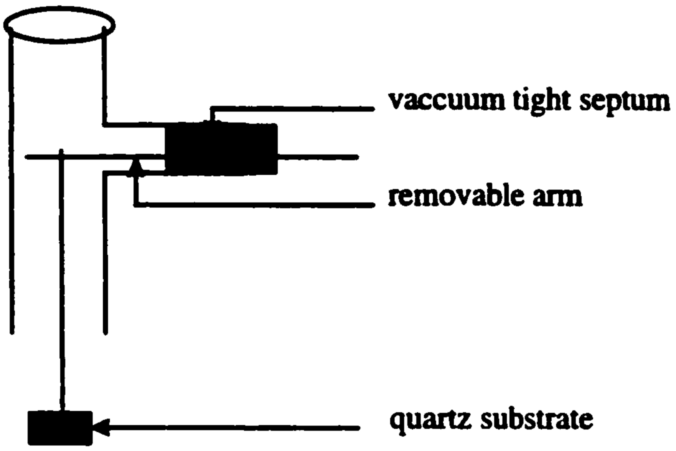

Figure 2-5: The removable apparatus for dropping a substrate in the counter-flow reactor (not to scale).

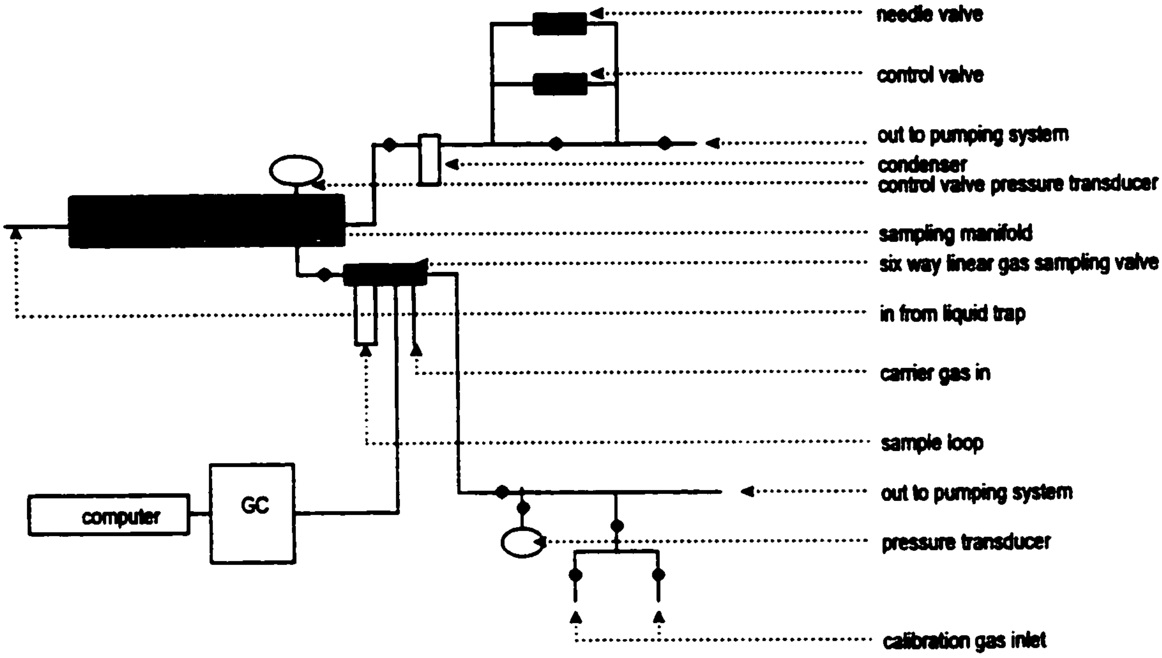

Figure 2-6: The sampling, analysis and pressure control section.

the system through a solenoid valve (MKS, 248A/B) which was adjusted by the controller. The required pressure was set on the pressure controller and calibrated against another pressure transducer (Bell and Howell, model CEC1000, 0-50 psi). The controller read the system pressure and automatically controlled the pressure by opening and closing the controlling valve, which was connected to a rotary pump (Welch, model 1397). The needle valve (Whitey, model SS22RS4) connected in parallel to the control valve was used as an additional gas exit for fast flow rates. This bypass valve could be manually set to achieve flows with minimal variation, which was necessary for reduction of noise during micro-balance runs.

Gaseous products were sampled at the reactor exit manifold shown in Figure 2-6. During gas analysis either 2 or 10-ml samples of gaseous products were extracted from the system by means of a six-way linear gas sampling valve (Varian, 57-000034-00) and injected onto the gas chromatograph (Tracor, model 550).

2.3 Experimental Procedures

2.3.1 Procedure 1, Conventional Flow

Before starting any experiment, the system was evacuated and the pressure transducers were calibrated against atmospheric pressure. After a vacuum was established ($<10^{-2}$ kPa) the system was leak tested. The maximum allowable leak into the supply side of the apparatus was 1 x 10^{-4} kPa/minute and that into the sampling side was 1 x 10^{-4} kPa/minute. For experiments involving the trapping of liquid products, leak rates on the sampling side were approximately a factor of ten higher. Once leak tested the system was filled to the desired pressure with an inert gas (argon, Matheson, prepurified), flow rates for reagent and dilution gases were set to the desired values and the pressure controller was appropriately tuned for the flow rate of interest. For direct comparison of deposition rates, measured half-way down the reactor, and gaseous products, measured at the reactor exit, two analyses were performed. Flow rates for deposition experiments were half of those for analysis of gas phase products. Once flow rates were set, all necessary analyses were performed. During experiments, the pressures at the inlet and exit of the reactor were monitored. In all experiments performed, pressures at the inlet and exit of the reactor were equivalent. In experiments where the parameters of the controller were insufficient, variability in the reactor pressure resulted in unacceptable levels of noise on micro-balance traces and pressures were set manually.

For the mixtures of ethane with argon, hydrogen sulfide, hydrogen, carbon dioxide, acetylene and propylene; the ethane and the additive were passed through separate flow controllers into a common line leading to the reactor. Ethane was passed into the common line at a constant flow rate of 41.8 sccm (standard cm^3 min^{-1}) and the additive was passed into the same line with a flow rate of 10.4 sccm. For benzene addition a 20 % mixture of benzene and ethane was prepared in a 12-L bulb and the mixture was passed through the same flow controller. For these experiments all areas before the mass flow controller were heated to greater than 70 °C to insure all benzene remained in the gas phase.

2.3.1 Procedure 2, Counter Flow

Flow of ethane at a rate of 6-sccm entered the reactor from the top or bottom and exited at a T-joint at the mid-point of the heated section. A counter flow of argon entered the reactor at the opposite end and also exited at the T-joint in the middle. The total pressure of gases in the reactor was controlled at 40 kPa.

2.4 Sampling and Analysis

2.4.1 Gas Phase Analysis

Products were separated on two different columns. Butane, butene, butadiene, propane and propylene, were separated on a 1.2-m (Poropac, type Q) packed column (column 1) at 150°C and benzene, toluene and styrene, on the same column at 225°C. Hydrogen, methane, ethane, ethylene and acetylene were separated on a 1 m (10% NaOH on alumina) packed column (column 2) at a temperature of 0°C. A flame ionization detector was utilized for analysis of all compounds except hydrogen, for which a thermal conductivity detector (Gow-Mac, 10952-6) was utilized. Data acquisition was done under control of a personal computer (80-386). Analogue signals were converted to digital form by a voltage to frequency converter. A GC data acquisition program developed in the department electronics shop was used for analysis of data.

Product identification was achieved by comparison of sample retention times to those of known standards and was confirmed by mass spectrometry. Pertinent data and discussion of the analysis is provided in Chapter 3. In order to establish retention times and purity of reagents, standard gases (Matheson, research grade) were run separately, at the temperatures discussed above. Once the composition of the gaseous mixture was established, routine analysis for the hydrocarbons of interest could be achieved using a temperature ramp (0-200°C in 10 minutes and held for the duration of the run, 30 minutes, column 1). Standard mixtures were made and the concentration of products was determined by comparison with calibration curves of at least four points. In all cases the calibrations were linear and extrapolation was not necessary. In this manner analysis of all gas phase products, excluding acetylene where column 2 was used and hydrogen where a TCD detector was used, could be achieved in one run. Samples for mass spectrometric analysis were collected in a 100-mL bulb at the exit manifold. The sample and standard mixtures were analyzed by mass spectrometry (VG Quattro) using an electron impact source at an ionizing potential of 15 eV.

2.4.2 Carbon Deposition

Carbon deposition rates were measured by following the increase in the mass of a quartz substrate suspended in the middle of the hot zone of the reactor. Calibration of the micro-balance was achieved by removing all weight on both arms and zeroing the output. A weight equivalent to the substrate was placed on one arm and an equal counterweight was added to the other until the balance returned to zero. Then full scale (10000 units) was set to represent 5mg to 50mg using calibration weights. Initially, the microbalance was calibrated prior to each experiment; however, this was found to be unnecessary. Typical rates measured were on the order of 5 to 100 μg/min. Due to background noise, results were found to vary by approximately 1 μg/minute under ideal flow conditions.

For deposition onto a metal substrate cuttings from a stainless steal pipe (Incoloy 800 HT) were used in place of the quartz substrate. The substrates were heated to the desired temperature under vacuum and pumped down for one hour. After deposition the metal substrate was cooled to room temperature under vacuum, removed from the vacuum system and cut into 2 mm sections. Each Section was coated with gold at 27 Pa with an automatic sputter-coating apparatus (Sam-Sputter-2A) and examined by scanning electron microscopy (SEM, Bausch and Lomb, Nanolab 2000). A 2-mm section of the carbon coating was removed from the metal substrate. SEM images of the top and underside of the coating were obtained.

2.4.3 Liquid Analysis

Liquid samples were collected in the trap at the reactor exit. The neck (9 mm o.d.) of the trap extended to the hot zone of the reactor and allowed for the capture of most tars exiting the reactor. The main body of the trap was filled with glass rings and had a plug of glass wool at the exit. To ensure all liquid products were collected, the trap was kept at approximately 213 K using a "dry ice" and chloroform bath. The temperature of the bath was monitored throughout the experiment using a type K thermocouple (Omega, model 199). Samples were collected under steady state conditions for 60 minutes. Initially the trap was filled with argon and weighed on an analytical balance (Mettler, AJ100) it was then attached to the reactor exit and pumping system. The system was pumped to a vacuum (1×10^{-4} kPa) and filled with argon. Ethane was passed through the reactor for 60 minutes and then the flow was switched to argon for 5 minutes. The system was pumped down to less than 0.01 kPa and then filled to atmospheric pressure with argon. The trap was then removed from the system and weighed. The trap was then rinsed with hexane(Anachemia, AC-4858) into a 100-mL volumetric flask and brought to volume for HPLC-UV analysis. For APCI-MS analysis, samples were obtained in the manner which is described above, but using dichloromethane (Fisher Scientific, HPLC grade) as a solvent.

Three sets of HPLC experiments were performed. Samples were analyzed by HPLC (Hewlett Packard, series 1100) on a 25 cm column (Vydac, 201TP54) with the water/acetonitrile(acn)/dichloromethane(dcm) solvent gradient shown in Table 2-1. The injection volume was 20 μL and the flow rate was 0.5 mL/min. A UV detector (Bio RAD Laboratories, model 1305) set to 260 nm was used for detection. Product identification was achieved by comparing sample retention times to those of known standards. Pertinent data from this method are denoted LC-UV in Chapter 3. Standard samples were run separately in order to establish the retention times and the purity of the standards. Concentrations of samples were determined by the method of standard additions, in some cases, or by the preparation of calibration curves.

In the second set, MS detection was used to confirm the identity of these species. For the HPLC-APCI-MS analysis, two LC pumps (Shimadzu) were used to provide binary solvent gradients to the LC column (Whatman, PAH). The eluent passed through a UV detector into the APCI interface of the mass spectrometer described above. The operating conditions were as follows: nebuliser gas, 30 standard liters per hour (sLph) of N_2; source temp., 350°C; nitrogen bath and sheath gases, 300 sLph; orifice potential, 60 V; corona discharge, 3.5 kV. Due to background problems in the low mass range (m/z < 202), selected ion monitoring (SIM) was used to establish the masses of the species quantified by LC-UV.

In the third set an acn/dcm gradient (100% acn linearly programmed to 100% dcm over 30 minutes, holding for 25 min and linearly programmed to 50% acn/dcm over 2 min) was used to separate higher mass species. For the third set, m/z ranges 50 units wide were scanned at the appropriate retention times.

Table 2-1: Solvent gradient for the LC-UV analysis.

TIME (MINUTES)	ACETONITRILE/ WATER (%)	DICHLOROMETHANE/ ACETONITRILE (%)
0	50	0
15.0	80	0
16.0	100	0
18.0	100	0
20.0	0	100
24.0	0	100
25.0	100	0
28.0	50	0
30.0	50	0

For the highest mass species liquid pyrolysis products were collected for 180 minutes and diluted to 25 mL with dcm; 20 µL samples were injected directly into the heated nebulizer interface of the MS. Dichloromethane (0.5 mL/min) was the mobile phase and mass spectra were obtained by scanning the 300-1000 *m/z* range. The molar sensitivity of the instrument was established by examining 20 µL samples of 0.0014 M naphthalene, phenanthrene and pyrene standards.

The liquid samples were also analysed by GC-MS. Samples of liquid products (1 mL) diluted in dcm were washed through a 5 cm x 0.5 cm silica gel column (Aldrich, cat. # 28-852-7) with 5 mL of dcm. Washing was necessary in order to remove particulate matter and very large species, which could damage the GC column. The instrument used for GC-MS consisted of a gas chromatograph (Hewlett Packard 6890) coupled to the electron impact (EI) source (70 eV) of a triple quadrupole mass spectrometer (VG Quattro). The first 1 mL fraction was analyzed by injecting 1 µL of it onto the GC column (HP-5 CrossLinked 5% Phenyl Methyl Siloxane, HP 190913-433) with a temperature profile (inlet 330°C, starting column temperature 50°C, rate 10°C/min., final temperature 300°C, holding for 20 min.). The MS conditions were as follows: inlet 300°C, ionizing voltage 70 eV, *m/z* scanned 50 - 350 amu, scan duration 0.5s.

2.4.4 Aerosol Analysis

Direct observation of the hot zone was performed by two methods. Light from a diode laser (Alpec, 670 nm) was directed through a quartz window, down the axis of the reactor, out a second quartz window, through an aperture (2 mm diameter) and onto a photodiode (Texas Instruments, TSL 220). The reactor was also examined visually.

Pictures of the hot zone of the reactor were obtained with a digital video camera (Sony, PC10) directed along the axis of the reactor. The camera was focused on the centre of the region in which ethane was flowing through the hot zone.

Quartz discs (7 mm diameter and 3 mm thick) were suspended in the upper (argon blanketed) region of the hot zone. Using a wire arm operated through a septum, the disks were suspended from the arm with quartz thread and then allowed to fall through the flowing gases to the lower window. The disks were removed from the vacuum system, coated with gold at 27 Pa with an automatic sputter-coating apparatus (Sam-Sputter-2A) and examined by scanning electron microscopy (SEM, Bausch and Lomb, Nanolab 2000).

Circular gold wire grids (Electron Microscopy Sciences, 200-Au50), with a 3-mm diameter (200 mesh), were placed in a quartz sample holder. The quartz sample holder and grid were then suspended from the arm and dropped through the system in a manner similar to the quartz disks. Disks were removed from the system and holder without contacting the front surface of the grid and were analysed by transmission electron microscopy (Philips, EM201).

Higher surface area substrates were made by coiling 3 meters of quartz thread into a cylindrical form (5 cm in height with a diameter of 7 mm). These substrates were also suspended in the argon-blanketed region of the hot zone of the reactor and dropped through the hot gases. The substrates were washed with 3 ml of dcm (Fisher Scientific, HPLC grade). The fluorescence spectrum of this liquid was recorded using a spectrofluorophotometer (Shimadzu, RF-5301 PC) with an excitation wavelength of 270 nm. The liquid sample was then placed in an oven at 60 ?C and evaporated to about 0.2 mL. The remaining material was placed onto the platinum filament of a thermal desorption probe (VG, Quattro) and the remaining solvent was allowed to evaporate. The probe was then placed into the electron impact (EI, 70 eV) source of a quadrupole mass spectrometer (VG Quattro) and a current of 1500 mA was used to heat the filament.

2.5 Reaction, Transport and Flow

The goal of this work was to consider the pyrolysis of ethane under industrially relevant conditions. These conditions are rather extreme and, as a consequence, some of the usual assumptions are not valid. The following discussion deals with some of the potential errors in the flow method.

2.5.1 Incomplete Radial Heat Transfer

In the use of a flow reactor, it is assumed that the entering gas molecules warm to reaction temperature instantaneously at the inlet of the reactor. However, when a gas is passed through the reactor at a fast flow rate, the gas molecules will travel a certain distance down the reactor before attaining the reactor temperature. This delay in warming the reagent results from incomplete radial heat transfer. Furue and Pacey (96) found that the fractional experimental error is approximately equal to $r^2/\kappa t$, where r is the radius of the reactor, κ is the coefficient of thermal diffusivity and t is the time. Under the conditions of these experiments, the errors in calculated rate constants, for the shortest residence times considered, have been calculated to be less than 10 % at reactor pressures below 40kPa and for residence times greater than 1.5s. The error was no greater than 20% at all pressures. The error due to incomplete radial heat transfer is plotted as a function of

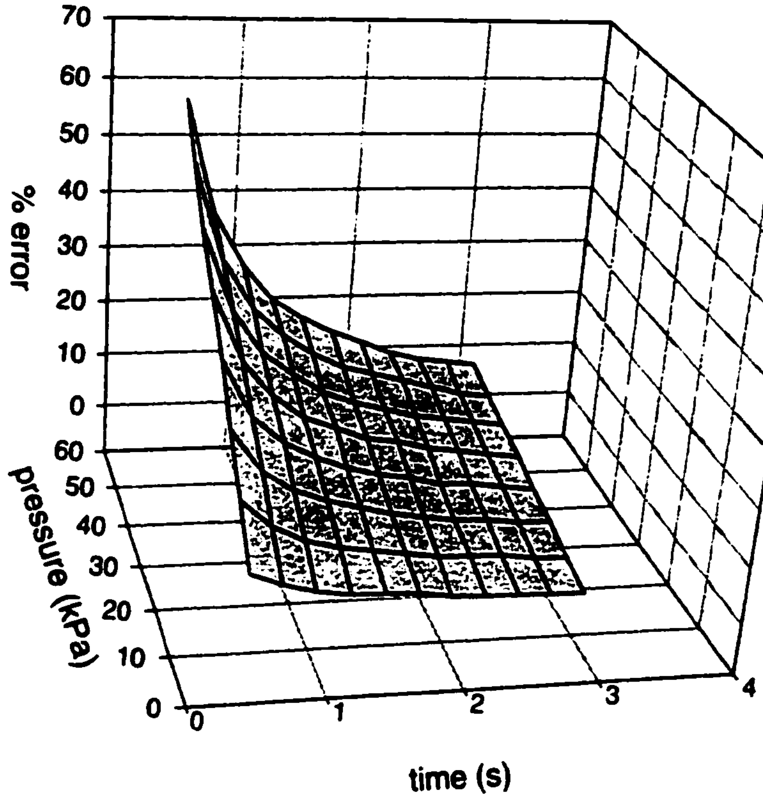

Figure 2-7: The error due to incomplete radial heat transfer plotted as a function of time and pressure for a temperature of 1185K.

time and pressure in Figure 2-7. An error of 55 % is reached at a time of 0.5s and a pressure of 50 kPa.

2.5.2 Mass Transfer

High conversion results in concentration gradients down the axis of the reactor. Reactant molecules move faster toward the exit of the reactor due to diffusion. Product molecules diffuse in the opposite direction. Furue and Pacey (116) reported that an upper limit to the fractional error in residence time caused by mass transfer is equal to $(r^2/48D)+Dt_r^2/l^2$, where D is the diffusion coefficient. The error due to mass transfer was calculated to be less than 10 % at residence times less than 10 seconds and no greater than 40% at longer residence times.

2.5.3 Pressure Drop

When a gas is passed through a reactor a pressure drop arises along the reactor as a result of the friction between the moving gas and the stationary tube. Any error arising from the pressure drop can be minimized by measuring the pressure, both at the inlet and exit ends of the reactor, and using the average for calculations. The effect of pressure drop was insignificant under the conditions of this study.

2.5.4 Volume Expansion and the Calculation of Residence Time

During all experiments the total pressure and temperature were maintained constant. Therefore, according to the ideal gas law the volume remains constant unless the reaction increases or decreases the number of moles in the system. For example a reaction 2-1 of the form,

$$A \rightarrow B + C \qquad 2\text{-}1$$

results in an increase in the number of moles. This leads to an expansion of volume, and in a flow system the molecules move out of the reactor faster, resulting in shorter residence times. At early stages of the reaction, any increase in volume is insignificant. Hence, at low conversion the error caused by volume expansion is negligible and the nominal residence time of a gas in the reactor is given by Equation 2-1,

$$t_r = n/(\Delta n/\Delta t) \qquad 2\text{-}1$$

where n is the number of moles in the reactor and $\Delta n/\Delta t$ is the flow rate into the reactor. When ideal gas behavior is assumed the above equation 2-1 becomes,

$$t_r = P\,A\,l\,/(\,R\,T\,(\Delta n/\Delta t)) \qquad 2\text{-}2$$

here P, A, l and T are, respectively, the pressure, cross-sectional area, length and average temperature in the reactor. R is the gas constant, and $(\Delta n/\Delta t)$ is the average molar flow rate in the reactor. At high conversion, however, the effect of volume expansion cannot be ignored.

In considering residence times prior to carbon deposition, only the distance, *l*, from the top of the hot zone to the mid-point of the substrate was included. To find residence times for the formation of gaseous and liquid products, the total length of the hot zone was included in equation 2-2. In order to compare product yields at the same residence time, the flow rate for the measurement of deposition onto the quartz substrate was set at one half the flow rate which was used for the gas and liquid analyses. The deposition rate and gas composition were then compared at the same residence time.

The length of the hot zone and the average reaction temperature were calculated from the measured temperature profiles. This calculation took into account the fact that the reaction was slower on the shoulders of the temperature profile at the ends of the reactor than it was at the peak temperature in the center.

Temperatures were weighted by Arrhenius exponential factors to find an average reaction temperature. In a typical experiment 85 % of the reaction was found to have occurred within 10 K of the average reaction temperature. Changing from an activation energy of 25000 K to 30000 K, only changed the calculated average reaction temperature by 1 K and the effective reactor length by 4 %.

The dominant reaction in ethane pyrolysis (18) is given in Reaction 2-2. The

$$C_2H_6 \rightarrow C_2H_4 + H_2 \qquad 2\text{-}2$$

resulting doubling of the number of moles leads to an acceleration of flow, resulting in shorter residence times. The residence times for the pyrolysis of pure ethane have been calculated assuming *($\Delta n/\Delta t$)* in equation 2-2 is twice the flow rate of ethane entering the reactor. This assumption will be tested in chapter 3.

In order to establish the effect of the concentration of ethane, several experiments were performed by diluting the ethane with an inert gas (argon). The partial pressure of ethane was varied while holding the total reactor pressure constant. In this case the residence time was calculated by assuming that *($\Delta n/\Delta t$)* in equation 1 is the sum of the argon flow rate entering the reactor and twice the flow rate of ethane entering the reactor.

3.0 Formation of Light Hydrocarbons and Pyrolytic Carbon on a Quartz Substrate

In previous work, when the product composition was correlated to the deposition rate, research focused on analysis of the light gases (C_6 and less) and the rate of deposition. Since this analysis has not been well established for the pyrolysis of ethane, in this chapter the gas-phase composition and the deposition rate have been examined as a function of the reaction time. This work strives to extend and test the conclusions of previous work on other hydrocarbons to ethane pyrolysis.

3.1 Deposition

The deposition rate of pyrolytic carbon was followed as a function of time for two different quartz substrates: an open-ended quartz tube with a surface area of 7.9 cm^2, and a quartz tube of the same dimensions but closed at both ends, decreasing the surface area to 4.7 cm^2. The rate of deposition per unit area, calculated by assuming the surface area of the substrate did not change with deposition, is provided in Figure 3-1. Deposition onto the open-ended quartz substrate remained relatively constant, at approximately 0.5 ± 0.1 kg s^{-1} m^{-2}, over the 100-minute period illustrated in Figure 3-1. Negligible differences were observed for deposition onto the closed substrate, indicating the deposition onto quartz was directly proportional to the surface area available for deposition. The fact that deposition inside the substrate was at the same rate as outside the substrate indicates the precursor concentration was similar inside and outside the substrate.

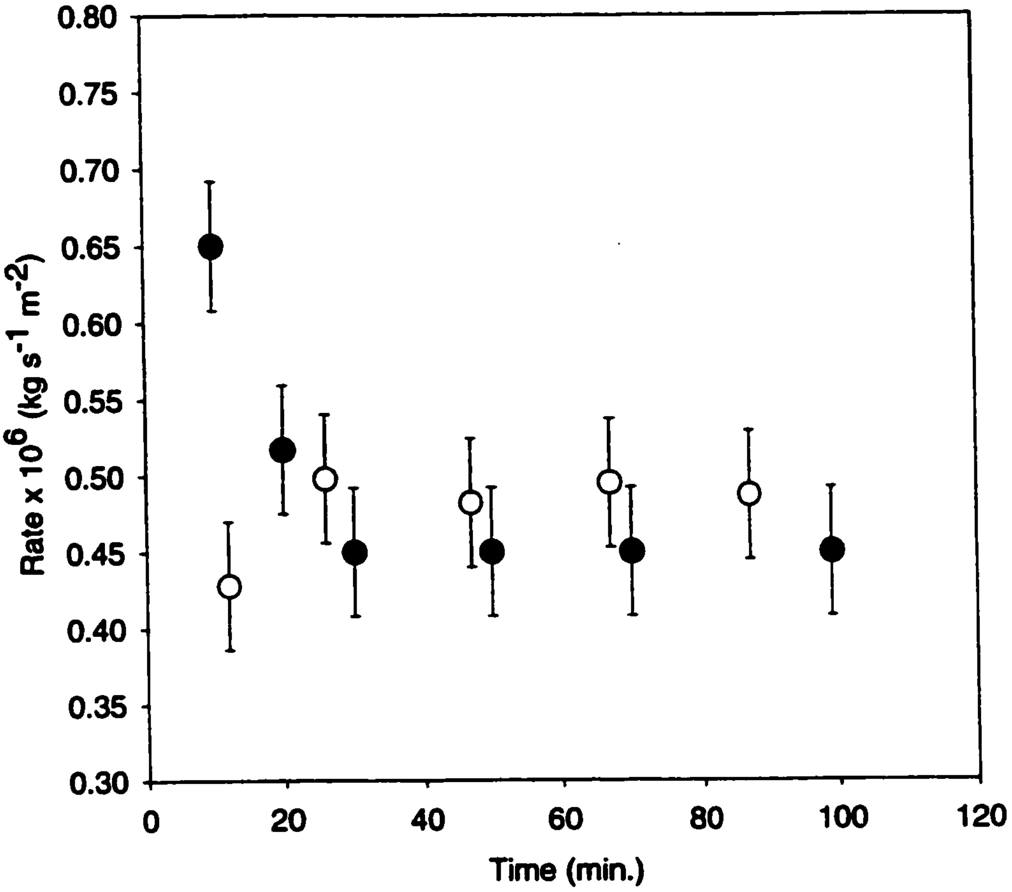

Figure 3-1: The deposition rate per unit area as a function of deposition time and substrate surface area at a pressure, temperature and flowrate of 40 kPa, 1151 K and 26 sccm. The closed circles indicate the rate of deposition onto a closed-ended substrate (4.7 cm^2) and the open circles represent the rate of deposition onto an open-ended substrate (7.1 cm^2).

Figures 3-2 A and B show pictures of the open-ended substrates with and without deposition. In Figure 3-2 B a clear, clean quartz substrate is shown for comparison to Figure 3.2 A, which shows a substrate on which deposition had occurred for 100 min. In Figure 3.2 A a reflective layer of grey pyrolytic carbon is observed. Figure 3-3 provides SEM images of the surface of a quartz substrate before and after deposition. Before deposition a light surface with a few "dirt" particles was observed, indicating a flat, relatively clean surface. Figure 3-3 B shows the edge of a layer of *pyc* on a quartz substrate. The picture shows the coated surface had more three-dimensional structure with a number of hemi-spherical protrusions and a general roughness, which resulted in a brighter image. Both surfaces, however, were relatively even, with little augmentation of the surface upon coating. The SEM images indicated that the surface area of the substrate changed very little upon deposition. There may have been a slight increase in surface area. This is reflected in the rate profile in Figure 3-1, which remained relatively constant.

3.2 Products as a Function of Residence Time

In order to establish the relative proportion of each of the products, the total rate of formation of gaseous products was obtained as the difference between the rate of flow of ethane into the reactor, and the sum of the rates of formation of carbon and liquids. A typical product analysis for the pyrolysis of ethane at a temperature of 1185 K and a pressure of 40 kPa is provided in Table 3-1. All data used in this calculation is provided in Appendix 1. This analysis gives an indication of the relative proportions of 95 % by weight of the individual products. High selectivities for hydrogen, ethylene and

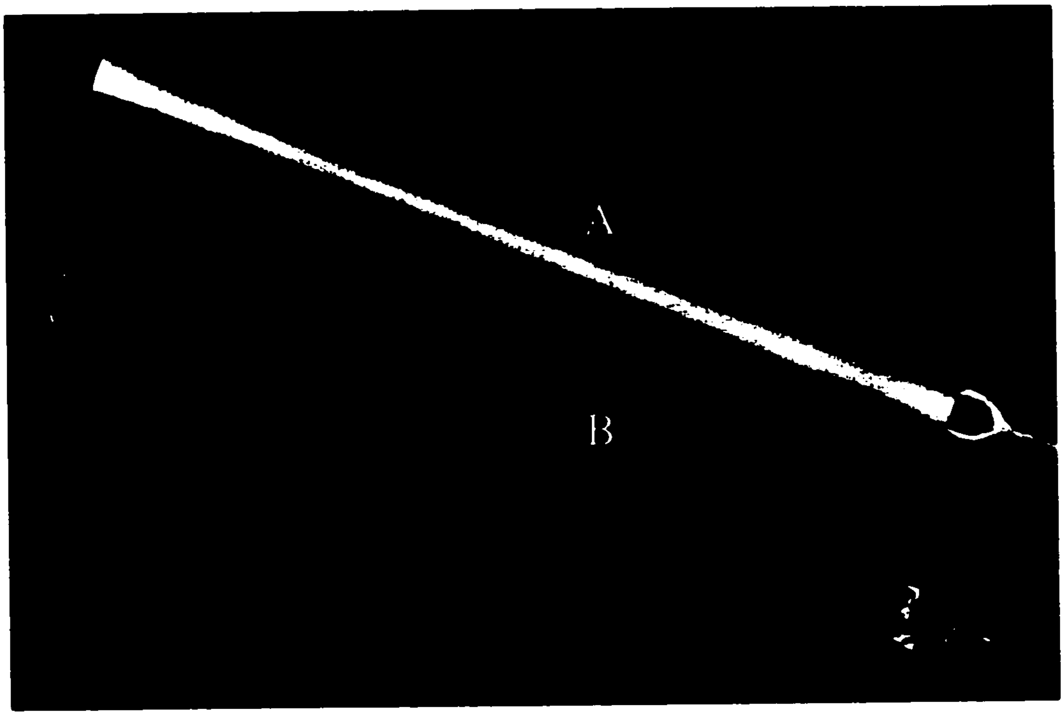

Figure 3-2 Photograph of an open ended substrates with and without deposition. A. A substrate on which deposition has occurred for 100 min.. B. A clear, clean quartz substrate.

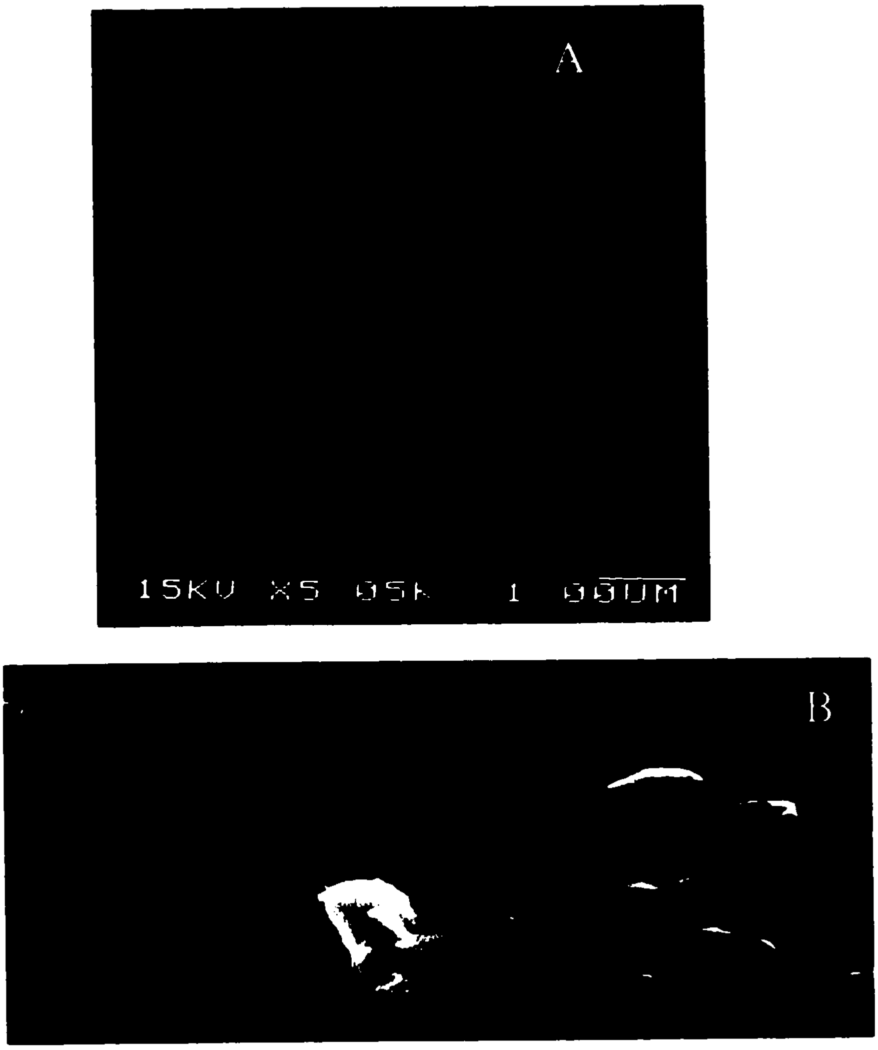

Figure 3-3: SEM images of a clean quartz substrate, A, and of carbon coating on a quartz substrate (coated with *pyc* for 100 min.), B.

methane were observed, with relatively large amounts of acetylene and benzene also present.

Figure 3-4 provides a plot of the experimentally determined ratio of the moles of product exiting the reactor over the moles of ethane entering the reactor as a function of the mass flow rate. From the data it is apparent that the ratio does not deviate significantly from 2, indicating the flow rate is approximately doubled. Thus the assumption made in Chapter 2, that *(Δn/Δt)* is twice the entering flow rate of ethane, is justified.

In order to establish trends in the *pyc* deposition rate, experiments were run at a variety of residence times. From Figure 3-5 it is apparent that the deposition rate at 39.9 kPa reached a maximum at approximately 6 seconds. At lower pressures it appeared the rate of deposition would also reach a maximum, but at longer residence times. The results agreed with the work of Lahaye and Prado on benzene (35) and Feron *et al.* on methane (117), where maximum deposition rates were also observed.

Figure 3-5 also provides the yield of solids deposited within the reactor. Actual carbon yields for a particular residence time are not readily available by this method of analysis. However, it is possible to calculate the average yield as a function of residence time. The average yield was established by fitting the deposition rate as a function of time to a third order polynomial (equation 3-1 where dY_c/dt is the rate of pyrolytic carbon deposition) to obtain the parameters a, b, c, and d. Recognizing that equation 3-1 has no

$$dY_c / dt = a + bt + ct^2 + dt^3 \qquad 3\text{-}1$$

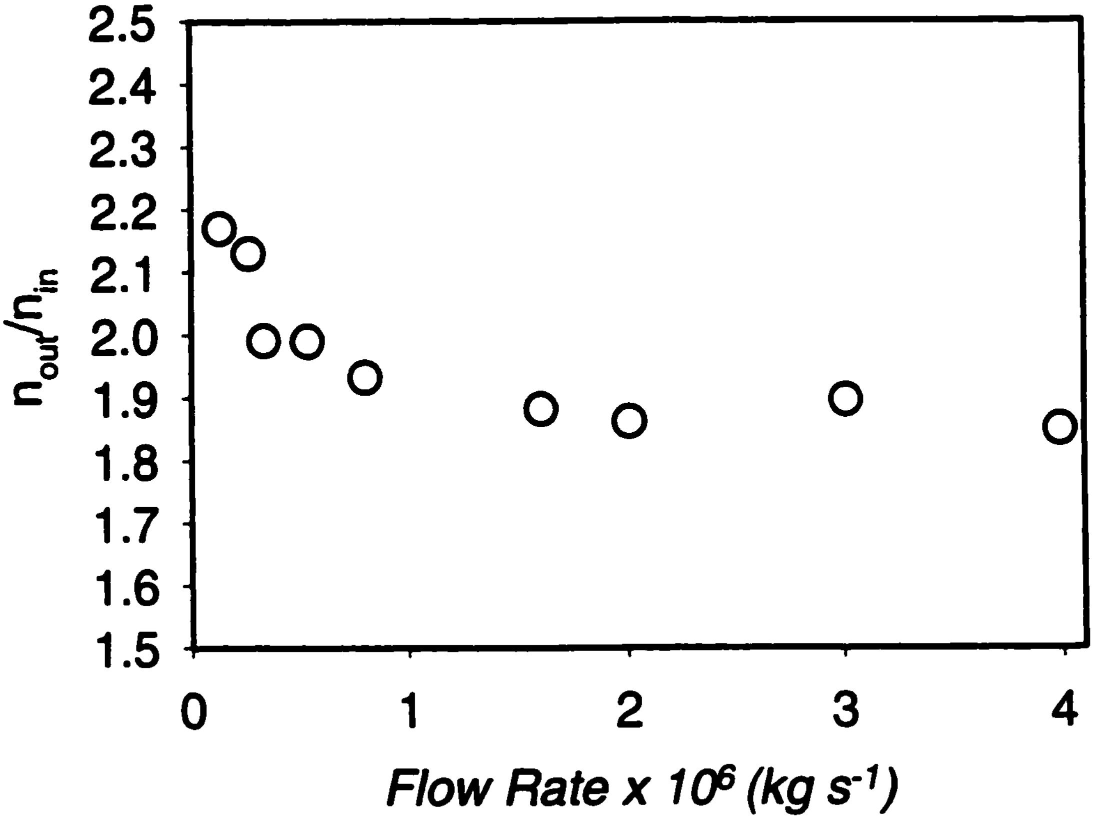

Figure 3-4: The ratio of the total number of moles of product calculated to be exiting the reactor over the total moles of ethane entering the reactor as a function of mass flow rate at a constant temperature of 1185 K and a constant pressure of 39.9 kPa.

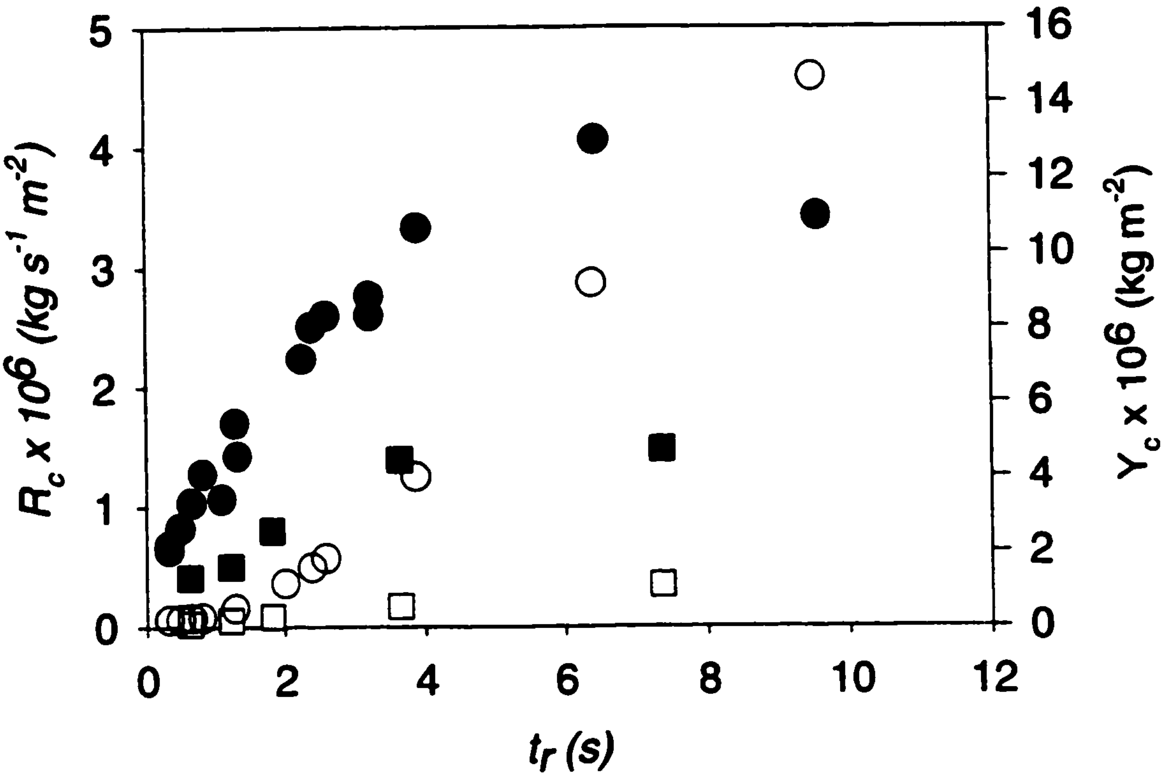

Figure 3-5: The rate, R_c, of deposition of solids onto a quartz substrate, as a function of the residence time, t_r, of gases from the top of the hot zone to the substrate at 39.9 kPa(●), 26.6 kPa(■), and 13.3 kPa(□), and at a constant temperature of 1185 K. The cumulative yield, Y_c, of carbon deposited at a pressure of 39.9 kPa (○) is shown scaled against the right axis. The feedstock was pure ethane.

mechanistic interpretation and is only valid due to the fact that it fits the data, one can integrate to obtain an expression for the yield of deposited carbon as a function of residence time.

$$Y_c = at + bt^2/2 + ct^3/3 + dt^4/4 \qquad 3\text{-}2$$

The average yield is plotted in Figure 3-5. The maximum rate at 6 s is matched by a slight maximum in the slope of the yield.

A typical product analysis is provided in Table 3-1 for a 1 s residence time. The main gaseous products were hydrogen, ethylene, and methane. Analysis of these products as a function of residence time, shown in Figure 3-6, revealed high conversions of ethane to products (>97 mole %) with high selectivities for hydrogen and ethylene at shorter residence times. The minor gaseous products included acetylene, propylene, butadiene and benzene. The mass spectrometric analysis also indicated that trace amounts of other species such as vinylacetylene, toluene and styrene were also present in the gas phase. The intensity of the MS peak for vinyl acetylene was an order of magnitude lower than that observed for the butadiene peak, indicating it was not present in appreciable quantities. Since there were problems in getting nonvolatile material through the gas sampling manifold quantitatively, benzene was used as the cutoff for gas-phase analysis and all larger species were analyzed with the liquid products and are dealt with in Chapter 4.

Table 3-1: Product analysis for the pyrolysis of ethane at a residence time of 1 s, a temperature of 1185 K and a pressure of 39.9 kPa.

Compound	Weight %	Mole %
hydrogen	5.3	43.8
methane	15.3	15.8
acetylene	6.6	4.2
ethylene	53	31.3
ethane	2.8	1.5
propylene	1.1	0.4
butadiene	1.9	0.6
benzene	9.1	1.9
liquid products	4.9	0.40
pyrolytic carbon	0.05	0.07

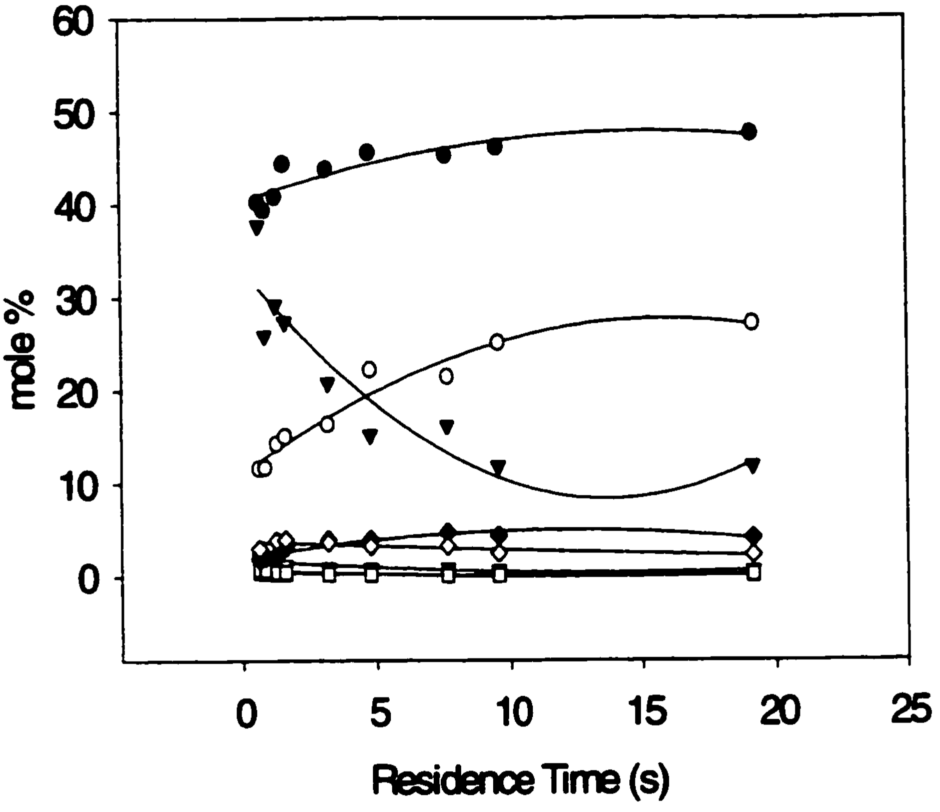

Figure 3-6: The mole percent composition of the major gaseous products, hydrogen (●), ethylene (▼), and methane (○), the minor gaseous products propylene (■), butadiene (□), benzene (◆) and acetylene (◊) and of the reactant, ethane (▽) as a function of residence time, *t*t_r, of gases in the hot zone of the reactor at a pressure of 39.9 kPa.

The minor product concentrations are compared to the deposition rate in Figure 3-7. At relatively short residence times and low *pyc* yields, acetylene and benzene were present in appreciable quantities, whereas propylene and butadiene did not appear to be important products at any residence time. Acetylene reached a maximum concentration at about 1s and declined. Benzene had a maximum at 6s, which is about the same time as the deposition rate.

Acetylene and benzene have been suggested as important precursors of *pyc* formation in other systems (13). It is expected that the concentration of a rate limiting species would have reached a maximum at about the same time as the deposition rate; this was observed for benzene. From these results it is possible that reaction of benzene or some intermediate with a concentration proportional to the benzene concentration was the slow step in forming *pyc*. This is not to say that parallel mechanisms involving direct decomposition of other hydrocarbons are not prevalent under different conditions.

3.3 Rates as a Function of Concentration

If a reactant, intermediate or product is involved in a rate limiting step, then it is expected that the rate of *pyc* deposition (R_c) should be proportional to the precursor concentration. For example, Tesner (56) proposed R_c to be directly proportional to the concentration of hydrocarbon pyrolysed, as indicated in equation 3-3.

$$R_c = 2k_e [C_2H_6] \tag{3-3}$$

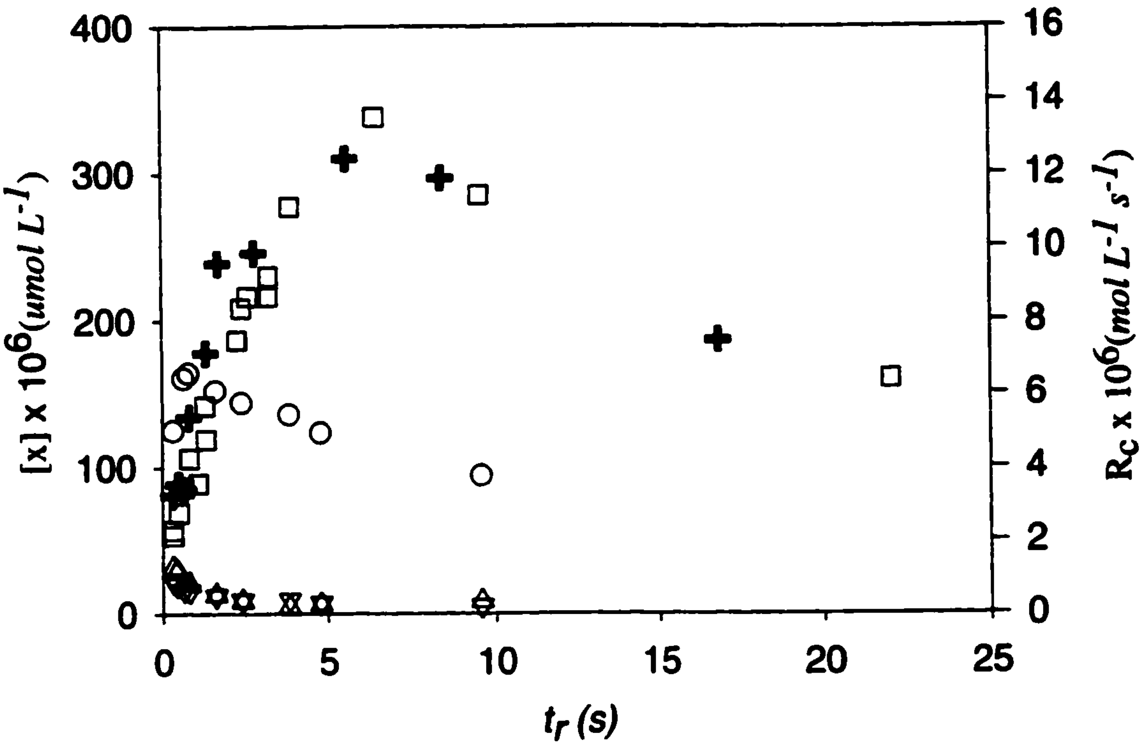

Figure 3-7: The concentration of the minor products, benzene (✚), acetylene (O), butadiene (∇), and propylene (Δ), found in the product mixture as a function of residence time in the hot zone of the reactor at 39.9 kPa. The rate, R_c, of deposition of solids onto the quartz surface per unit volume of the reactor, (☐), is shown scaled against the right axis. The deposition rate and gas composition were measured at the same residence times by using faster flow rates for the gas analysis, as explained in section 2.3.

In order to establish the pressure and concentration dependence of the deposition rate, experiments were performed at several residence times. Results for the reactant, ethane, are provided in Figure 3-8. The data indicate that the deposition rate increased nonlinearly with increasing initial concentration of ethane in the reactor. Comparing Figures 3-1 and 3-6, we see that R_c increased between 0 to 6 s, while the concentration of ethane decreased. These observations support work on other hydrocarbons by Huttinger's group (13, 46, 50-53). It can be concluded that the simplified assumption of a first-order reaction of ethane is not warranted for this system.

The dependence of the deposition rate on the concentration of benzene was also examined. Experiments were performed by varying the flow rate of ethane and argon in the inlet of the reactor while holding the total reactor pressure constant at 53.3 kPa. R_c was determined when the gases had spent 1.1s proceeding from the start of the hot zone to the substrate. In a separate run the benzene concentration was determined when the gases exited after spending 1.1s in the hot zone. Based on results from the pyrolysis of benzene, it has been found that the rate of *pyc* deposition was directly proportional to the initial partial pressure of benzene (50-53). A similar relationship held for the present system. A plot of R_c as a function of the concentration of benzene was nearly linear and passed through the origin, as indicated in Figure 3-9. A plot of the logarithm of R_c against the logarithm of $[C_6H_6]$ had a slope of 1.1 ± 0.1.

In Figure 3-10 a double logarithmic plot of the average rate of formation of benzene, $([C_6H_6]/t_r)$, as a function of acetylene partial pressure reveals a linear relationship with a slope of 3.1 ± 0.2. This observation may indicate that three acetylene molecules, or species with concentrations proportional to acetylene, reacted to form

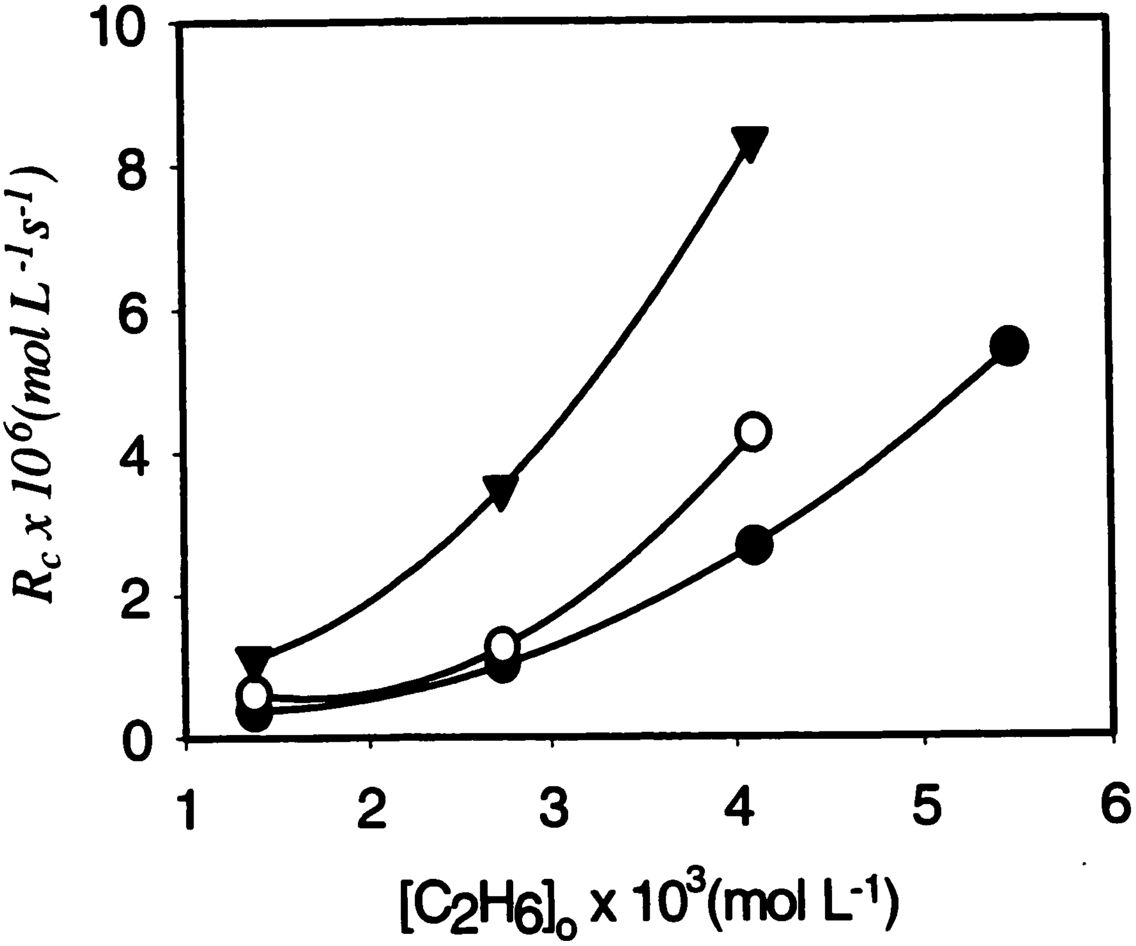

Figure 3-8: The deposition rate as a function of the initial ethane concentration, at a temperature of 1185 K and residence times of 3.7s, (▼), 1.3s , (O) and 0.7s , (●).

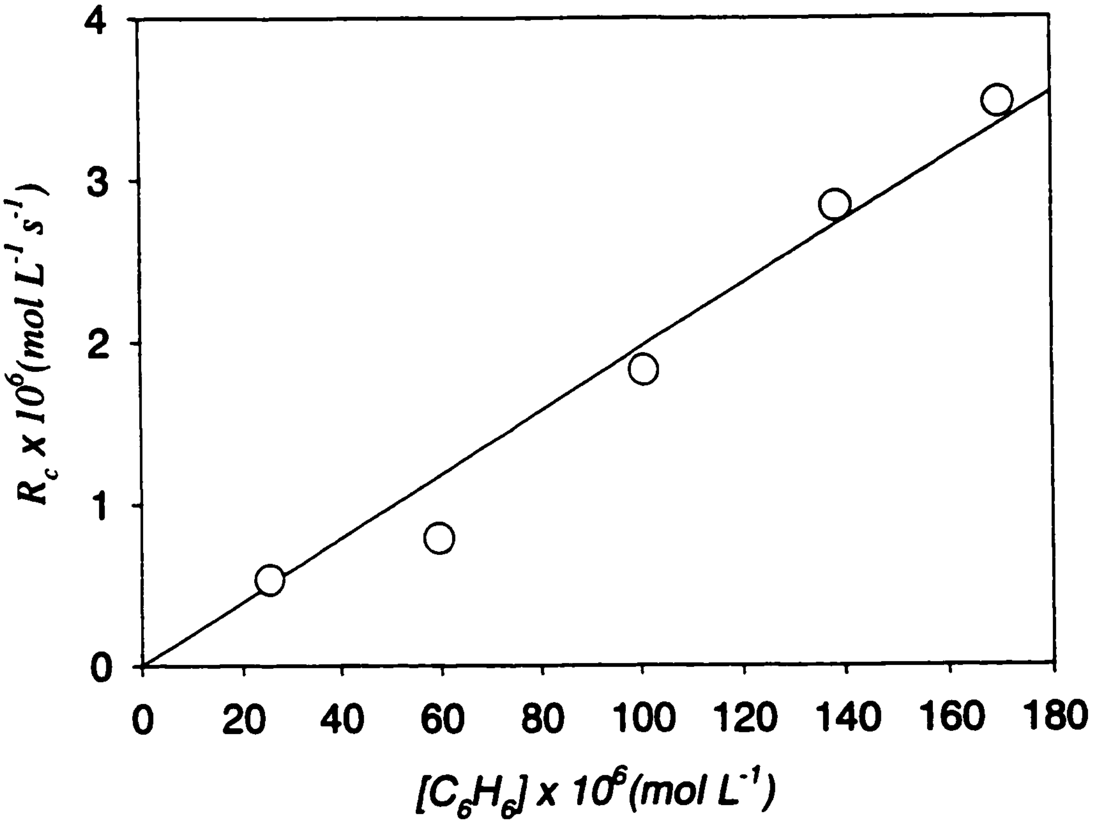

Figure 3-9: The rate of *pyc* formation (R_c) as a function of benzene concentration at a constant total pressure of 53 kPa (using argon as diluent) and a temperature of 1185 K. Circles were experimentally determined by pyrolysing mixtures of ethane and argon. The gases had spent 1.1 s between the top of the hot zone and the substrate, for measurements of R_c, and between the top and bottom of the hot zone, for measurements of [C_2H_6]. The line represents a first order relationship.

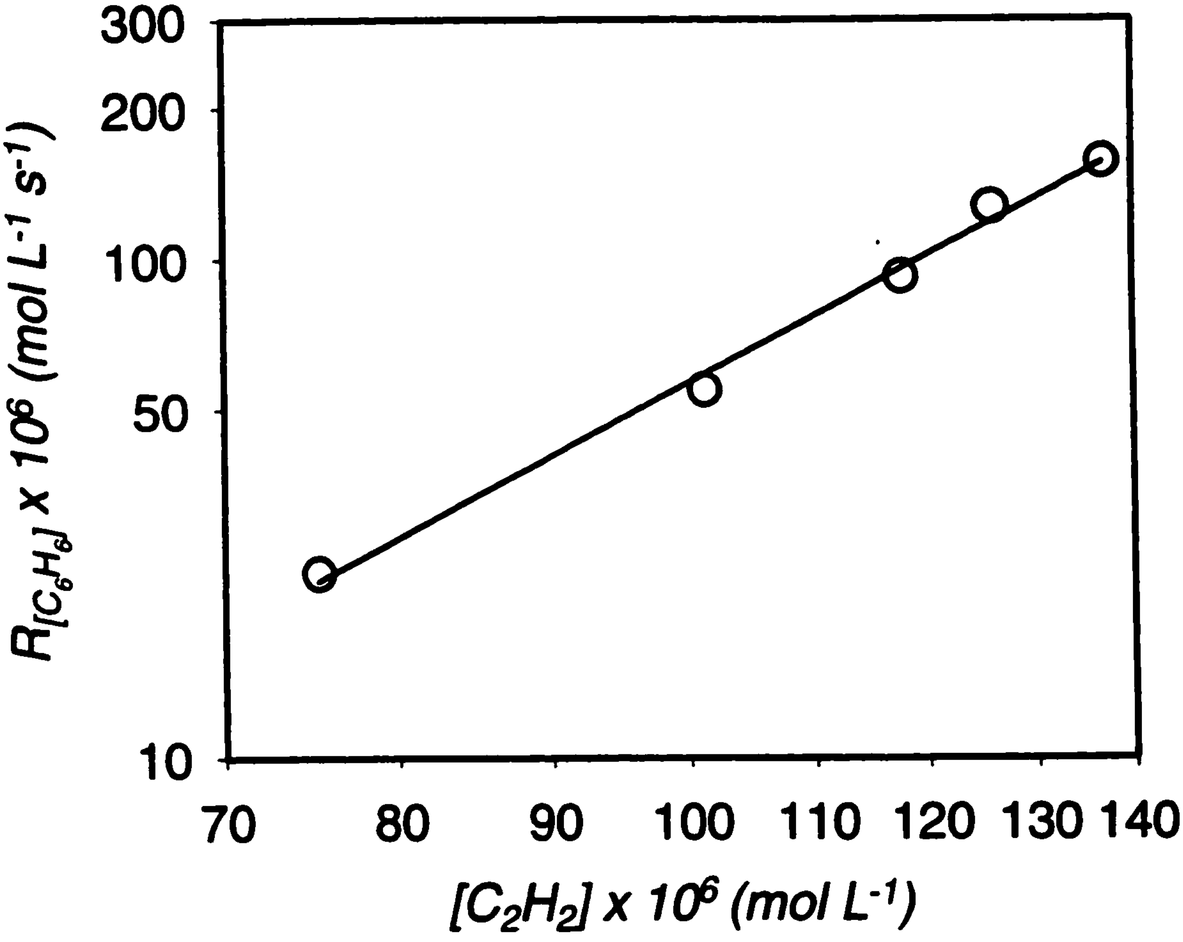

Figure 3-10: Double logarithmic plot of the average rate, $R_{[C6H6]}$, of benzene formation as a function of acetylene concentration for experiments at a constant total pressure of 53 kPa (using argon as diluent), a temperature of 1185 K and a residence time of 1.1 s.

benzene. Some of the relevant literature is consistent with this idea. Westmoreland *et al.* (85) provided a brief review of some of the routes that have been suggested by several researchers for the formation of benzene during pyrolysis and combustion. Based on experimental results from flames and computational results, Westmoreland *et al.* (85) showed the rate of benzene formation can be reasonably accounted for by acetylene addition to form a C_4 radical which may add to another molecule of acetylene to form benzene. Frenklach *et al.* (82) support the addition of 3 acetylene molecules over several steps to form a phenyl radical. Becker and Huttinger (50-53) said benzene is a direct product of acetylene pyrolysis and that it is formed in a third order reaction. Dimitrijevic *et al.* (118), based on experimental results, showed that the reaction is approximately third order with respect to acetylene concentration. This process likely involves a complex series of reactions of radicals. If a step in which three acetylene molecules have combined is rate limiting, then an empirical third order relationship is expected.

Under conditions of high surface area, fast residence time, and low conversion to products, it has been suggested that the formation of surface carbon is due to the direct decomposition of hydrocarbons on the carbon surface (56). A large amount of quantitative data based on a first-order relationship has been tabulated by Tesner (56). Although the mechanistic interpretation of Tesner's work has been questioned (46), a consideration of the rate constants in an empirical sense may be of some use here. From Tesner's work it is found that rate constants for reactions of many aliphatic hydrocarbons are several orders of magnitude lower than those observed for acetylene. If one supposes that many product species are responsible for *pyc* formation, as has been suggested by Tesner (56), Lahaye *et al.* (37), and Huttinger and coworkers (46, 50-53), the rate of deposition may depend on many parallel reactions as indicated below in equation 3-4.

$$R_c = 2k_{et}[C_2H_6]+2k_{ey}[C_2H_4]+ 2k_a[C_2H_2]+ 3k_{pr}[C_3H_6]+ 4k_{bu}[C_4H_6]+ 6k_{ab}[C_6H_6] \quad (3\text{-}4)$$

From Tesner's results (56), $k_{et}, k_{ey}, k_{pr}, k_{bu} << k_a$ and it is expected that, R_c is essentially described by equation 3-5,

$$R_c \equiv 2\ k_a[C_2H_2] + 6\ k_{ab}[C_6H_6] \quad (3\text{-}5)$$

Here the rate constants, k_a and k_{ab}, refer to the empirical reactions 3-6 and 3-7, respectively.

$$C_2H_2 \rightarrow 2\ C + H_2 \quad (3\text{-}6)$$

$$C_6H_6 \rightarrow 6\ C + 3\ H_2 \quad (3\text{-}7)$$

The values of k_a and k_{ab}, calculated from a nonlinear least squares fit of equation 3-5 to experimental data at a 1.1s residence time and several starting ethane concentrations, are $(2 \pm 70) \times 10^{-4}$ and $(3.5 \pm 0.4) \times 10^{-3}\ s^{-1}$, respectively. The standard deviation of k_a is more than an order of magnitude greater than its value, indicating that the direct contribution of acetylene to carbon formation cannot be reliably determined from this data. Dropping this term, we obtain

$$R_c \cong 6\, k_{ab}[C_6H_6] \qquad (3\text{-}8)$$

Fitting equation 3-8 to the data we also obtain a value of $(3.5 \pm 0.3) \times 10^{-3}\ s^{-1}$ for k_{ab}. The consistency of the values of k_{ab} calculated from equations 3-5 and 3-8 agrees with the earlier suggestion that benzene is the major precursor of *pyc* in this system. Moreover, the fact, established in Figure 3-7, that the deposition rate parallels the concentration of benzene indicates this relationship can be extended to longer residence times. This work does not provide evidence for the hypothesized parallel route suggested by Benzinger, Becker and Huttinger (46,50-53) but does not negate the possibility of a slower route to carbon directly from acetylene.

These results do not prove that benzene lies on the pathway from ethane to carbon, nor that the reaction of benzene is the rate-limiting step on this pathway, even though the results are consistent with both of these hypotheses. It is possible that there are other species, whose dependencies on time and pressure are similar to those of benzene, which would also be reasonable precursors for carbon. One possibility is the phenyl radical (71). Its time dependence is expected to be similar to that of benzene, although its concentration might also depend on the concentrations of other radicals present. Heavier aromatic compounds and radicals might also depend on time and pressure in a way similar to benzene. It is not clear whether heavier aromatics can be formed directly from acetylene and small radicals or whether they are formed from benzene.

3.4 Rates as a Function of Temperature

The deposition rate and benzene concentration were examined as a function of temperature from 1100 K to 1185 K. An empirical Arrhenius analysis was used to investigate the rate of deposition (mol L^{-1} s^{-1}) and rate constants (s^{-1}) calculated from equation 3-6. A plot of the natural logarithm of the deposition rate as a function of inverse temperature (shown in Figure 3-11) yielded an activation energy of 412 ± 15 kJ mol^{-1}. The natural logarithm of the pre-exponential factor in mol $L^{-1}s^{-1}$ was 29 ± 2.

A plot of the natural logarithm of rate constants, k_{ab} (s^{-1}) calculated from equation 3-6 as a function of inverse temperature (shown in Figure 3-12) yielded an activation energy of 268 ± 24 kJ mol^{-1}. The natural logarithm of the pre-exponential factor was 21.6 ± 2.5. In this analysis the lowest temperature point was not on the line and was therefore excluded from the regression analysis.

From Reference 56, for the pyrolysis of pure benzene, the Arrhenius parameters given in units of g cm^{-2} s^{-1} Pa^{-1} are -5.8 for the natural logarithm of the pre-exponential factor and 230 kJ mol^{-1} for the activation energy. Converting our results to the same units, values of 259 ± 23 for the activation energy and 2.87 ± 1 for the natural logarithm of the pre-exponential factor were obtained. The temperature dependence from Reference 50 is not available but the value of k_{ab} for the pyrolysis of pure benzene at 1273 K can be calculated to give a value of 5.6×10^{-11} g $cm^{-2}s^{-1}Pa^{-1}$ compared to a values of 1.1×10^{-12} g $cm^{-2}s^{-1}Pa^{-1}$ from Tesner's results (56), also for the pyrolysis of pure benzene, and 4×10^{-10}

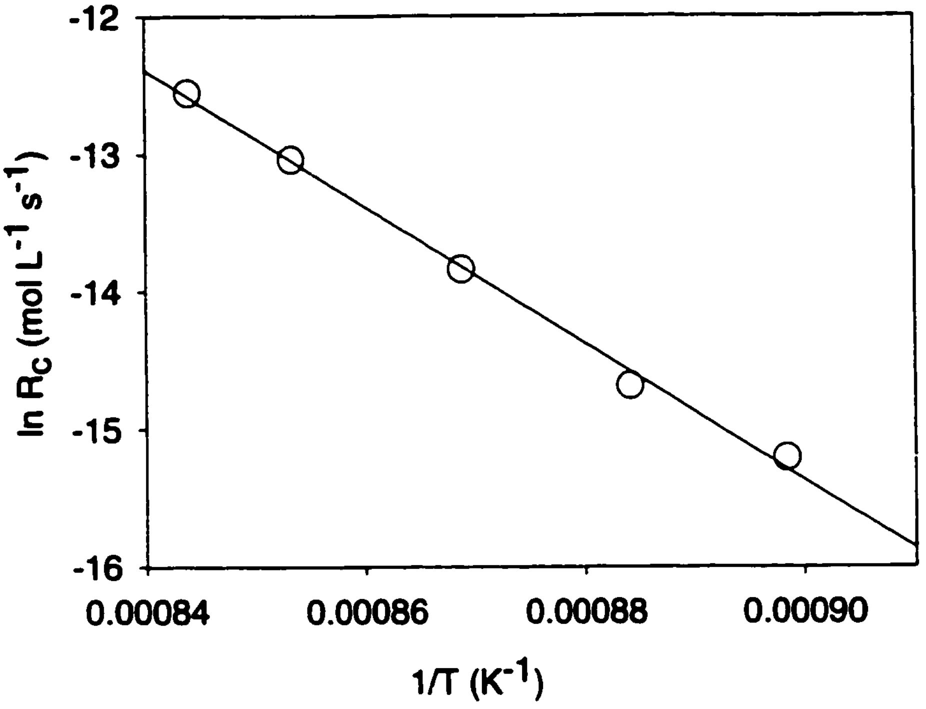

Figure 3-11: A plot of the natural logarithm of the deposition rate as a function of inverse temperature at a 1 s residence time and a pressure of 40 kPa.

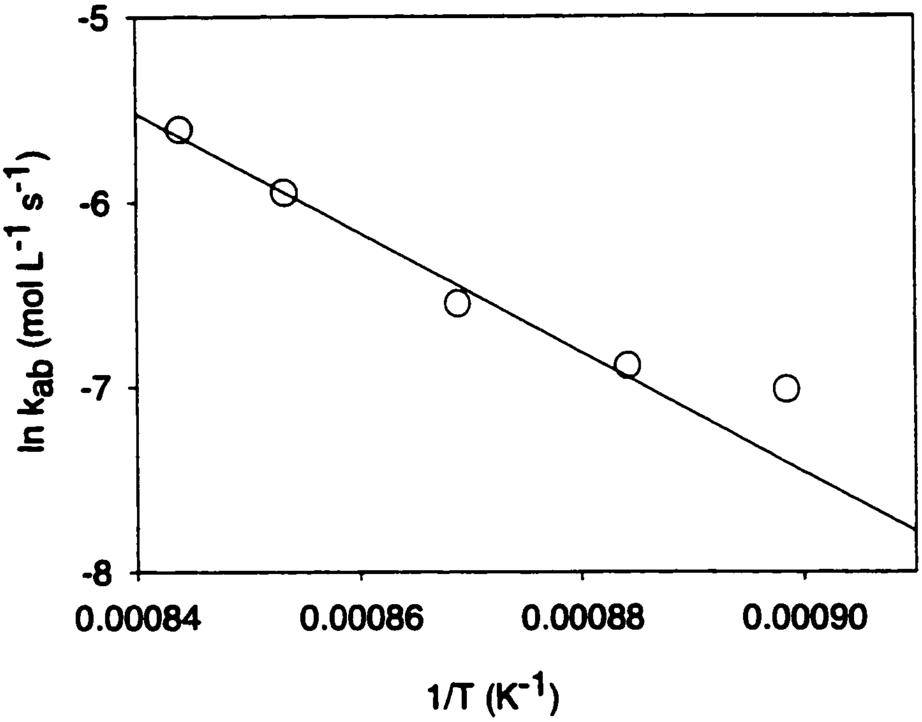

Figure 3-12: A plot of the natural logarithm of rate constants, k_{ab} (s^{-1}), calculated from equation 3-8 as a function of inverse temperature at a 1 s residence time and a pressure of 40 kPa.

g cm^{-2} s^{-1} Pa^{-1} extrapolated from our results. The value of k_{ab} calculated from our results is 7 times faster than that calculated from Huttinger's results (50-53) and 360 times faster than that calculated from Tesner's results (56).

The large difference between the present value of k_{ab} and that calculated from the pyrolysis of pure benzene is consistent with the assumption that it is not the direct decomposition of benzene but some intermediate with a concentration proportional to benzene which represents the bottleneck to carbon formation. Further, the nonlinearity of the Arrhenius plot in Figure 3-12 would support the suggestion of an intermediate. The fact that k_{ab} is larger for the pyrolysis of ethane than for the pyrolysis of pure benzene may indicate that, relative to the benzene concentration, there is proportionally more of this intermediate present in the ethane system than for the pyrolysis of pure benzene. This hypothetical intermediate could be a simple molecule such as the phenyl radical or a complex mixture of large PAHs. The latter possibility will be examined in Chapter 4.

4.0 Formation of PAHs Coincident with Pyrolytic Carbon

In Chapter 3, examination of the gas-phase products present during the deposition of pyrolytic carbon showed the rate of carbon deposition was proportional to the benzene concentration at the point of deposition within the reactor. This would be consistent with the direct decomposition of benzene on the surface, or it may be the benzene concentration paralleled that of the true carbon precursors, perhaps a mixture of large PAHs. In the last decade a few researchers have performed GC-MS analysis of PAHs formed during pyrolysis. A number of new techniques have been developed and used to examine combustion products. There is little doubt that molecular growth and PAH formation are important in combustion. However, there has been little evidence to support their importance in pyrolysis. The aim of the work presented in this Chapter was to extend the archetypal analysis provided in chapter 3 to provide the composition of the liquid products found in the reactor effluent. Numerous studies point out the possible significance of very large PAHs in determining the rate of formation and the structure of *pyc*. However, few studies have provided experimental evidence for the presence of large PAHs. A detailed analysis of the liquid products should provide a measure of the importance of further molecular growth and PAH formation in pyrolysis and allow one to examine the plausibility of these species as carbon precursors.

4.1 Yields of Identified Products

Figure 4-1 shows a typical LC-UV chromatogram of the liquid reactor effluent in which samples were prepared in the manner described in Chapter 2. Peaks are numbered

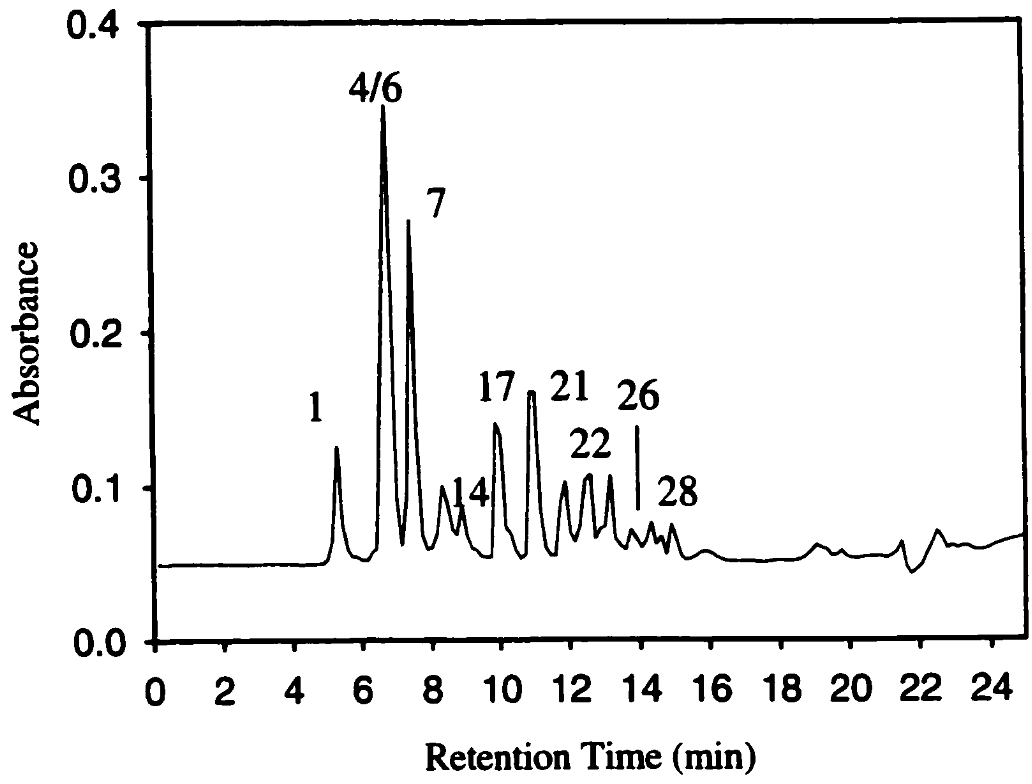

Figure 4-1 Chromatogram from the LC-UV analysis of the liquid products collected at a temperature of 1185 K and a pressure of 40 kPa for a 0.55s residence time. Identities of the numbered peaks are listed in Table 4-1.

and their identities are listed in Table 4-1. The peak labeled 4/6 was identified by GC-MS as a mixture of styrene and indene but was quantified using a styrene standard.

Three liquid samples were obtained at each experimental condition. One of these samples was run, by LC-UV, in triplicate and the others were run in duplicate. Standard deviations of the analyses from the three runs on the same sample were less than 5% by weight. From the gas, liquid and solid results the mass of each component of the product mixture was calculated and converted to weight % as reported in Table 4-1. The mass of gas leaving the trap was obtained as the difference between the mass of ethane entering and the masses of carbon deposited and liquids collected. The weight % of individual components were calculated from the fraction of the rate of material exiting the reactor to the total flow rate of ethane into the reactor. The data presented in the third and fourth columns of Table 4-1 are averages of all the analyses performed at the stated experimental conditions. For the analysis of components of the liquid mixture the standard deviations, calculated from repeated runs, are reported. The yield reported for benzene at 0.5 s was calculated from gas-phase results, with the trap kept warm to allow benzene to reach the gas chromatograph. The yield of benzene from the liquid analysis at this residence time was 67 % of that obtained from the gas-phase analysis because some of the benzene passed through the cooled trap. It is expected that benzene would have the highest vapor pressure of any of the products analyzed by HPLC and therefore would have the largest losses. Conversely, at longer reaction times (slower flow rates) the yields of benzene obtained by gas-phase analysis were less than those obtained by liquid phase analysis. At slower flow rates the trap may have worked more efficiently and the benzene product may have been dissolved in the higher molecular weight liquid products present.

Table 4-1: Analysis of the liquid effluent and deposited carbon for the pyrolysis of 40 kPa of ethane for 0.5s and 3s at 1185 K.

PEAK #	COMPOUND	WT % (0.5	WT % (3 s)
1	benzene	9.1[a]	12.6 ± 2
4/6	indene/styrene	0.50 ± 0.03	1.1± 0.1
7	naphthalene	0.70 ± 0.08	4.1 ± 0.5
14	acenapthylene	0.26 ± 0.03	1.3 ± 0.2
17	fluorene	0.094 ± 0.02	0.24 ± 0.03
21	phenanthrene	0.12 ± 0.03	0.61 ± 0.1
22	anthracene	0.076 ± 0.02	0.42 ± 0.02
26	fluoranthene	0.092 ± 0.02	0.73 ± 0.1
28	pyrene	0.054 ± 0.02	0.64 ± 0.1
	other liquids (not quantified)	3.0	7.2
	pyrolytic carbon	0.05	0.5
	gases	86	71

[a] From gas phase results.

Therefore, for residence times equal to or greater than 3 s, the concentration of benzene was obtained from the HPLC analysis of the liquid products.

A mass balance could not be established because the exit flow rate of gases was not directly measured. However, another test of the validity of these results, a hydrogen/carbon (H/C) balance, was calculated. If the proportion of each product was obtained in an accurate manner then the ratio of hydrogen to carbon entering the reactor should have been equal to the calculated ratio of hydrogen to carbon exiting the reactor. Since pure ethane entered the reactor, the material exiting the reactor should have consisted of 75% by mole hydrogen and 25% by mole carbon. The results in Table 4-1, for a 3.0 s residence time, suggest 71 % of the material exiting the reactor was found in the gas-phase. From the gas-phase analysis the weight % of gas-phase species for these conditions were 5.7 % hydrogen, 17.1 % methane, 6.3 % acetylene, 38.1 % ethylene, 1.9 % ethane, 0.83 % propylene and 1.1 % butadiene. Combining the gaseous and liquid species (not including the 7 % of unknown material) collected beyond the reactor exit and the carbon deposition within the reactor, the products were found to be 74.4% by mole hydrogen, which is only 0.6% below the expected result. A similar result was obtained for a 0.5 s reaction time.

4.2 Liquid Products as a Function of Residence Time

Figure 4-2 provides a plot of the total yield, Y_L, of liquid products collected in the trap as a function of residence time. The results indicate that the maximum yield of liquid products, which is over 30 %, is coincident with the maximum rate of carbon

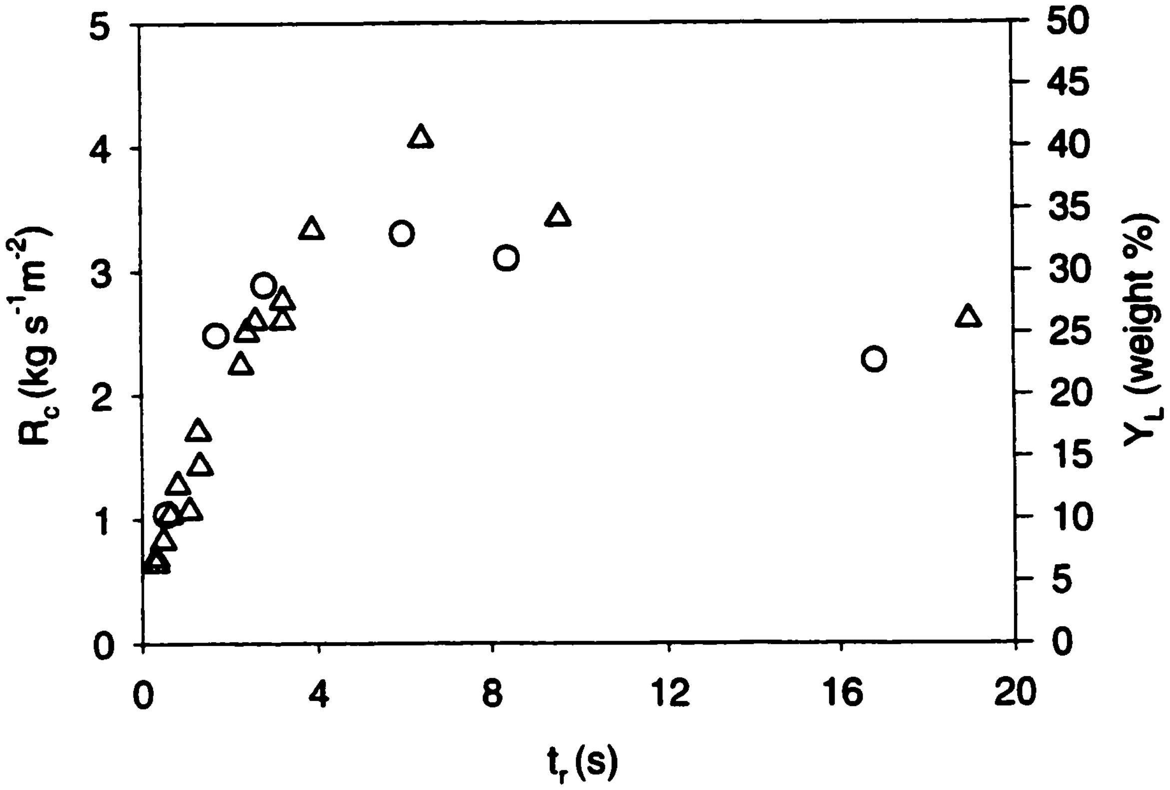

Figure 4-2: Carbon deposition rate, Δ, (left axis) and total yield of liquid products(110), O, (right axis) as a function of residence time, t_r.

deposition. Although not conclusive, the results are consistent with the proposal that the formation of aromatics could be an important step in carbon formation. Lahaye and Prado obtained a similar result from the pyrolysis of benzene (35).

To further test the PAH model one must consider the composition of the liquids as well as the total yield. Figures 4-3 and 4-4 show the yields of a few of the liquid products as a function of residence time. The liquid products were composed primarily of benzene, naphthalene and acenaphthylene (Figure 4-3) and to a lesser extent of styrene/indene, anthracene, fluorene, phenanthrene, fluoranthene, and pyrene (Figure 4-4).

In the pyrolysis of methane, Chen and Back (38) found the maximum concentrations of larger aromatics occurred at longer reaction times than those of smaller species. However, in the present work the yields of most species reached a maximum at about 6 seconds, which is the same time as the maximum deposition rate. The rate of formation of carbon would be expected to be proportional to the concentration of its immediate precursors and to have a maximum at the same time as the maximum precursor concentration. This is observed for seven of the aromatics in Figures 4-3 and 4-4. The coincidence between the maxima for the yields of the aromatics and for the rate of carbon deposition is consistent with the proposal that these species, or closely related species such as their radicals, are precursors of carbon.

The early maxima for styrene/indene and fluorene may indicate that these species are particularly reactive, and decayed to other products soon after they were formed.

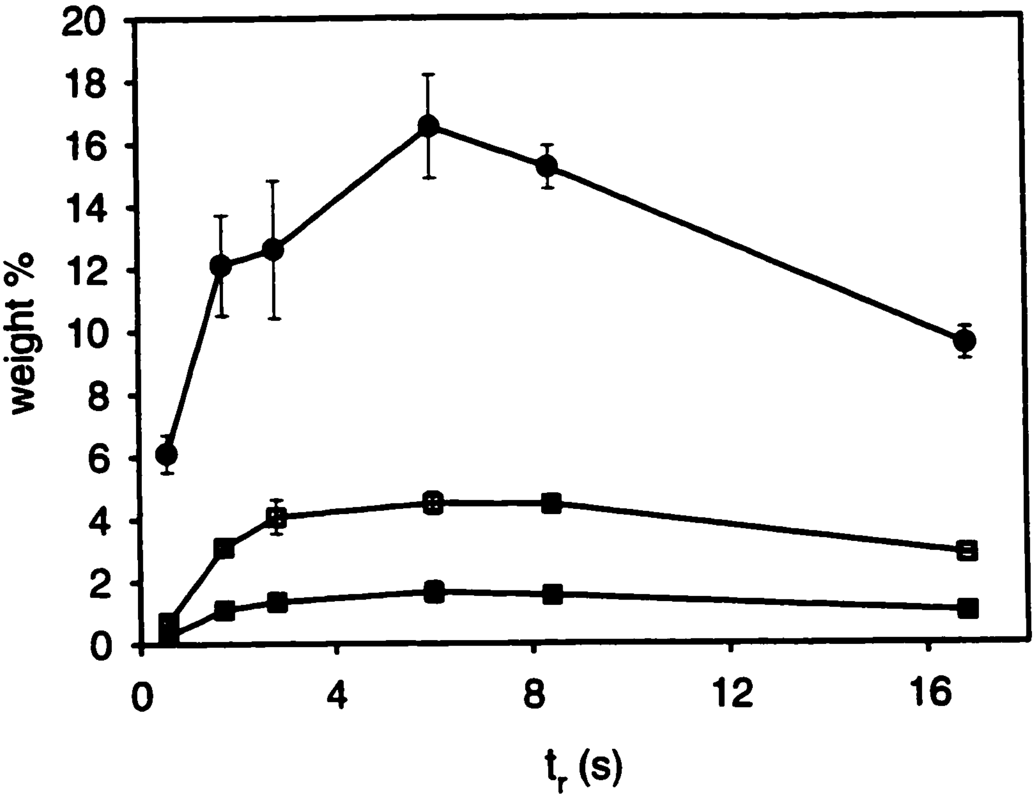

Figure 4-3: Yields of the major aromatic constituents (●, benzene; □, naphthalene; ■, acenaphthylene) found in the liquid product mixture for the pyrolysis of ethane at a temperature of 1185 K and a pressure of 40 kPa. The error bars represent the standard deviations among four measurements.

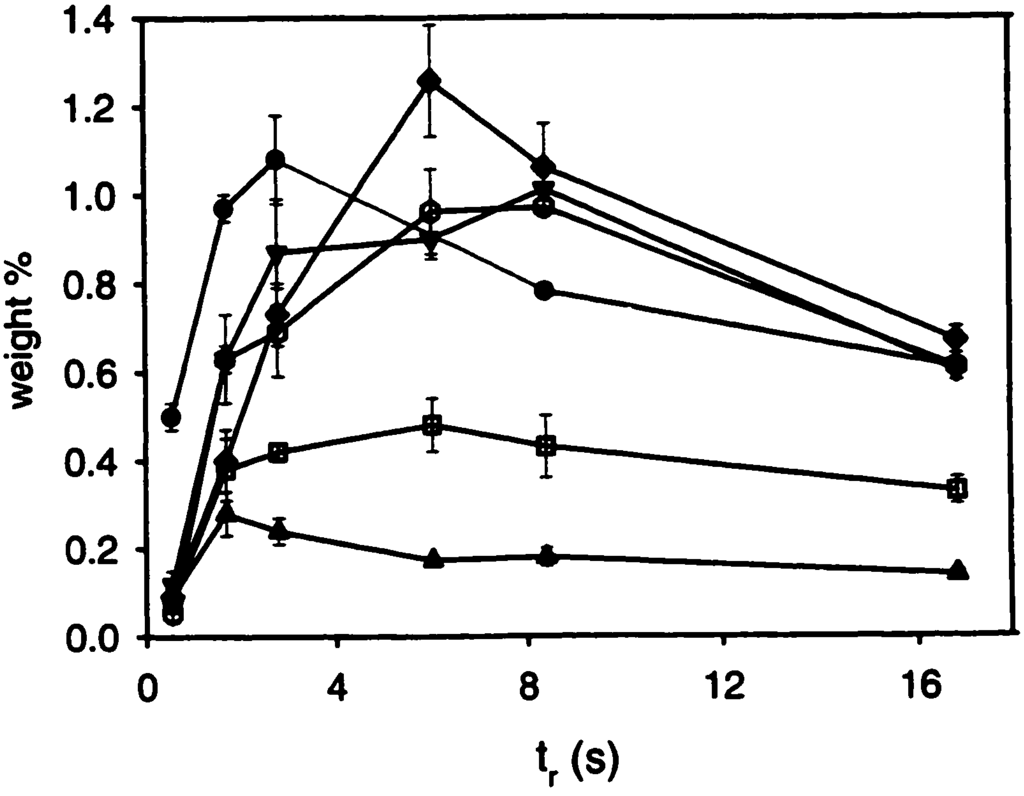

Figure 4-4: Yield of minor aromatics (●, styrene/indene; ▲, fluorene; ∇, phenanthrene; □, anthracene; ◆, fluoranthene; Δ, pyrene) as a function of residence time for the pyrolysis of ethane at a temperature of 1185 K and a pressure of 40 kPa..

4.3 Mass Spectrometric Characterization

From the chromatogram in Figure 4-1 it is clear that species other than those listed in Table 4-1 were present. The composition of the liquid products was extremely complex; a complete chemical composition could not be determined using established analytical techniques.

In order to establish the identity of some of these species a GC-MS analysis was performed. The chromatogram from this analysis is shown in Figure 4-5 and a list of the peaks is given in Table 4-2. Several of the peaks have been identified by comparison of retention times and mass spectra to those of standards. In cases where standards were not available, identifications were based on observed masses and relative retention times and on comparison with the results of other researchers on samples obtained from combustion (73). Due to the stability of PAHs, structural isomers often exhibit similar or identical fragmentation patterns; therefore identifications made without comparison to a standard are speculative. Where only a molecular formula is given in Table 4-2, it is based on the mass of the base peak of the spectrum and an appropriate carbon to hydrogen ratio for a highly condensed PAH. Further, several peaks were not conclusively identified but appeared to be substituted PAHs. The mass spectra for peaks 3, 4, 8, 9, 13, 19, 20, 23, 29, 30 and 31 in Table 4-2 all show fragment ions that may correspond to the removal of ethenyl or ethynyl groups.

Some larger PAHs would have been removed or reduced in concentration by the silica gel column used in GC sample preparation. In order to extend the analysis to larger species an HPLC-APCI-MS analysis was performed. The results are shown in Figure 4-6

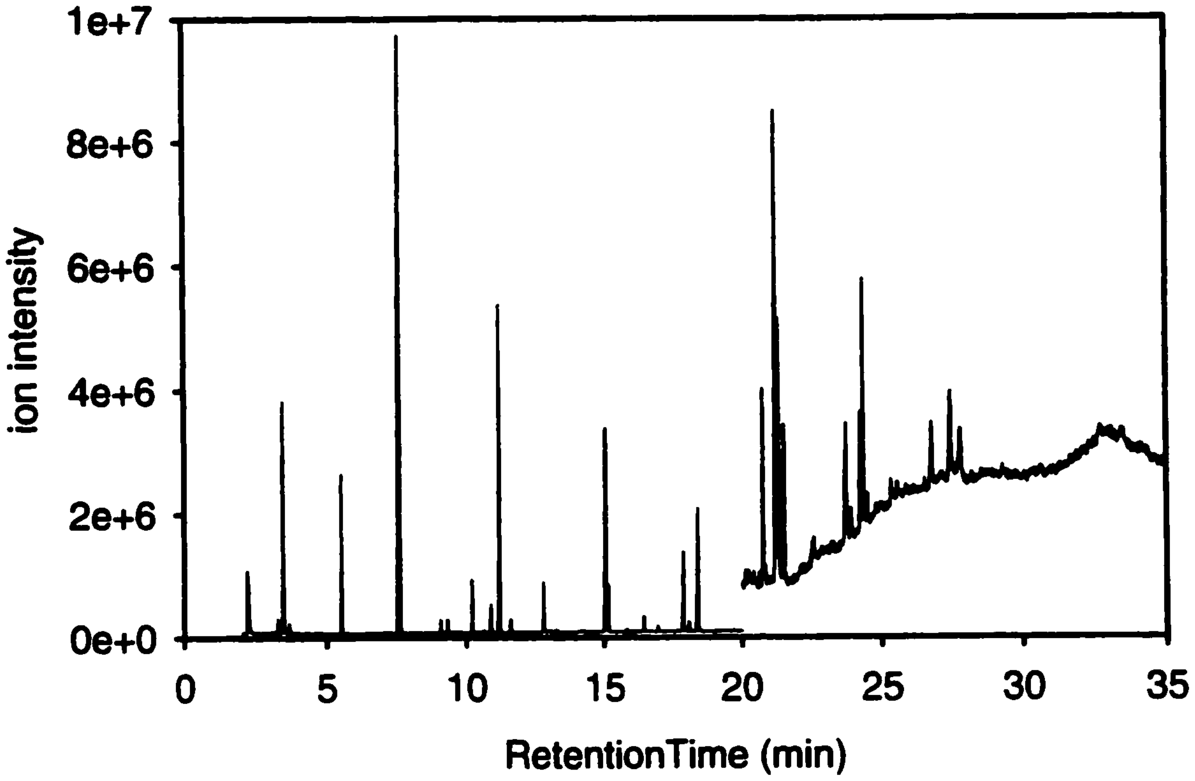

Figure 4-5: GC-MS chromatogram of liquids collected with a 3 s residence time for the pyrolysis of ethane at a temperature of 1185 K and a pressure of 40 kPa. Ion intensities are given for peaks eluting between 0 and 20 min. For longer retention times the obtained intensity has been multiplied by a factor of 40. Some of the peaks are identified in Table 4-2.

Table 4-2: Interpretation of the GC-MS analysis illustrated in Figure 5 for C_6 to C_{22} species obtained from the pyrolysis of ethane for a 3 s residence time.

Peak #	Retention Time(min)	m/z^a	Suggested Identification
1	-	78	Benzene^{b,d}
2	2.2	91,92	Toluene^{d}
3	3.3	102(76,77)	C_8H_6^{e}
4	3.5	103,104(77,78)	Styrene ^{b,d}
5	3.7	131,132	-
6	5.5	115,116	Indene ^{b,d}
7	7.6	127,128	Naphthalene ^{b,c,d}
8	9.1	141,142(115)	$C_{11}H_{10}$ ^{e}
9	9.3	142(115)	$C_{11}H_{10}$ ^{e}
10	10.2	154	Biphenyl^{d}
11	10.6	151,152	$C_{12}H_8$ ^{e}
12	10.7	153,154	$C_{12}H_{10}$ ^{e}
13	10.9	153,154(128)	$C_{12}H_{10}$ ^{e}
14	11.2	152	Acenaphthylene ^{b,c,d}
15	11.6	154	$C_{12}H_{10}$ ^{e}
16	12.6	166	-
17	12.8	166	Fluorene ^{b,c,d}
18	13.0	166	-
19	13.2	165,166(139)	$C_{13}H_{10}$ ^{e}
20	13.3	165,166(139)	$C_{13}H_{10}$ ^{e}
21	15.1	178	Phenanthrene ^{b,c,d}
22	15.2	178	Anthracene ^{b,c,d}
23	15.8	203,204(177)	$C_{16}H_{12}$ ^{e}
24	16.5	189,190	Cyclopenta[*def*]phenant
25	17.0	203,204	$C_{16}H_{12}$ ^{e}
26	17.9	202	Fluoranthene ^{b,c,d}
27	18.1	202	Acephenanthrylene ^{e}

28	18.4	202	Pyrene[b,c,d]
29	19.2	215,216(189)	$C_{17}H_{12}$[e]
30	19.4	216(189)	$C_{17}H_{12}$[e]
31	19.7	216(189)	$C_{17}H_{12}$[e]
32	20.8	226	$C_{18}H_{10}$[e]
33	21.2	226	$C_{18}H_{10}$[e]
34	21.3	228	Benzo[*a*]anthracene or
35	21.5	227,228	$C_{18}H_{12}$[e]
36	23.7	252	Benzo[*b*]fluoranthene[d]
37	23.9	252	$C_{20}H_{12}$[e]
38	24.2	252	Benzo[e]pyrene[e]
39	24.3	252	Benzo[*a*]pyrene[d]
40	24.5	252	$C_{20}H_{12}$[e]
41	26.8	276	Indeno[1,2,3-*cd*]pyrene[d]
42	27.4	276	Benzo[*ghi*]perylene[d]
43	27.8	276	$C_{22}H_{12}$[e]

[a]Mass to charge ratios reported are for base peaks. Where the two largest peaks were comparable in size both are reported. Masses in parenthesis represent relevant fragments. [b]Confirmed by LC-UV. [c]Confirmed by LC-SIM-MS. [d]Confirmed by comparison to a standard. [e]Molecular formula suggested on the basis of base peak mass.

Figure 4-6: Chromatogram from the LC-MS analysis of high mass products (200-400 amu) obtained with a residence time of 3 s for the pyrolysis of ethane at a temperature of 1185 K and a pressure of 40 kPa. The chromatographic conditions involved an acn/dcm gradient, and are described as the 'third set' of conditions in section 2.2. Data for the peaks are found in Table 4-3. In order to obtain better sensitivity several regions of the chromatogram were scanned separately. The retention time ranges (min) and *m/z* ranges scanned were: 0-5, 128-202; 5-10, 200-260; 10-15.5, 250-310; 15-30, 300-360; 30-35, 360-390; 35-55, 390-401. The peaks from 0 - 10 min had the the ion intensities plotted on the left axis; for the peaks from 10 to 30 min and 30 to 40 min the intensities were multiplied by factors of 2.5 and 60, respectively.

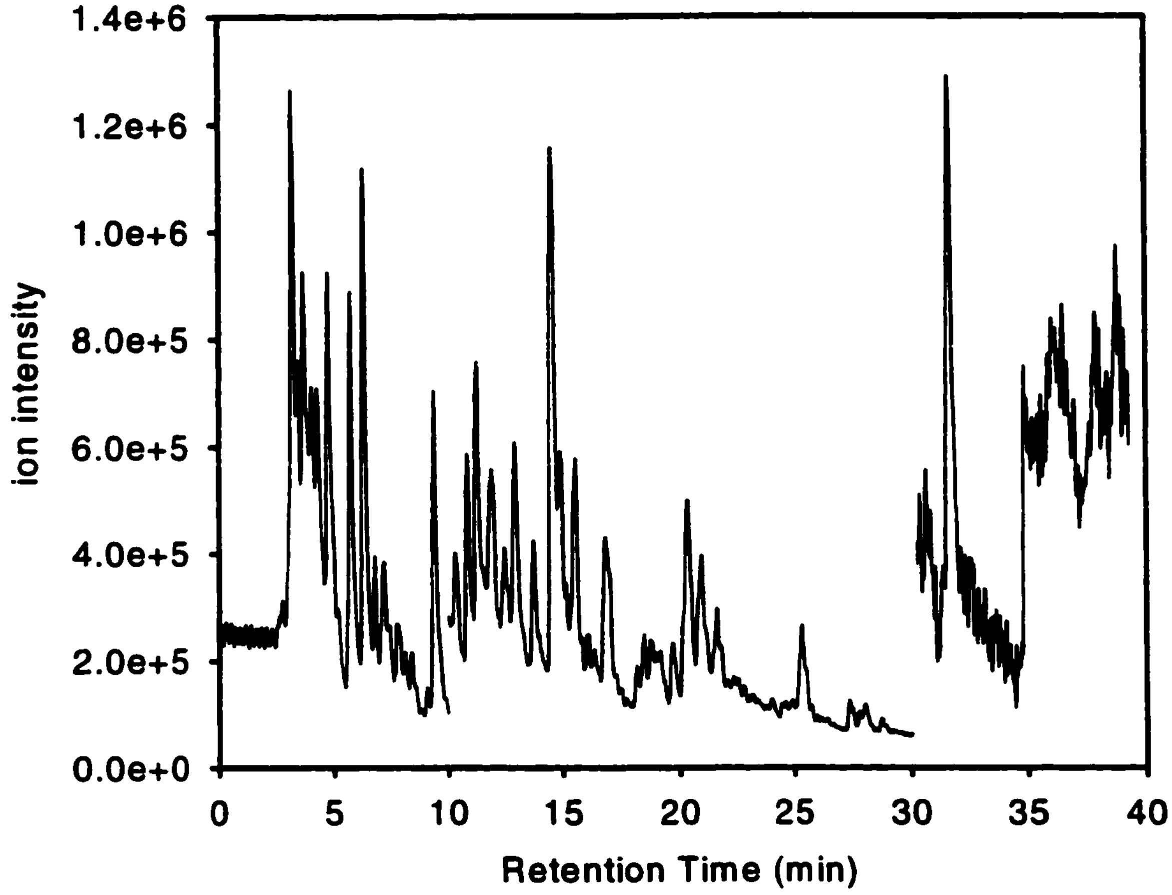
1.4e+6
1.2e+6
1.0e+6
8.0e+5
6.0e+5
4.0e+5
2.0e+5
0.0e+0
ion intensity
0
5
10
15
20
25
30
35
40
Retention Time (min)

Figure 4-6

Table 4-3: LC-MS results for C_{10} to C_{32} species from the pyrolysis of ethane at a residence time of 3s.

Peak	m/z[a]	Peak Intensity	Retention time(min.)
7-28	128-202	-	0-5
32	226	7.7×10^5	5.7
33	226	1.0×10^6	6.3
44	254	2.9×10^5	7.2
36	252	1.7×10^5	7.8
37	252	9.0×10^4	8.1
38	252	9.0×10^4	8.4
39	252	5.7×10^4	9.1
40	252	6.4×10^5	9.4
41	276	2.0×10^5	10.3
45	278	3.8×10^5	10.8
42	276	5.9×10^5	11.3
43	276	3.5×10^5	11.9
46	276	2.2×10^5	12.5
47	276	4.3×10^5	12.9
48	278	2.6×10^5	13.8
49	276	9.6×10^5	14.6
50	300	4.2×10^5	14.9
51	302	1.9×10^5	15.6
52	302,314	5.6×10^4	16.1
53	302,315	4.2×10^4	16.3
54	302	1.3×10^5	16.8
55	300	3.2×10^4	18.1
56	326	5.8×10^4	18.5
57	326	5.3×10^4	18.7
58	326,328	4.2×10^4	19.1
59	326	4.6×10^4	19.7
60	326	1.6×10^5	20.4

61	328	$1.2x10^{5}$	20.9
62	328	$8.1x10^{4}$	21.6
63	326	$2.8x10^{4}$	22.5
64	350	$9.6x10^{3}$	24.0
65	350	$7.2x10^{4}$	25.3
66	350	$2.5x10^{4}$	27.4
67	326,350	$2.3x10^{4}$	28.0
68	350	$9.6x10^{3}$	28.7
69	374,376	$1.2x10^{4}$	30.4
70	374	$9.1x10^{3}$	31.6
71	378	$1.1x10^{3}$	32.5
72	400	$2.2x10^{3}$	36.9
73	398	$2.0x10^{3}$	39.4

[a] Peaks reported as M+; M+1 peaks were also observed. Where 2 masses are reported compounds were not separated.

and interpreted in Table 4-3. In Figure 4-6 peaks 7-28 from the GC-MS analysis were eluted together in the first 5 minutes, after which peaks 32 to 43 were separated and eluted in the 5-12 min. region. The LC analysis in Table 4-3 includes additional peaks, 44-73, which were not observed by GC. Peaks 44-73 ranged in mass from 252 to 400 amu. The combination of mass and elution behavior suggests these species represented larger "parent" PAHs (119) and PAHs with side chains, as observed in the GC analysis. Although there is little doubt these species were large PAHs, the number of possible structural isomers (119) which may elute in this region combined with the lack of standards and the low signal to noise ratio associated with APCI makes it difficult to suggest the identity of these species.

The GC and HPLC analyses indicated many of the same PAHs observed in high temperature combustion (73) were observed in these pyrolysis samples. Unlike high temperature combustion samples (73) the analysis indicated the presence of a significant number of PAHs with attached ethenyl and ethynyl groups. The presence of these species provides some experimental support for the acetylene addition mechanism (73, 58).

It has been suggested (73) that PAHs larger than ovalene (398 amu) cannot be efficiently eluted using current column technology. Therefore, a fourth analysis was undertaken. DLI was used to look at the 300- to 1000-amu range. In Figure 4-7 one can observe mass "clusters" in the range 300 - 600 *m/z*. Moreover, there appears to be a trend in the data, where each cluster is separated by 12-14 *m/z* units. The average spacing between clusters is 12.7 amu, which corresponds to one carbon atom and either zero or one hydrogen atom.

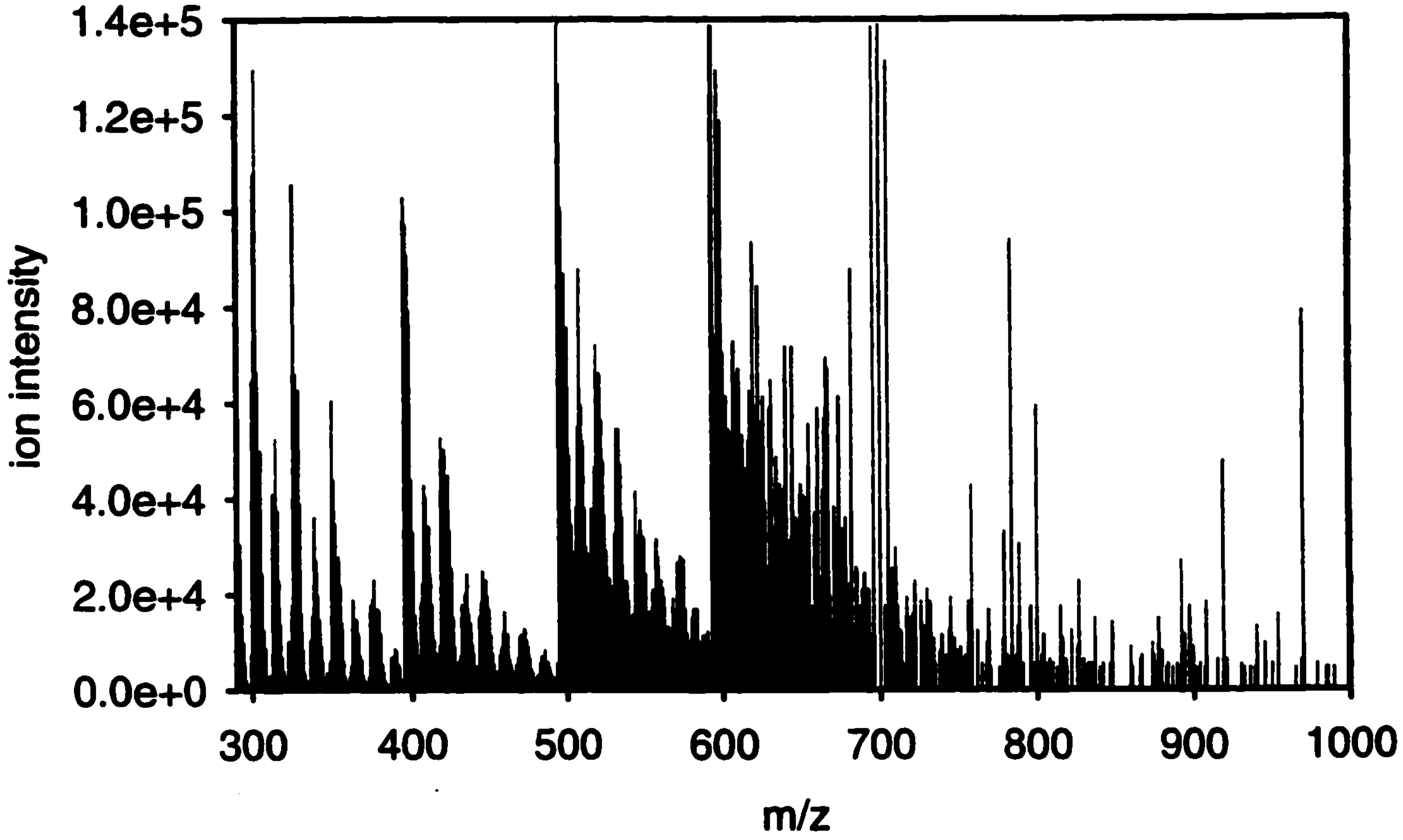

Figure 4-7: Mass spectrum obtained by direct liquid injection for the 290-1000 *m/z* range for a sample obtained with a 3 s residence time. The peaks from *m/z* 300-400 had the ion intensities on the left axis, for the peaks from *m/z* 400-500, 500-600, and 600-1000 the plotted intensities were multiplied by factors of 10, 220, and 900, respectively.

From 300 to 500 amu, there is a further tendency for every second cluster to be more intense than its neighbors. The average spacing between these intense clusters is 25.4 amu. For addition of acetylene units, the spacing would be 26 amu. For growth of linear aromatics, such as from hexacene to heptacene, the increment would be 50 amu. For consolidated growth of fused ring systems, such as phenanthrene to pyrene, the increment would be 24 amu. The observed increment is between 24 and 26 amu, suggesting that growth may occur by addition of acetylene units, accompanied by consolidation and partial dehydrogenation as suggested in Reference 58. Furthermore, the masses of the more intense clusters are consistent with molecular formulas having an even number of carbon atoms. This finding is reinforced by the results in Table 4-1, where only two species, indene and fluorene, have odd numbers of carbon atoms. In Table 4-2, 70% of the species listed have masses which correspond to aromatic compounds with even numbers of carbon atoms. Of the additional species listed in Table 4-3, only 2 masses (*m/z* = 314 and 315) correspond to aromatic compounds with odd numbers of carbon atoms.

4.4 Estimation of the Yields of Large Hydrocarbons

Since a mass spectrometer detects individual ions, it is sensitive to the molar concentration. To find the mass concentrations or weight % of material the ion intensity will be multiplied by the *m/z* to provide the 'mass corrected' ion intensity.

Figure 4-6 shows that the ion intensities of species decreased as the chromatographic retention times increased. The logarithm of the mass corrected intensity for each chromatographic peak, taken from Table 4-3, is plotted as a function of *m/z* in

Figure 4-8. Figure 4-7 shows the ion intensities for mass clusters also decreased with increasing mass up to the 700-*m/z* unit range. The logarithm of the maximum peak intensity, for each cluster in Figure 4-7, times *m/z* is also plotted as a function of *m/z* in Figure 4-8. This figure reveals that there was a linear relationship between the logarithm of the mass corrected intensity and *m/z*. Overlap in the intensities of the species analyzed by LC-MS and DLI was observed in the 300- to 400-*m/z* range. However, species separated chromatographically began to fall off in intensity at 350 *m/z*. It is possible that species with *m/z* above 350 were not eluted from the column efficiently. Above 600 amu the ion intensity from the sample had the same order of magnitude as the background. The straight line in Figure 4-8 is based on the DLI data ranging from 300 to 600 amu and has a slope of (-1.0 œ 0.1) x 10^{-2}, indicating that the mass corrected intensity decreased by an order of magnitude for each increase of 100 amu in *m/z*.

Since the weight % of species ranging in size from naphthalene to pyrene has been established in Table 4-1 it is possible to use the ion intensities, plotted in Figure 4-8, to estimate the concentrations of the higher mass species. The legitimacy of this estimation depends on the molar sensitivity of the MS toward PAHs remaining constant over all mass ranges. In other words there should be no mass discrimination in the introduction, selection and detection methods. This appears to be a reasonable approximation for naphthalene, phenanthrene and pyrene, for which the molar sensitivities for the M+ ions (in units of intensity amu mol^{-1}) were found to be 7 x 10^{16}, 4 x 10^{16} and 5 x 10^{16}, respectively. However this is not necessarily true for larger mass species. Therefore, due to possible mass discrimination in the procedure, estimation of the weight % of high mass

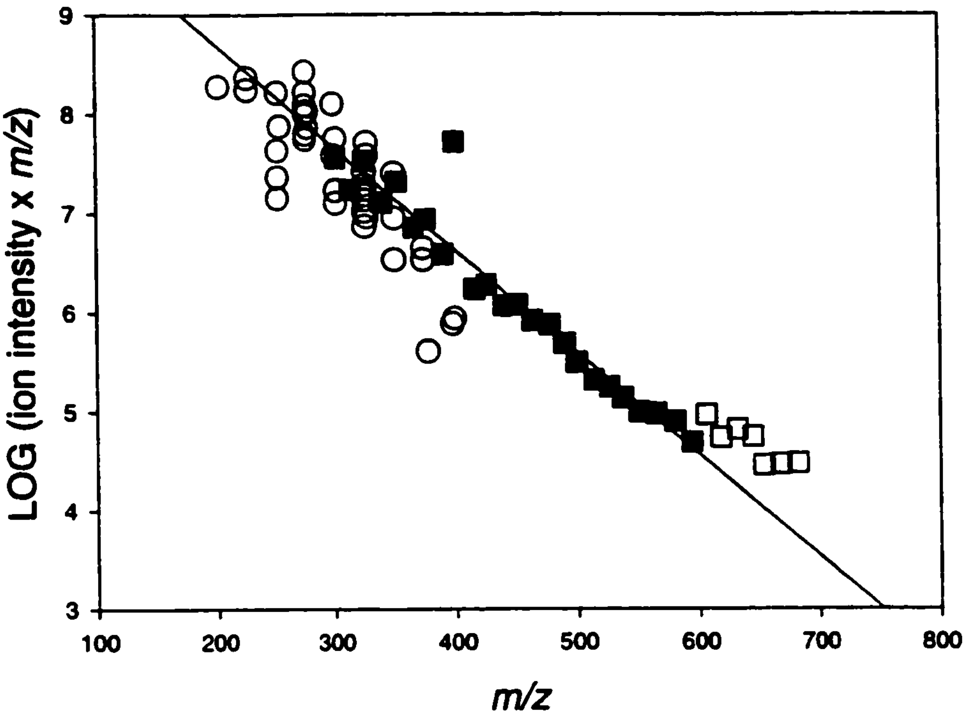

Figure 4-8: The logarithm to a base of 10 of the maximum intensity times the *m/z* for each chromatographic peak, taken from Table 4-3 (open circles), and the maximum peak intensity, for each cluster, times the *m/z* for each peak, taken from Figure 4-7 (squares), as a function of *m/z*. The regression line is calculated from the DLI results (Figure 4-7) in the 300- to 600-*m/z* range. Open squares indicate data in which the background and signal were of the same order of magnitude.

species, where standards are not available, can only be assumed accurate to within an order of magnitude.

For a 3s residence time, Figure 4-2 shows that the total yield of liquid products was 28.9%, leaving 71.1% of gaseous products. Among the liquids, benzene had a yield of 12.6%. Therefore, the total yield of products in the 2- to 100-amu range was 83.7 %. Species in the range from 100-200 amu, calculated from the data in Table 4-1, made up 7.8 wt % of the material. By assuming the molar sensitivity remained constant for all masses the proportions of larger species were estimated from the mass corrected ion intensities indicated in Figure 4-8. Since the wt % of pyrene was established in section 3.2. it was used as an internal standard for this analysis. Species in the range from 200 to 300 were calculated from the LC-MS peak intensities in Table 4-3 to make up 6.7 wt% of the products and 1.28 wt % for the 301- to 400-*m/z* range. Species from the DLI results shown in Figure 4-7, in the ranges from 300-400, 400-500 and 500-600 *m/z* were calculated to make up approximately 0.64 wt%, 0.028 wt%, and 0.0039 wt%, respectively. Of the 28.9 wt.% of liquids collected, 96 -98 wt% could be accounted for in this way, providing additional credibility to the analysis. In the 300- to 400-*m/z* range data was obtained from the LC-MS analysis and the DLI analysis. In this overlap region the wt. % calculated from the chromatographically separated results and the DLI results differ by a factor of two. The LC analysis separates structural isomers whereas these species are not distinguishable by the DLI analysis. This result in the 300- 400-m/z range indicates that the weight % estimated by DLI for higher mass ranges will be underestimated.

4.5 Diffusion of Hydrocarbons to the Reactor Surface

Given an estimate of the relative proportions of the aromatics it is possible to consider the mass transport of these species to the reactor surface. The diffusion limited surface deposition rate is described by equation 4-1. Here C_i is the molar concentration of

$$R_D = r\, k_D\, C_i\, M_i / 2 \qquad \text{4-1}$$

species *i*, estimated from data in sections 3.1 and 3.4; r is the radius of the reactor; M_i is the molar mass of species *i* and k_D is the rate constant for radial diffusion to the reactor surface.

The rate constant for diffusion to a cylindrical surface in the presence of laminar flow was obtained from reference 120. In equation 4-2 D_{mi} is the coefficient of diffusion

$$k_D = 3.6 D_{mi} / r^2 \qquad \text{4-2}$$

for a binary mixture of rigid spheres (122), given in Equation 4-3. Here k_b is the

$$D_{mi} = (k_b^3\, T^3\, L\, (M_m + M_i) / (\pi^3\, 2\, M_m M_i))^{1/2} / P\, \sigma_{mi}^2 \qquad \text{4-3}$$

Boltzmann constant, L is Avogadro's number, P is the pressure and σ_{mi} is the average collision diameter. For each calculation the mixture was assumed to consist of the diffusing species, *i*, in a uniform gaseous medium, *m*. Since it was established in chapter 3 that the number of moles of material exiting the reactor were approximately twice the number entering, a molecular weight, M_m, of 15 amu was assumed for the medium in equation 4-3. The literature value for methane was used to represent the collision diameter, σ_m, for the medium (122). The collision diameters, σ_i, for the aromatics were estimated from their densities, assuming a spherical volume for each molecule. For benzene this method estimated the collision diameter to within 20 % of the literature value (119). For species above mass 202, where identification was speculative, a value of 1.37 g/mL (the density of coronene, a 300 amu PAH) was used. For all species, a deviation of 20 % in the density resulted in less than a 5 % change in the rate constant. Average collision diameters, σ_{mi}, were calculated as the arithmetic mean of σ_i and σ_m.

Table 4-4 lists the mass flux to the reactor surface for species which were identified and quantified with standards as discussed in section 4.2, and provides an approximation for the higher mass ranges based on the estimates of yields provided in section 4.4. The results in Table 4-4 indicate that each of the aromatics which were quantified could account for the experimentally determined deposition. Only 0.8 % of the mass of benzene which diffused to the surface would have had to stick to account for all the deposited material. There were sufficient PAHs present in the system to allow for formation of the observed amount of carbon by direct chemical decomposition on the surface from the gas phase.

According to Chen and Back (38), PAHs in the 500-800 amu range may be large enough to condense to liquids at the temperatures of industrial pyrolysis (1100-1200K).

Table 4-4: The diffusion limited rate of mass transport of several aromatics to the reactor surface, compared with the experimentally determined deposition rate, R_c, for a 3 s residence time.

Species or mass range (*m/z*)	R_D (kg m^{-2} s^{-1})*10^6
benzene	320[a]
naphthalene	85[a]
acenapthylene	26[a]
phenanthrene	12[a]
anthracene	8.3[a]
fluoranthene	14[a]
pyrene	12[a]
100-202	190[a]
203-300	100[b]
300-400	17[b], 7[c]
400-500	0.4[c]
500-600	0.03[c]
R_c	2.7[d]

[a] Calculated from species quantified using standards as described in section 4-1 and 2. [b] Estimated from chromatographically separated species as described in section 4-4. [c] Estimated from DLI results as described in section 4-4. [d] Actual deposition rate obtained experimentally as described in Chapter3.

Particle inception during combustion is suspected to occur when PAHs of 400 - 800 amu are present (56). The present work shows species of this size are present in the pyrolysis system. The observed rate of carbon deposition was 15 to 36 % of the estimated rate of diffusion to the surface of molecules in the 300 - 600 amu range. Without standards it is not possible to accurately determine the concentrations of these high mass species. The results presented here provide estimates which are expected to be within an order of magnitude at the highest masses. Given this uncertainty for high mass species physical condensation on the surface followed by dehydrogenation is also possible. A third possible mechanism, condensation as an aerosol followed by deposition, cannot be tested by the present results, but will be the subject of the following chapter.

5.0 Observation and Preliminary Characterization of a Condensed Phase

In Chapter 4 PAHs were observed which were postulated to be large enough to condense at reactor temperatures. These species could have formed an aerosol in the hot zone of the reactor. Numerous studies have indicated the possible significance of a condensed phase in the deposition of *pyc*. However, few have provided experimental evidence for the presence of an aerosol in the hot zone (36). The following analysis establishes the presence of an aerosol.

Characterization of this aerosol is also relevant to the early stages of soot formation in combustion systems and provides further confirmation of the proposed particle inception processes.

5.1 *In-situ* Observation

The main criticism of previous attempts to sample and characterize precursor material has been the use of cold probes, which disturb the system being analyzed. The counter flow reactor, described in Chapter 2, allowed examination of material that had not come into contact with cooler regions of the reactor.

The reactor was examined visually and photographed with a digital camera. The upper image in Figure 5-1 shows the hot zone of the reactor, viewed from above, with fast flows (52 sccm) of ethane in the top and of argon in the bottom. At this flow rate of ethane it was shown in Chapter 3 that very little carbon was deposited on the reactor walls. The irregular, bright circle in Figure 5-1A corresponds to the reactor wall, on which there was a deposit of coke from previous runs. The gas in the centre of the reactor was dark. In the lower image the flows of ethane and argon were reduced to 6 sccm. At this flow rate, it was

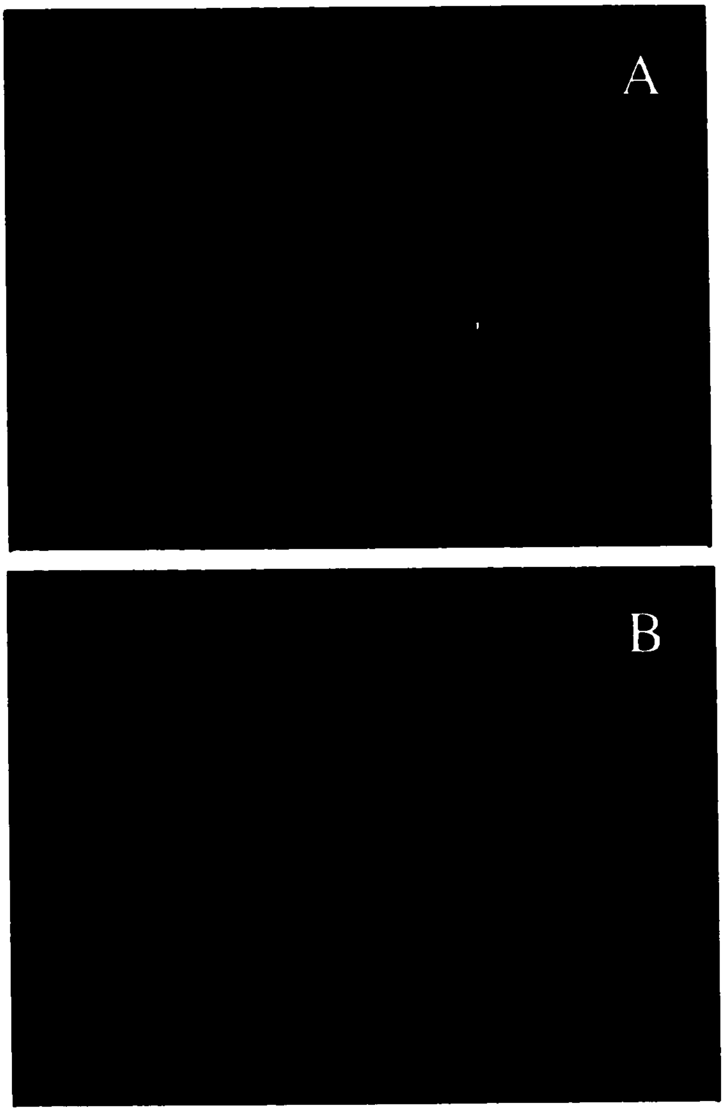

Figure 5-1: Two frames obtained from a digital video camera directed along the axis of the reactor at a temperature of 1185 K and a pressure of 40 kPa. A: Ethane (52 sccm) flowing in the top and Ar (52 sccm) in the bottom. B: Ethane and Ar flows both reduced to 6 sccm.

shown in Chapters 3 and 4 that there was a maximum rate of carbon deposition and a maximum yield of liquid products. An orange glow appeared in the centre of the reactor. This observation was consistent with the presence of an aerosol which was either hot and emitting light or reflecting and scattering light from the furnace or reactor walls out through the quartz window.

It was suspected that, if a condensed phase was present in the reactor, it should attenuate a light beam. To begin laser attenuation experiments, the signal was stabilised with 6 sccm of argon flowing into both the bottom and top entrances to the reactor. The flow in the top was then changed to 6 sccm of ethane. As shown in Figure 5-2, there were some oscillations in the photodiode signal initially as the flow stabilised, but then the signal intensity settled down at three-quarters of its initial value. Switching back to argon flow in the top returned the photodiode signal to its initial value.

The attenuation of the laser signal depended on the residence time of the gases in the reactor, as shown by the squares in Figure 5-3. At the shortest residence time of about 1 s, (52 sccm) the attenuation was only about 3 %. The attenuation reached a maximum of about 40 % when the residence time was 7 s and then declined slightly for longer residence times or slower flow rates. Overlapping squares at the same residence times show the results of experiments performed on different days to check reproducibility.

The dependence of the deposition rate of *pyc* on a solid surface, described in Chapter 3 (shown by the circles in Figure 5-3) on residence time paralleled the dependence of the laser attenuation on residence time, shown by the squares. Assuming, as a first approximation, that the attenuation of light was proportional to the amount of material in the gas phase, a number of possibilities exist. This close parallel was consistent with the

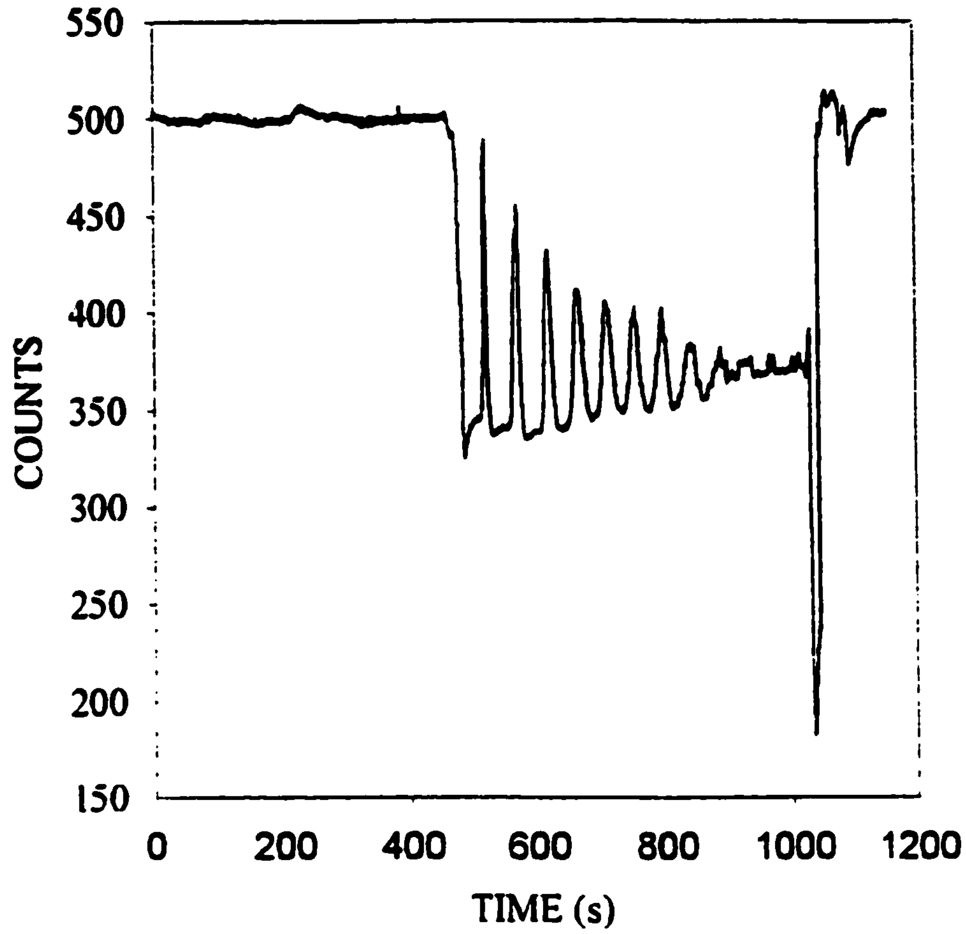

Figure 5-2: Attenuation of the transmitted laser intensity for a flow rate of 6 sccm of ethane in the top of the reactor and an equal flow rate of argon in the bottom at a reactor pressure of 40 kPa and a reactor temperature of 1185 K.

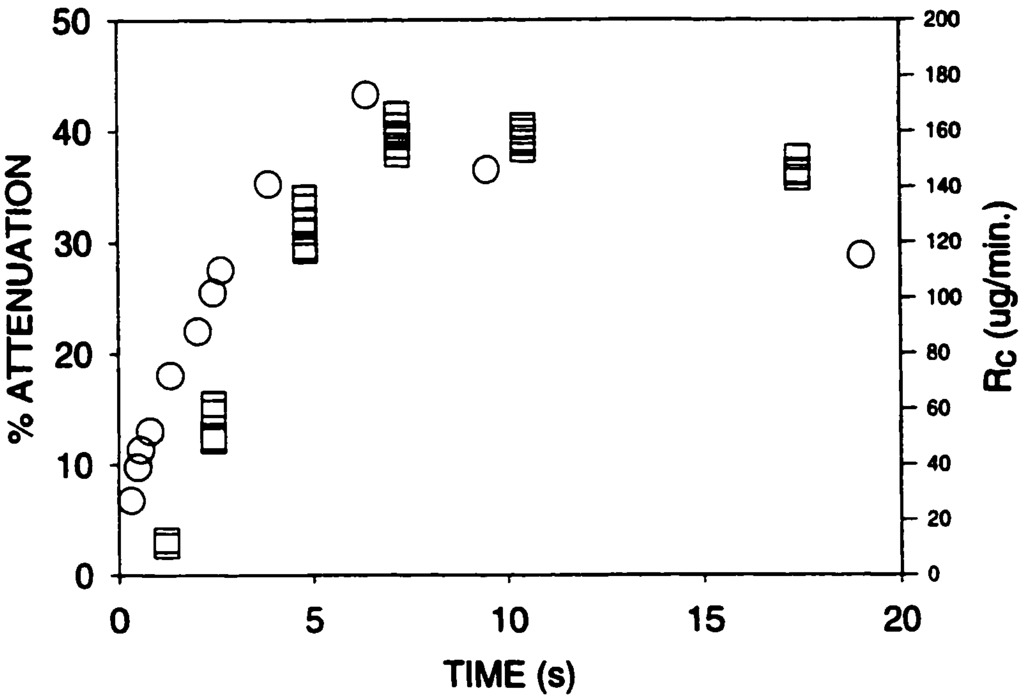

Figure 5-3: Attenuation of the laser beam (squares) and rate of carbon deposition (circles), as a function of the residence time of gases at 40 kPa in the reactor (at 1184 K).

hypothesis that the species responsible for attenuating the light beam also formed carbon in a direct, first-order process. It is also possible that the *pyc* was formed from another intermediate, such as a collection of large PAHs which also reached a maximum at the same time. Actually, the attenuation of light is a complex function of a number of parameters including particle diameter, which is related to the mass through the density, and the optical properties of the species. This relationship will be examined in more detail in Chapter 6.

5.2 Analysis of the Samples Collected in the Hot Zone

In order to characterise the material responsible for this orange glow, quartz disks were warmed to 1185 K in argon in the upper part of the hot zone and dropped through hot ethane flowing up from the bottom. SEM images of such a disk are shown in Figure 5-4. These images revealed the presence of tiny circles on the surface of the disk. The circles ranged in diameter from 10 to 250 nm. A consideration of different regions of the substrate indicated the material was not evenly distributed over the entire surface of the substrate. As shown in Figure 5-4 a high number of species were observed in the center of the substrate and the number decreased toward the outer edge. Examination of the side of the substrate indicated fewer species.

In order to establish the validity of the technique additional sets of experiments were performed. A substrate was held at 400 K in the region just above the top of the furnace and was dropped through the hot zone of the reactor under the same flow conditions as for the first substrate. An SEM image of such a disk is shown in Figure 5-5. This image revealed the presence of much larger spheres (from 400 to 1000 nm), closely spaced on the surface of the disk.

Figure 5-4: Scanning electron microscope images of a hot quartz disc (1185 K) which has been dropped through the hot zone of the reactor when 6 sccm of ethane flowed in the bottom and an equal amount of Ar flowed in the top at a reactor temperature of 1185 K and a pressure of 40 kPa. The arrows indicate the region of the disk where each image was taken. The line in the bottom right hand corner of each image represents a distance of approximately 2 microns.

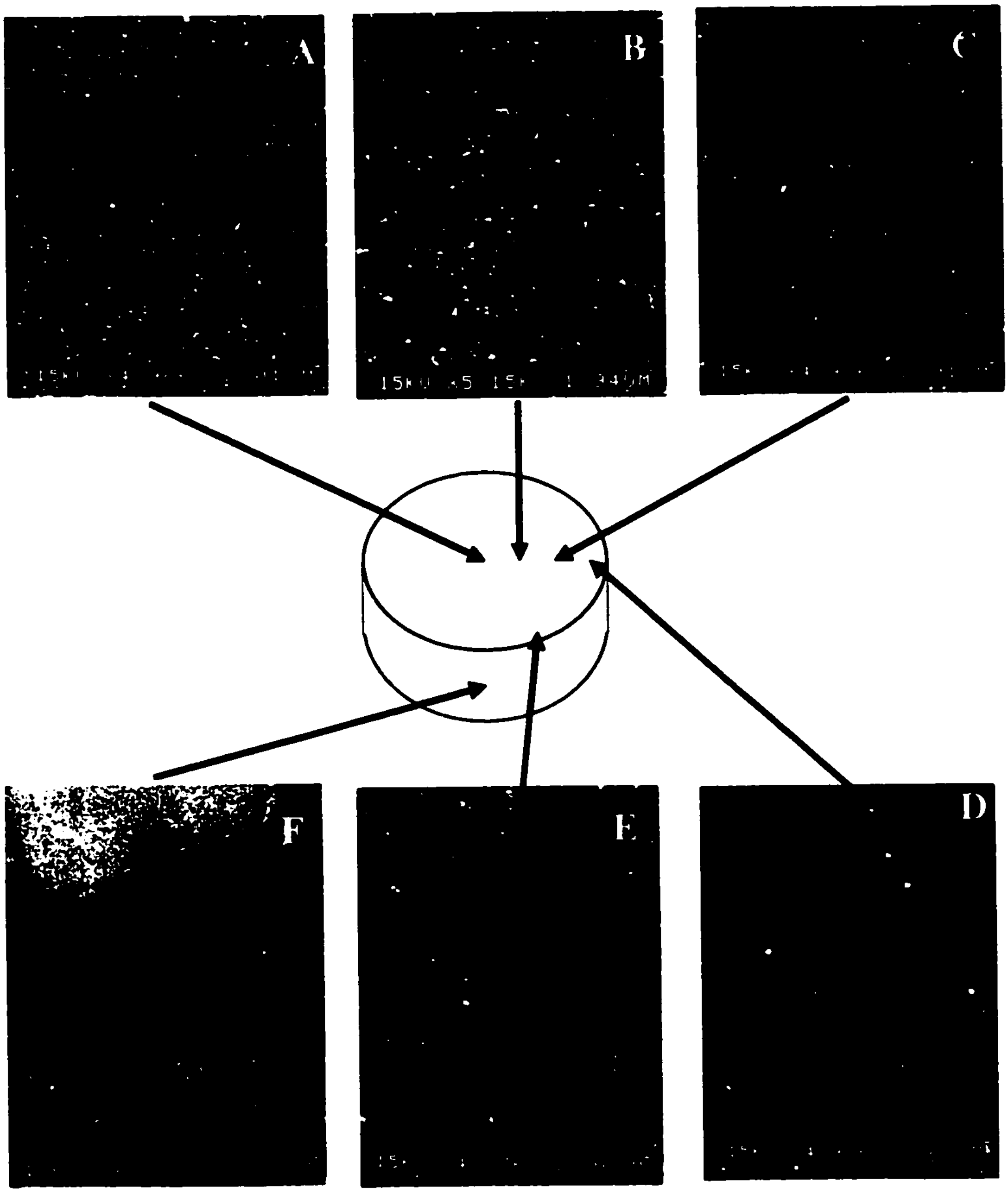
A
B
C
15KU X5 15K 1 340UM
F
E
D

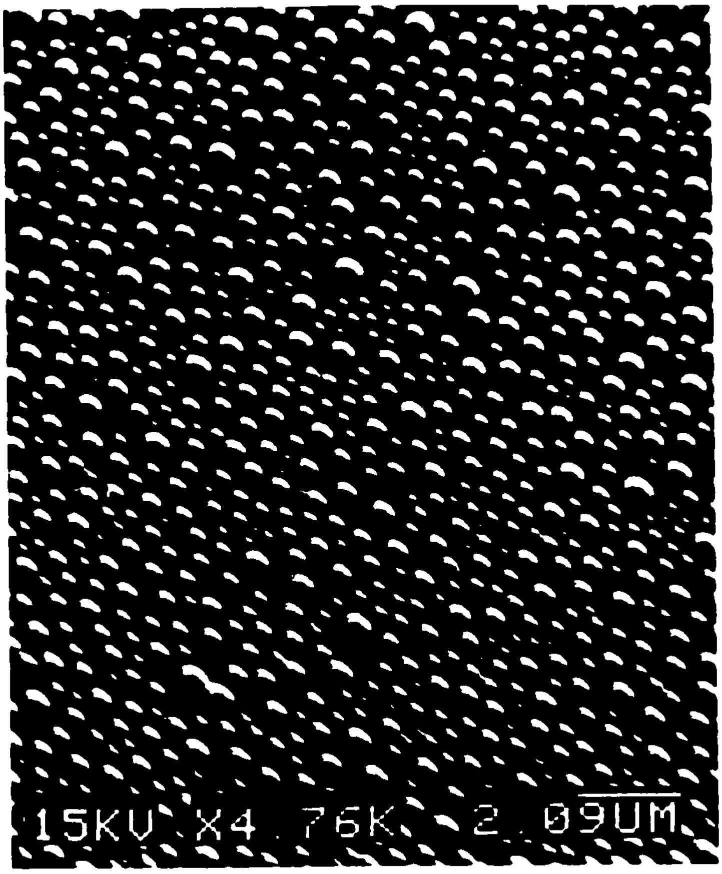

Figure 5-5: Scanning electron microscope image of a cool quartz disc (400 K) which has been dropped through the hot zone of the reactor when 6 sccm of ethane flowed in the bottom and an equal amount of Ar flowed in the top at a reactor temperature of 1185 K and a pressure of 40 kPa. The line in the bottom right hand corner of each image represents a distance of approximately 2 microns and the magnification is 6900x.

To obtain a blank, a disk was dropped from the hot zone through argon, which flowed into the top and bottom of the reactor. When such a disk was examined by SEM, only imperfections in the quartz and a number of "dirt" particles were observed on the SEM image in Figure 5-6A.

Figure 5-6B shows an SEM image of a substrate which had been dropped through ethane flowing at 6 sccm, removed from the system and washed with methylene chloride. Most of the material was removed from the substrate indicating the effectiveness of methylene chloride as a solvent.

A transmission electron microscope (TEM) analysis of material which was sampled from the hot zone reinforced the results obtained by SEM analysis. For the TEM analysis grids were heated and dropped through the aerosol in the reactor in the manner described in Chapter 2. Figures 5-7 A and B show TEM images of the edge of one bar from a grid which was dropped through the hot zone. The images shown in Figure 5-7 were typical of those which were observed in most regions of the grid. Here several semi-circular objects appeared on the horizon of the grid wire, which was silhouetted against the white background. Comparison to the blank grid, which was dropped through argon, in Figure 5-8 indicated these species were not present. They were a product of the hydrocarbon system. These species measured at the widest point were between 5 and 260 nm in diameter. The size of the species observed by TEM was similar to those observed by SEM, providing further conformation of the SEM results.

The cross-sectional view and increased magnification provided additional information. In Figure 5-7 B a section of the bar has been magnified to a point where 1mm was equal to 5 nm. In this region two species with diameters of 24 and 260 nm were

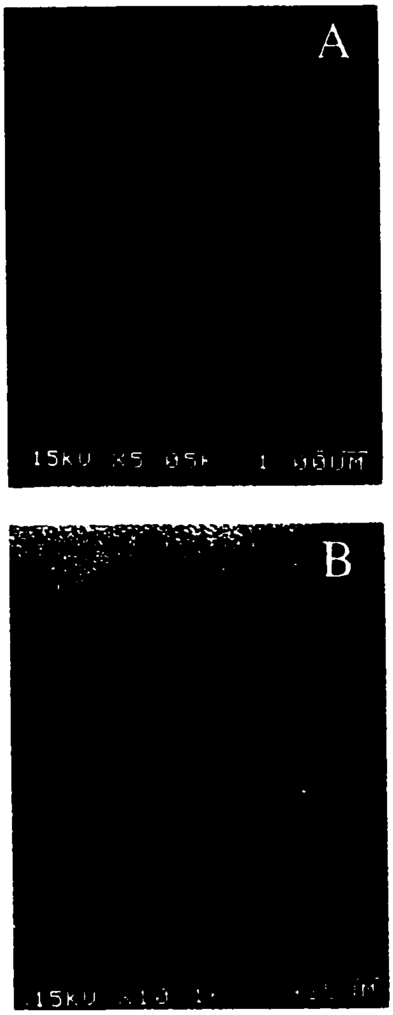

Figure 5-6: Scanning electron microscope images of, A, a blank quartz disc (1185 K) which was dropped through the hot zone of the reactor when 6 sccm of Ar flowed in the bottom and an equal amount of Ar flowed in the top and, B, a quartz disc (1185 K) which was dropped through the hot zone of the reactor when 6 sccm of ethane flowed in the bottom and an equal amount of Ar flowed in the top. In B the disk was washed with dcm before obtaining the image. The line in the bottom right hand corner of each image represents a distance of approximately 1 microns and the magnification is 7800x.

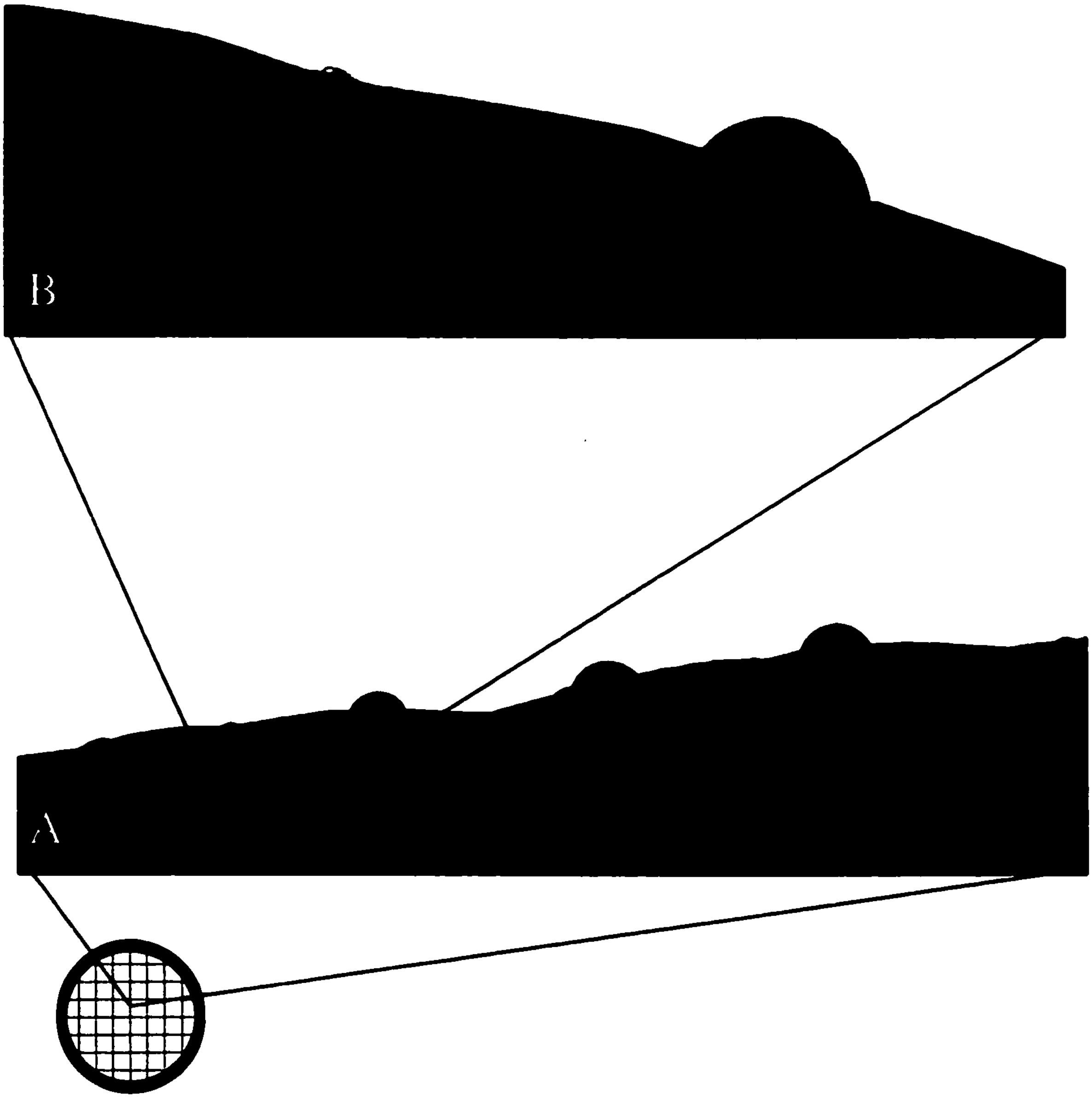

Figure 5-7: TEM images of the edge of a wire from a grid which was dropped through the hot zone of the reactor. Six sccm of ethane flowed in the bottom and an equal amount of Ar flowed in the top. In A the magnification is 40000 times and in B one region is expanded to 142000 times.

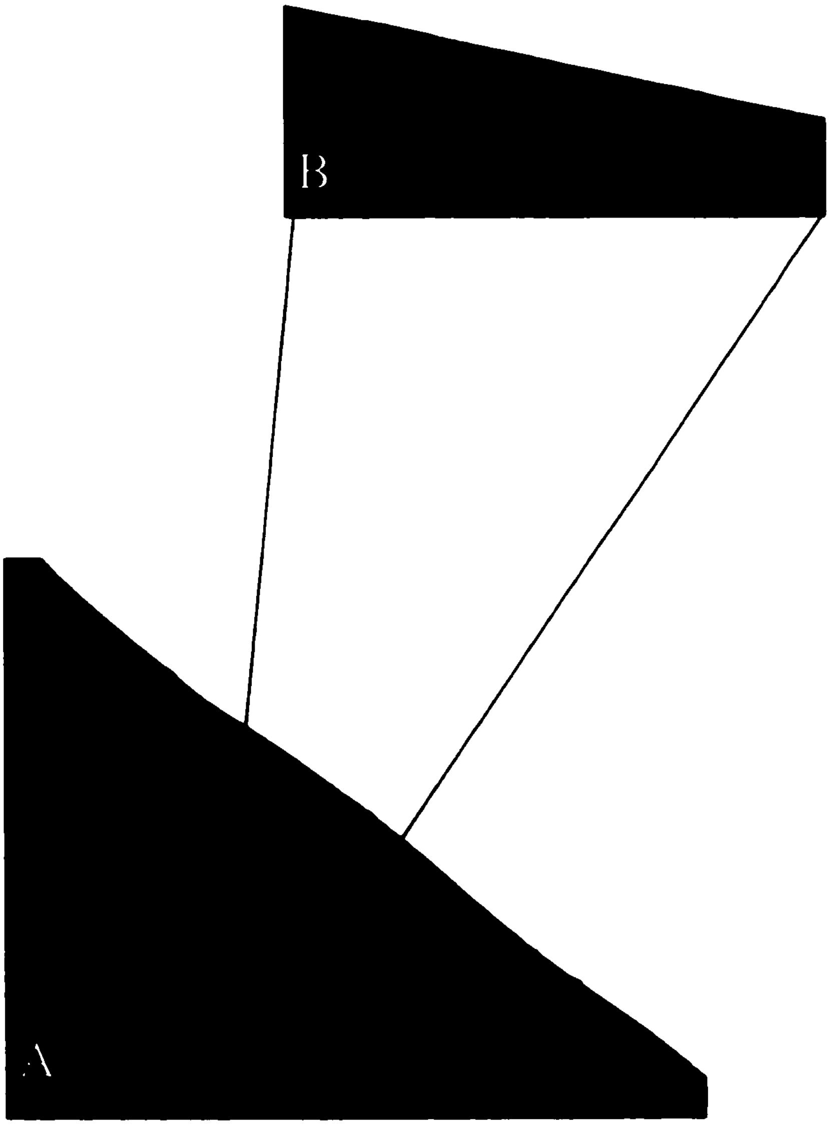

Figure 5-8: TEM images of the edge of a wire from a blank grid which was dropped through the hot zone of the reactor. 6 sccm of argon flowed in the bottom and an equal amount of Ar flowed in the top. In A the magnification was 40000 times and in B one region was expanded to 80000 times.

observed. The featureless surface between the two species was representative of most regions examined. Species significantly smaller than those observed by SEM were not observed by TEM providing further conformation of the SEM results.

The semicircular shape of the aerosol may have been partially caused by the circular shape of the grid wire obscuring the lower portion of the object. However, during observation of hundreds of protrusions from the bar, only one spherical species (Figure 5-9 A) in full view was observed. The absence of spherical species in full view is consistent with an aerosol population which partially flattened upon impact. Flattening implies a certain amount of fluidity in the material and indicates the diameter of flattened species on the substrate surface would be greater than spherical species of equivalent volume.

More uncommon was the particle observed and blown up in Figure 5.9 A which kept its spherical shape upon impact with the bar. Also less common were species such as those observed in Figure 5.9 B where the size of the spherical units was smaller and a number of species were present in a chain. These chains were similar to the soot or carbon black which has been more commonly observed (36).

Comparison of the lone sphere and one of the hemi-spherical species at higher magnification (220000X) is provided in Figure 5-10. The sphere, with a diameter of about 180 nm is dense with a featureless interior at this magnification, whereas the hemi-sphere (220 nm) contains circular dark regions which may indicate smaller spherical units of less than 4 nm in diameter.

The high surface area substrates were also suspended either inside the hot zone or just above it and dropped through the hot gases. Fluorescence spectra of the solution obtained after the high surface area substrates had been washed in methylene chloride are

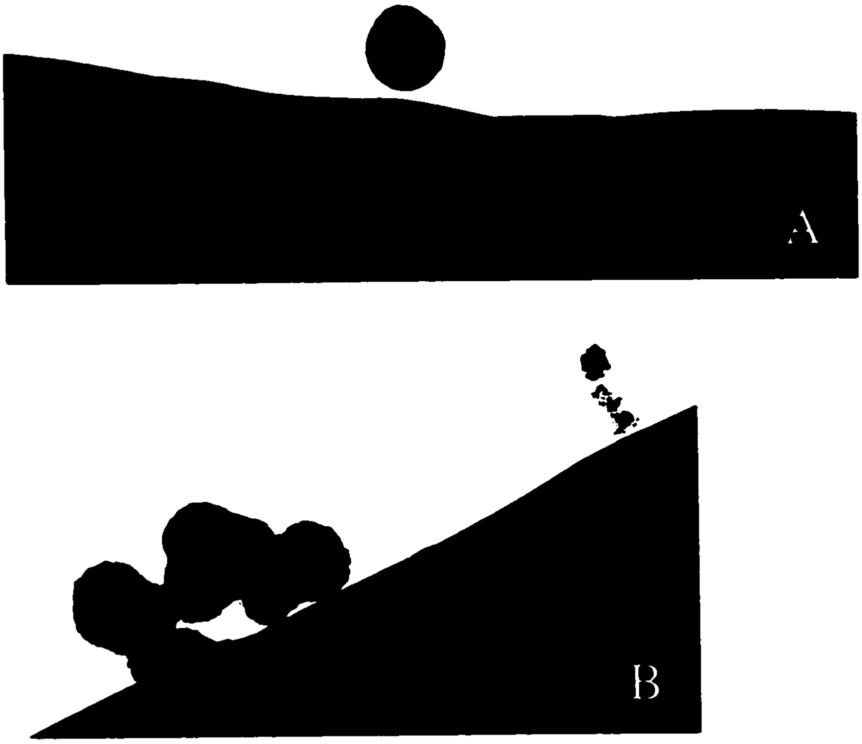

Figure 5-9: Atypical TEM images of the edge of wires from a grid which was dropped through the hot zone of the reactor when 6 sccm of ethane flowed in the bottom and an equal amount of Ar flowed in from the top. The magnification was 60000 times.

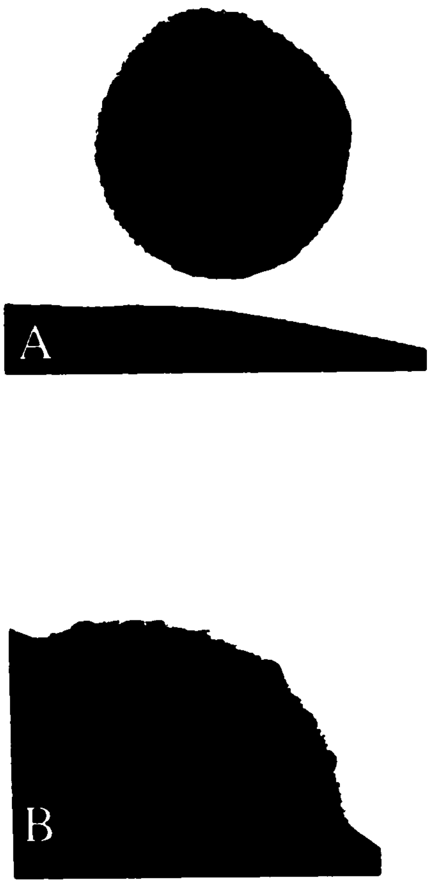

Figure 5-10 TEM images of the edge of wires from a grid which was dropped through the hot zone of the reactor when 6 sccm of ethane flowed in the bottom and an equal amount of argon flowed in the top. The magnification is 220000 times.

shown in Figure 5-11. The material collected on the preheated substrate (1185 K) fluoresced in the region from 300 to 600 nm, with maxima at 380, 415 and 440 nm. The material collected on the cooler substrate (400 K) also fluoresced in this region but the maximum occurred at 480 nm. The blank obtained with only argon flowing into the reactor did not fluoresce in the regions examined.

The mass spectrum of the material collected on the cooler substrate, which dropped from a point above the hot zone down through the hot ethane, is shown in Figure 5-12A. The largest peak had a mass to charge ratio of 350 amu. At higher masses, there were several peaks separated by either 24 or 26 mass units. Figure 5-12B shows that a similar MS analysis of the material collected on a hot substrate provided no discernible ion intensity.

When the reactor was removed from the furnace, it was observed that carbon had deposited on the parts of the reactor which had been in contact with hot ethane. The parts of the reactor which had always been blanketed by argon remained clear, indicating the argon counter flow was effective in preventing diffusion of carbon precursors.

5.3 Interpretation of the aerosol observation and analysis

The SEM analysis of the surface of the preheated disk indicated that tiny, spherical particles were suspended in the gas phase. These were unlike the solid soot particles observed elsewhere (3), which were generally chains of attached spherules, like strings of pearls. The SEM analysis of the surface of the cooler substrate revealed much larger particles. As was suggested previously with respect to cold probe sampling in flames (103),

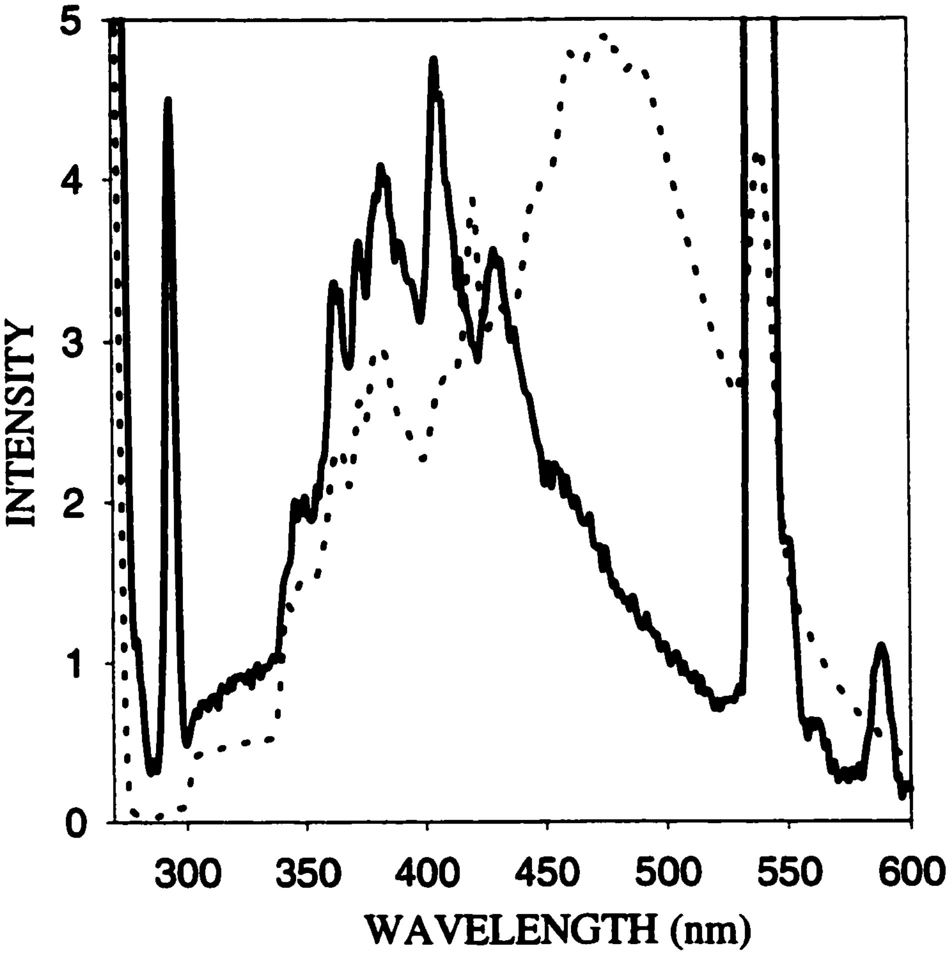

Figure 5-11 Fluorescence spectra, with 270 nm excitation, for material collected on a high surface area quartz substrate which was dropped through an aerosol formed with 6 sccm of ethane flowing in the bottom of the reactor and an equal amount of Ar flowing in the top. Solid line: hot (1185 K) quartz substrate. Dotted line: cold (400 K) quartz substrate (The sample was diluted to provide a fluorescence intensity similar to that of the cold substrate). The sharp peaks at 540 nm were due to scattered light.

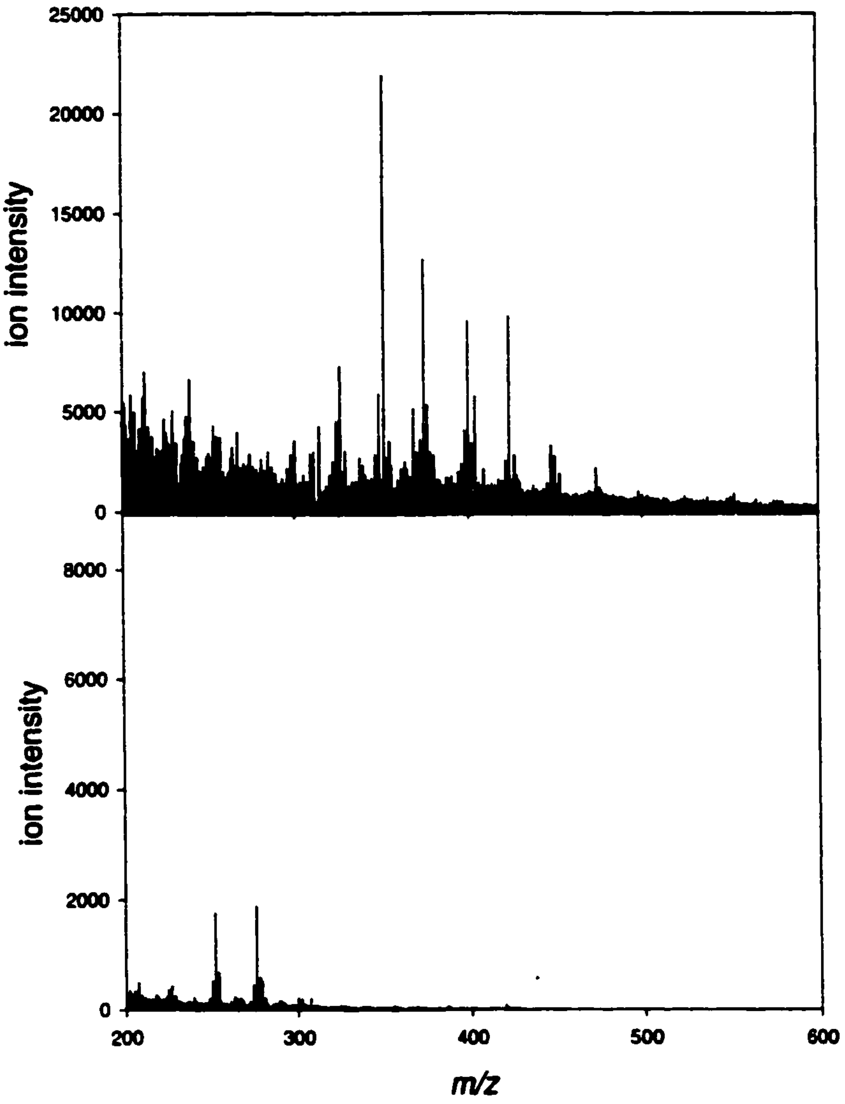

Figure 5-12: Mass spectra of material, collected as described in Figure 5-11, evaporated onto a platinum filament and flash desorbed into an EI source. A: Cool (400 K) quartz substrate. B: Hot substrate (1185 K)

material which was in the gas phase could have condensed when it was chilled by the passage of the cooler substrate. This would result in the formation of larger droplets.

The attenuation of the diode laser intensity could have been caused by absorption or scattering by the smaller droplets, as collected on the preheated disk. The observation of an orange glow could have been caused by scattering of light originating at the reactor walls or by direct, black-body emission of light by the gas-borne particles.

In Chapter 4 analysis of the condensed reactor effluent by liquid chromatography, gas chromatography and mass spectrometry revealed that the major constituent of this liquid was benzene. The rest of the mixture consisted of PAHs, whose concentration gradually declined with increasing mass, up to a mass of 700 amu. It seems possible that the large droplets formed on the cooler substrate resulted from the condensation of these large PAHs from the gas phase.

Samples collected on the high surface area substrates showed fluorescence in spectral regions where emission is expected from large PAHs (123). For example, naphtho(8,1,2abc)coronene, a nine-ring PAH with formula, $C_{30}H_{14}$, fluoresces at 460, 480 and 490 nm (124), similar to the maximum at 480 nm observed for the material collected on the cooler substrate. On the other hand, fullerenes (125) fluoresce in the region between 600 and 800 nm and linear polyenes ($C_{2n}H_{2n+2}$) (126) fluoresce weakly in the region between 500 and 700 nm. Evidently, fullerenes and polyenes are not responsible for the fluorescence maxima observed in this work.

However, the spectrum of material collected on the hot substrates in this work is different than that of condensed species extracted from flames with cooled probes (101).

The latter species showed fluorescence between 250 and 600 nm with maxima at about 320 nm and 375 nm which could correspond to a predominance of 1 or 2 ring aromatics. The cold probes used in the flames may have caused the condensation of smaller PAHs, as has been shown to occur in our system with cold substrates, and was previously suggested by Homann (103). In our work, with hot substrates, there was little fluorescence in the region from 300 to 350 nm and emission was strongest in the region between 350 and 500 nm. A number of aromatics fluoresce in this region including: anthracene, bianthranyl, 9,10-dinaphthyl anthracene, phenanthrene, 3,4-benzophenanthrene, chrysene, pyrene, tetraphenyl pyrene, bipyrenyl, fluoranthene, perylene, and benzo(ghi)perylene.

Larger PAHs tend to fluoresce at longer wavelengths. The methylene chloride soluble portion of the aerosol collected on the preheated substrate had a fluorescence maximum at a shorter wavelength than the species condensing on the cooler substrate. The observation of fluorescence at shorter wavelengths is consistent with an aerosol composition which incorporates smaller aromatic units into the structure. These results are consistent with a precursor material, similar to one suggested previously (100), which consists of a number of smaller aromatic units connected by alkyl or alkenyl links.

MS analysis of material condensed onto a cold substrate were consistent with the results of the reactor effluent analysis presented in Chapter 4 where it was shown that the high molecular weight material exiting the reactor consisted of large PAHs. Samples collected in other laboratories (101, 102) with water-cooled probes were different than those collected here on the cold probes. The largest peaks were at 226, 252 and 276 amu (102), much lighter than those observed in the present work. Sarofin (127) has pointed out that it is unlikely these lighter species would condense at high temperature.

A number of attempts were made to obtain the mass spectrum of the material collected on hot substrates. In Figure 5B the spectrum for a sample prepared from a hot substrate shows the only observable ion intensity can be attributed to the solvent, methylene chloride. There could be a number of reasons why the material could not be observed by the hot wire technique. It is possible that the probe wire was not hot enough to flash desorb the material into the gas phase. It is also possible that this material was sufficiently carbonised in the pyrolysis process that analysis by mass spectrometry was not possible or that there was simply not enough material to be observed by this technique.

6.0 Aerosol Statistics and Dynamics

In Chapter 5 the presence of an aerosol in the hot zone of the pyrolysis system was established. The presence of aerosol species does not necessarily indicate that they are precursors to surface carbon. The following chapter provides an estimation of the numbers of these species in the system and examines the plausibility of these species as carbon precursors.

6.1 Particle Size Analysis

As discussed in Section 5.2, the aerosol was sampled on the surface of a quartz disk that dropped through hot ethane. Each SEM image of each portion of the disk examined in Figure 5-5 was scanned into a digital format and eight sections (4 μm^2) of each of the photos were expanded to a point where one pixel represented 5 nm. For the side view of the disk, twenty-four sections (4 μm^2) of the photos were expanded to a point where one pixel represented 5 nm. A typical section (4 μm^2) of a photo is provided in Figure 6-1A. The contrast was then manually adjusted as indicated in Figure 6-1B to provide a clear distinction between the particle and the background. Scion image analysis software (128) was then used to set the threshold and count and measure the area of each individual particle. If manual contrast adjustment was not performed, the images could not be analyzed due to problems in setting the threshold. Figure 6-1C shows the result of setting the threshold for the measurements, where distinct cutoffs from black to white were set for the analysis. From the area, calculated by the software, the radius, r_d, of each particle was calculated from Equation 6-1.

Figure 6-1: A 4 um^2 section cropped from the SEM image of the central region of the substrate surface shown in Figure 5-4A. In A the image has been blown up. In B the contrast has been manually adjusted and in C the threshold algorithm in the Scion Image software (128) was used to set up distinct boundaries for counting.

$$r_d = (A_d / \pi)^{1/2} \quad 6\text{-}1$$

Here A_d is the area provided by the image analysis. From the simplifying assumption that the deposited species could be represented geometrically by one half of a sphere the radius of the corresponding gas-phase species was calculated from Equation 6-2.

$$r_g = (\tfrac{1}{2})^{1/3} r_d \quad 6\text{-}2$$

In this manner particles with gas-phase radii as small as 15 nm could be observed and counted. Some particles as small as 10 nm were also observed by eye, but due to limitations in the technique, numbers of particles smaller than 15 nm could not be reliably determined for particle size analysis. The total number of species counted from the SEM images in Figures 5-4 A through F are tabulated in Table 6-1. For each section the sample mean (the arithmetic average), median (the diameter for which one-half the particles are smaller and one-half are larger) and the mode (the most frequent size) are also presented in Table 6-1.

The analysis presented here can be compared to the previous MS analysis by comparing the diameter of the smallest species observed by SEM, 10 nm, to that of the largest observed by MS. The symmetrical PAH closest to 600 amu would contain 54 carbon atoms with a central ring surrounded by two rings out in any radial direction. This PAH would have a width of 1.3 nm and breadth of 1.4 nm. However, the SEM analysis could not reveal two-dimensional structure. We observed discrete hemi-spherical units

Table 6-1: The mean, median, and mode for the diameters (corrected to represent the diameter of species in the gas phase) of particles from the computer generated particle analysis for sections A-F of the substrate pictured in Figure 5-4.

Sample	Number of particles counted	mean (nm)	median (nm)	mode (nm)
A	494[a]	52	42.5	32.5
B	342[a]	60	67.5	22.5
C	78[a]	64	52.5	37.5
D + E	81[b]	46	37.5	27.5
F	276[c]	22.5	27.5	22.5
Total	1250	62.5	37.5	27.5

[a] Calculated from eight 4 μm^2 sections of regions A, B or C pictured in Figure 5-4.

[b] Calculated from sixteen 4 μm^2 sections of regions D and E pictured in Figure 5-4.

[c] Calculated from twenty-four 4 μm^2 sections of region F pictured in Figure 5-4.

which represented a three-dimensional agglomeration of hydrocarbon units. The gap between the two analysis was narrowed by TEM analysis, where structure down to 4 nm was observed. Without doubt there still remain small particles which were too large to observe by MS and too small to observe by TEM. This gap is perhaps better thought of in terms of mass where a spherical particle with a diameter of 4 nm and a density of 1.3 g/ml would have a mass of 4×10^{-23} kg, whereas the largest species observed by MS were about 700 amu or 1.16×10^{-24} kg. So the gap is a factor of 35 in mass or 3 in diameter.

Interception occurs when a particle follows a gas streamline that comes within one particle radius of the surface. Inertial impaction occurs when a particle, because of its inertia, crosses streamlines near the surface and hits the surface. Diffusion involves a particle whose Brownian motion is sufficiently great that it strays from the streamlines and hits the surface. Since a wide range of sizes and therefore speeds of particles were observed, it was expected (10) that interception, inertial impaction and diffusion all would have played a role in depositing material on the dropped substrates. It was expected that the majority of large heavy particles would have contacted the surface by impaction and the smaller light particles, by diffusion. Since these mechanisms are dependent on particle size, it is possible the size distribution established from sampled material may have been skewed due to differing collection efficiencies.

The approximate collection efficiencies can be estimated by making a number of assumptions as indicated in Reference 10. However, since the calculation of the theoretical efficiency curve requires numerical analysis and a large number of simplifying assumptions, and since the errors in the end result would have been difficult to establish(10), we took an empirical approach to the problem. Examination of different regions of the substrate indicated there were differences in sampling efficiency. From Table 6-1 we saw several trends in the collection of gas-phase species. A number of larger species were observed on the interior face of the substrate and the number and size of species decreased at the outer edge and on the side of the substrate.

Impaction would only occur on the face of the substrate. It is expected that small species would diffuse to any surface of the substrate, including the edge. Therefore, the observation of smaller species on the edge (region F in Table 6-1) of the substrate is not unexpected. Figure 6-2 shows the total distribution taken from all regions of the substrate and compares that to the distribution of sizes of species found on the side of the substrate. These two distributions should represent two extremes; the actual distribution in the gas phase should lie somewhere in between.

6.2 System Dynamics

In order to validate the sampling technique the dynamics of each component in the system needed to be estimated. The velocity of the substrate as it fell past the exit T was calculated to be 1.6 m/s and this should have increased to 2.3 m/s at the bottom of the reactor exit. The linear flow rate without volume expansion would have been approximately 0.01 m/s for a flow rate of 6 sccm. The root mean square speeds, C_{rms},

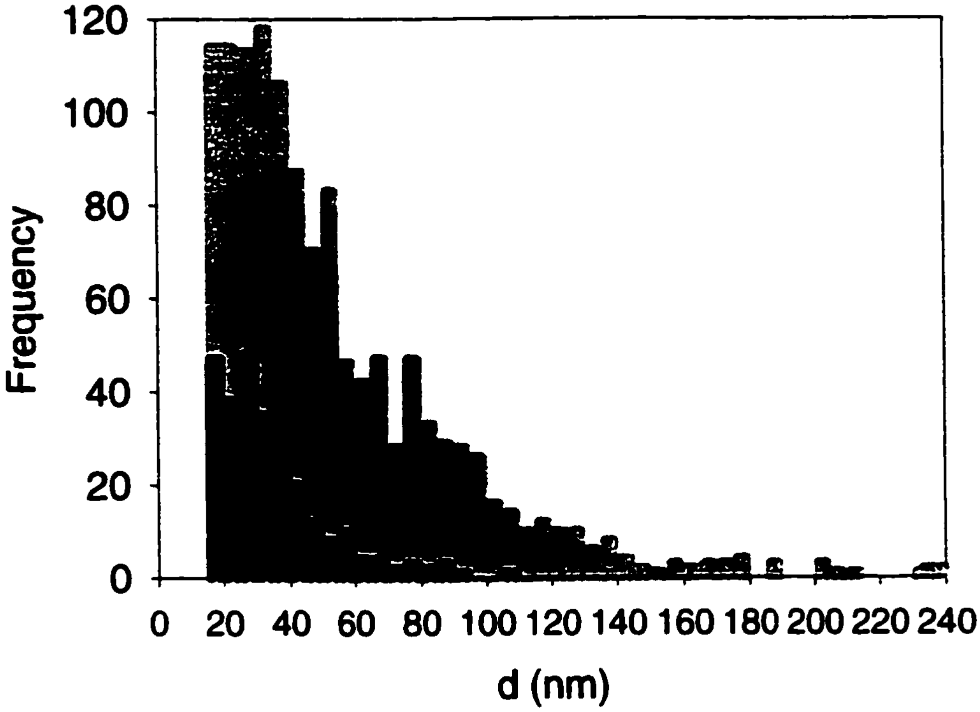

Figure 6-2: The size distribution of particles on the substrate based on measurements from the SEM analysis described in Section 6.1. The gray bars represent all of the data collected. The mechanism of collection would have included impaction and diffusion. The black bars represent the distribution for the side of the substrate. The mechanism of collection should only have included diffusion.

$$C_{rms} = ((\,18\,k_B\,T\,)\,/\,(\,\pi^2\,\rho\,d^3\,))^{1/2} \qquad 6\text{-}3$$

which were calculated from equation 6-3, and the particle masses as a function of particle diameter are provided in Figure 6-3. The actual density of the material was unknown. A value of 1.3 g/ml, the density of coronene, a large PAH, was used as an estimate. The actual density could have been different but the relative distribution would have remained the same, simply changing by the ratio of the actual density to that of coronene. The plot indicates that the small particles were very light and moved much quicker than the substrate. Since the mass of a sphere is a function of the radius cubed, the mass increased rapidly with particle size. The root mean square speed of the particles was a function of the square root of the inverse mass and decreased rapidly with particle size. The analysis indicated species less than 40 nm in diameter moved more quickly than the speed of the substrate at the central exit and those greater than 40 nm were moving more slowly than the substrate. This indicates that large, slow, moving species would have been preferentially captured on the face of the falling substrate by impaction. Small, fast-moving species would have been captured on the face and side by diffusion. This agrees with the observed distributions on the face and side of the dropped substrate.

The problem of the diffusion of species from laminar flow through a tube, to the surface of that tube, was considered for large aromatics in Chapter 3. The same equations, with modifications for annular flow (121), should apply to the aerosol considered in this section and are provided in Equations 6-4 and 6-5.

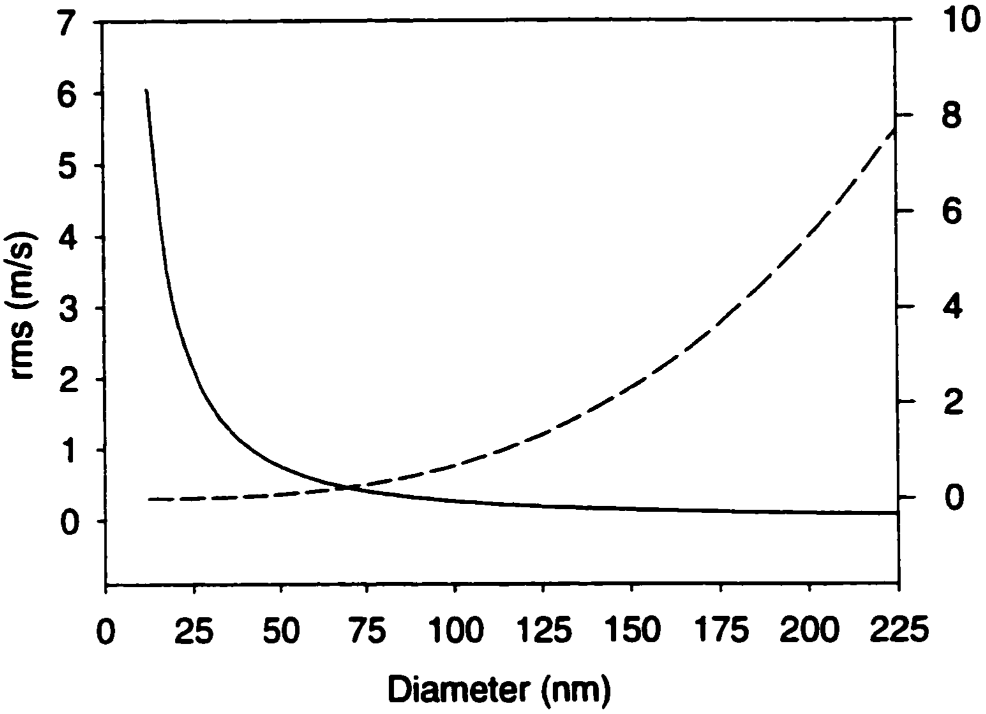

Figure 6-3: The root mean square speed (solid line, left axis) and the mass (broken line, left axis) as a function of particle size.

$$R_{DAi} = k_{DAi} C_i M_i \tag{6-4}$$

$$k_{DAi} = D_i / (22 R (1-a^2)/2a) \tag{6-5}$$

Here, R_{DAi} is rate of mass transport to the dropped substrate and k_{DAi} is the rate constant for diffusion to the inner surface of an annular reactor from reference 121 and a is the ratio of the inner radius to that of the reactor radius, R. The calculation of mass transport to the reactor surface requires the diffusion coefficient, D_i, which was calculated from the Stokes-Einstein equation (6-6).

$$D_i = (k_b \, T \, C_{c\,i}) / (3 \pi \eta \, d_i) \tag{6-6}$$

In equation 6-6, k_b is the Boltzmann constant, η is the viscosity of the median, d_i is the diameter of the particle, and C_c is the slip correction factor and takes into account the fact that the relative velocity of the gas at the surface of the spherical particle cannot be assumed to be zero at very small particle sizes (< 1 um). From Reference 10 the value of C_c can be calculated from equation 6-7.

$$C_{ci} = 1 + (\lambda/d_i) (2.34 + 1.05e^{-0.39(di / \lambda)}) \tag{6-7}$$

In equation 6-7, λ is the mean free path of the gas. In this case it was assumed the system was made up of methane only.

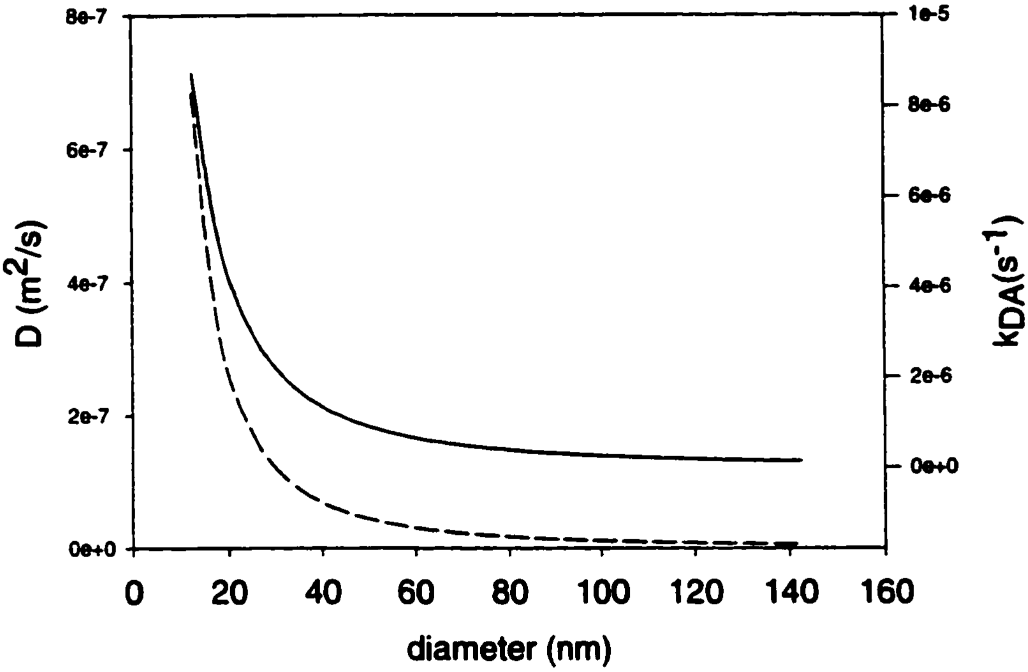

Figure 6-4: The diffusion coefficient, D, calculated from equation 6-6 (broken line, left axis) and the rate constant for mass transport of the aerosol to the reactor surface (solid line, right axis) as a function of particle size from Equation 6-5.

The diffusion coefficient is plotted as a function of the aerosol diameter in Figure 6-4. The plot indicates the diffusion coefficient decreased substantially with particle size. This was also reflected in the rate constant for mass transfer to the surface which decreased substantially with particle size.

6.3 Diffusion onto the Substrate

The material which was found on the side of the substrate was suspected to have diffused there with minimal impaction. By assuming only diffusion took place, the side distribution can be used to calculate the average rate at which material deposited onto the side of the substrate as indicated in equation 6-8.

$$R_{di} = [(F_i) / (A_d \ t_f)] \qquad 6\text{-}8$$

Here F is the number of particles found in a certain size range, i, A_d is the area of the substrate examined and t_f is the time it took the substrate to fall through the reaction region. Figure 6-5 provides a plot of the particle deposition rate calculated from Equation 6-8 as a function of particle size. Here we see the distribution is skewed toward smaller particle size due to the fact that small species will diffuse to the surface faster than large ones as illustrated by the constants in Figure 6-4.

In order to consider the contribution of these species to the observed deposition rate the rate of mass transport to the surface must be examined. By multiplying V_i ρ (where V_i is the volume of the ith species and ρ is the assumed density of 1.3 g/ml) by the rate from equation 6-8, one can obtain the rate of mass transport to the reactor surface for

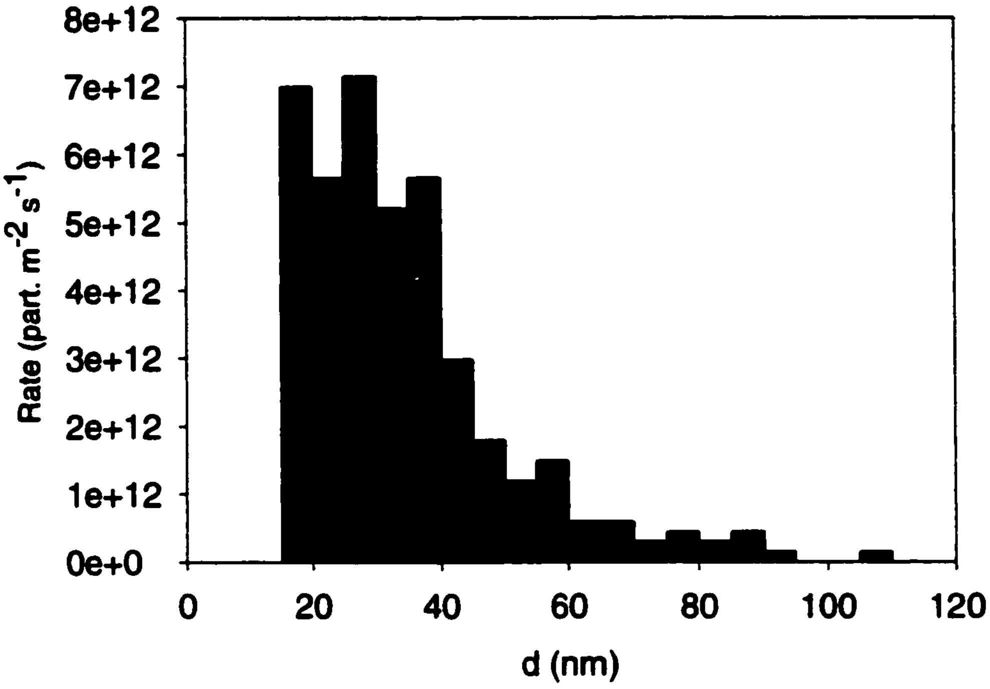

Figure 6-5 : The rate of particle transport to the substrate surface as a function of the particle diameter, calculated from the side distribution.

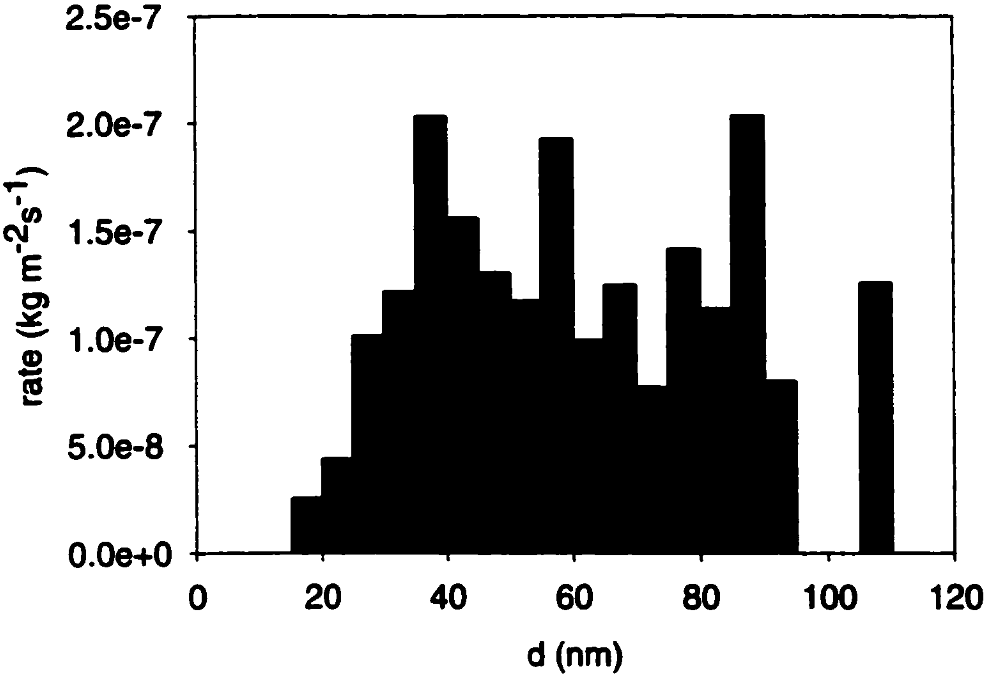

Figure 6-6: The rate of mass transport to the substrate surface as a function of the particle diameter calculated from the side distribution.

each size interval. The results are plotted in Figure 6-6. Here it is observed that the distribution is shifted to larger species due to the cubic dependence of mass on the radius as was indicated in Figure 6-3.

Overall the analysis indicates that, even though there were far more species found in the smaller size ranges, a small number of larger species had a substantial effect on the rate of mass transport to the surface.

By summing the rates for all diameter ranges, one can approximate the rate at which species diffused onto the substrate. In this case a value of 1.5×10^{-6} kg $m^{-2} s^{-1}$ was obtained. The rate of deposition onto the substrate suspended from the micro-balance was found to be 4.2×10^{-6} kg $m^{-2} s^{-1}$ at the same temperature, pressure and residence time. Therefore, this calculation indicates that the aerosol could account for 36 % of the observed deposition rate.

This analysis indicates that not only are aerosol species present in the gas phase but some proportion of them will deposit out, contributing to the surface deposition rate. However, the exact proportion is speculative since a number of factors could have introduced error into this calculation. There is some uncertainty in the calculation of the diffusion coefficient. Deposition mechanisms other than diffusion may have been involved. There is uncertainty in the calculation of the diameter of each particle. There may also be problems in the extreme regions of the distribution. Another possible problem is the sampling technique. The substrate suspended from the microbalance sampled a 5 cm section of the reactor whereas the dropped disk sampled a 20 cm section. Although some of the potential errors have been established, the combined errors involved in the calculation are difficult to establish. Therefore, although this analysis

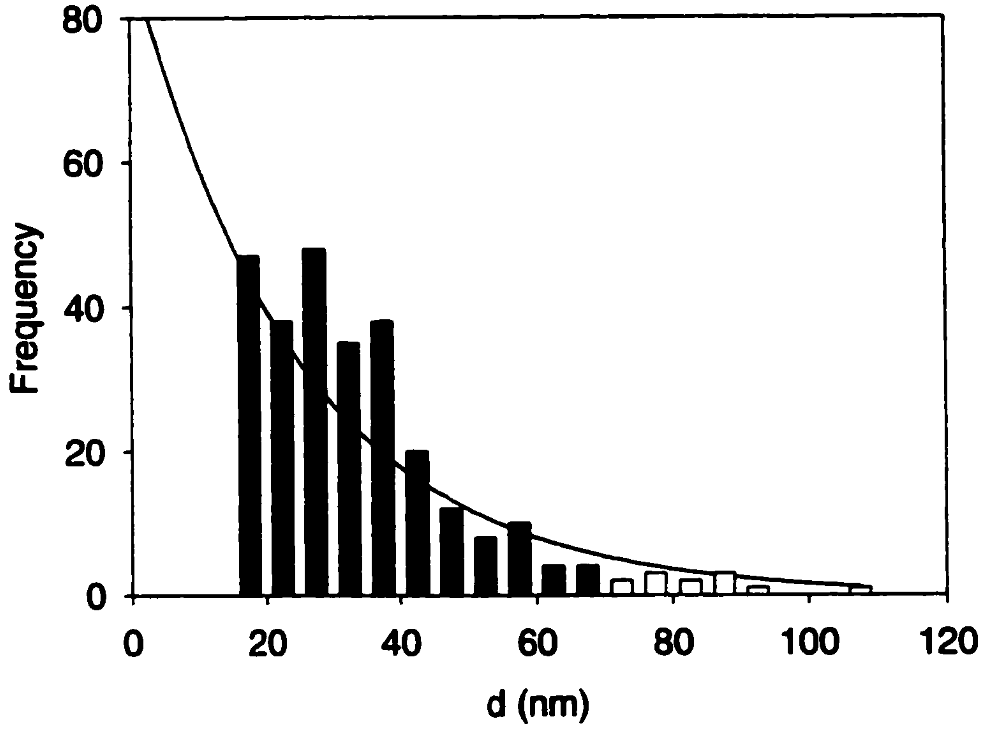

Figure 6-7: The size distribution of particles on the side of the substrate based on measurements from the SEM analysis described in Section 6.1. The line represents an exponential fit (Equation 6-9) which provides a maximum for the species in the size ranges below 15 nm. The white bars represent data based on less than 5 observations.

indicates that a fraction of the deposited material is due to the deposition of the aerosol, the actual proportion of material will need to be confirmed by alternative methods.

At very small diameters the species could not be observed by the SEM method. In order to establish the effect of small species, which were below the detection limits of this method, the frequency of these species was estimated. The original side distribution is plotted in Figure 6-7. Since the number of species smaller than 15 nm was not established, the data was fit to an exponential, Equation 6-9. In Equation 6-9, F is the

$$F = 88.469*\exp(-0.040*d) \qquad 6\text{-}9$$

number of particles for a 5 nm interval and d is the midpoint diameter for that interval. This fit is indicated by the solid line in Figure 6-7. It is not suggested that this data drops exponentially from zero but it is expected that an exponential fit should have provided a maximum. Taking into account the maximum number of smaller species, calculated from the exponential fit, has an insignificant effect (< 1 %) on the deposition rate.

At very large diameters it is suspected that a small number of observations could have biased the data. In Figure 6-7 intervals containing less than 5 observations are indicated by the white bars. If these species are excluded from the total rate calculation then the calculated rate is 9.0×10^{-7} kg m^{-2} s^{-1} which is 21 % of the deposition rate.

6.4 Diffusion Corrected Particle Size Distribution

Since the material on the side of the substrate is suspected to be deposited primarily by diffusion, then, by substituting R_D into equation 6-4, one can solve for the concentration and convert to number density for the gas phase. The resulting gas-phase distribution is provided in Figure 6-8. The mean diameter of the gas-phase population was 47.5 nm which indicates the distribution was shifted to larger species. Once again the species in the lowest mass ranges, which were estimated by the exponential fit, are shown to be insignificant. The higher mass species, in which few observations were made, are indicated by white bars. Summing all size ranges indicates the total concentration of all sizes of particles found in the gas phase was approximately 1.73×10^{19} particles m^{-3} .

6.5 Estimation of Number Density by Light Extinction.

The method used in section 6.3 provides the most direct route for the calculation of the rate of mass transport of particles to the reactor surface. This section provides another way to interpret these results which incorporates the laser extinction data from Chapter 5. Given the size distribution, estimated in Section 6.4, the light-extinction experiments in Section 5.1 can also be used to estimate the total number of particles in the reactor. Given this data one can then calculate the rate at which these species will diffuse to the reactor surfaces.

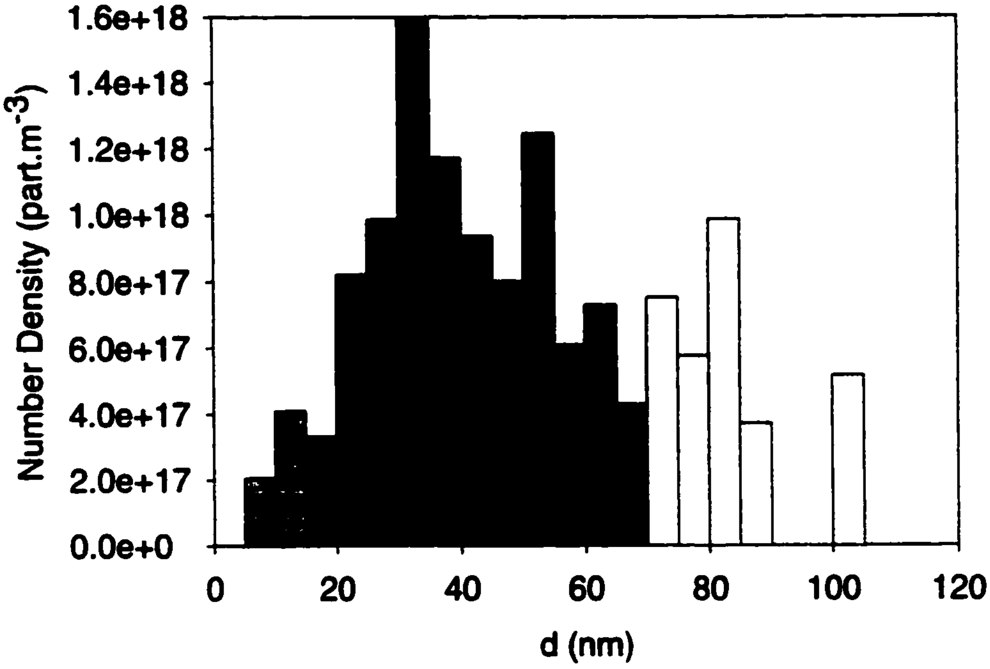

Figure 6-8: The number density of particles as a function of the particle diameter, calculated from the side distribution, where it was assumed only diffusional transport was important. The white bars represent data based on less than 5 observations. The gray bars represent values calculated from the exponential fit in Equation 6-9.

6.5.1 Extinction of Light by Small Particles

Interpretation of the laser attenuation experiments required knowledge of the absorption and scattering of light by small particles. A short summary of the necessary information will be introduced in this section. For further introduction the reader is referred to Reference 10, and to Reference 131 for a more rigorous treatment.

In order to interpret these results a number of assumptions needed to be made. It was assumed that all molecules in the gas phase did not absorb the laser light (670 nm). This was a reasonable assumption because the molecules in the gas phase have been characterized in Chapters 3 and 4 and the species observed are not expected to absorb in the visible. It was assumed that all aerosol particles were spherical. From the SEM and TEM results the spherical assumption appeared to be true for larger particles and there is no evidence to indicate the small particles, which could not be observed by these techniques, would be different. One must also assume the size distribution in Figure 6-8 is representative of that which was actually present. The discussion in Section 6-3 and 6-4 indicated the possible errors in the distribution.

It was also assumed that forward scattered light was not entering the detector. From Reference 10 forward scattering is not a problem if the angle from the exit to the detector outer diameter is less than 0.2 radians. In this case the angle was calculated to be about 0.19 radians. Finally the refractive index of the material must be known in order to calculate the extinction efficiency. Since the material is not well characterized, the refractive index is not known. However, reasonable estimations of the upper and lower limits will be established.

For a parallel beam of light, the ratio of the light intensity traversing the aerosol, I, to that incident on the aerosol, I_o, is given by the Beer-Lambert law in equation 6-10,

$$I / I_o = e^{-\sigma L} \qquad 6\text{-}10$$

where, σ is the extinction coefficient and L is the path length. From Reference 10 the extinction coefficient for a polydisperse aerosol is a sum of contributions from different particle sizes and is given by equation 6-11,

$$\sigma_i = \sum_i \pi N_i d_i^2 Q_{ei} / 4 \qquad 6\text{-}11$$

where σ_i , N_i, d_i and Q_{ei} are, respectively, the extinction coefficient, the number of particles per unit volume, the diameter of particles and the extinction efficiency of particle i. The extinction efficiency, Q_{ei}, is defined as the ratio of radiant power scattered and absorbed by a particle to the radiant power geometrically incident on the particle. Small particles are able to remove an amount of light from a beam which is greater than that simply blocked by the projected area. The equations describing the extinction efficiency are complex and intuitive interpretation is difficult. For particles whose diameters are of the same order of magnitude as the wavelength of the light, Mie theory can be used to describe the absorption and scattering of light. For these particles a program described in Reference 131 was modified (Appendix 2) and used to obtain the extinction efficiencies used in this work. As particle sizes decrease below 50 nm, into the Rayleigh region, the extinction efficiencies can be described by the limiting equation 6-6,

$$Q_{ei} = (8/3)(\pi d_i / \lambda)^4((m^2 - 1)/(m^2 + 2))^2 \qquad 6\text{-}12$$

where m is the refractive index and λ is the wavelength of light. Given the fourth order dependence on diameter the largest contribution should have been from the larger particles and neglect of aerosol particles under 15 nm should not have introduced significant error.

6.5.2 Aerosol Number Density

To further examine the role of the aerosol in this system, the number density of particles in the gas phase , was estimated from the observed light extinction.

Equations 6-10 and 6-11 can be combined and rearranged to give the number density as indicated in equation 6-13.

$$\sum_i N_i = -\ln(I/I_o)/(\sum_i (\pi x_i d_i^2 Q_{ei})/4)L \qquad 6\text{-}13$$

In equation 6-13 I/I_o can be taken from Chapter 5 and $x_i = N_i/(\sum_i N_i)$ can be obtained from Figure 6-8 as the fraction of the number of droplets in a particular size range.

The results presented in Chapter 5 were consistent with an aerosol composed of large aromatics which may or may not have been cross-linked. Therefore, using the refractive index for a small aromatic such as naphthalene provided one extreme and the refractive index for young soot provided the other extreme. A comparison of the extinction efficiencies, calculated by Mie theory, as a function of particle diameter, for these refractive indices, is provided in Figure 6-9. A large change in Q_e with m was observed. The extinction coefficient using the refractive index for naphthalene (130), given by the closed circles, was lower than for soot (129), given by the closed squares. It is likely that the soot precursors observed fell somewhere in between, with a reduced imaginary refractive index due to a cross-linked material which absorbed weakly compared to soot. Figure 6-9 also shows Q_e calculated using the refractive index for naphthalene, in the Rayleigh regime, from Equation 6-12 which is limited to describing small particles. Clearly there are vast differences between the two methods of calculation and these differences increased with particle size. Therefore, in the following discussion, only Mie theory is used in the calculation of Q_e.

Using the upper and lower limits on the refractive index, upper and lower limits on the number density were calculated from equation 6-13. The upper limit, using the naphthalene extinction efficiency, was 4.0 x 10^{17} particles per meter cubed and the lower limit, using the soot extinction efficiency, was 6.3 x 10^{15} particles per meter cubed. This result illustrates the strong dependence of the number density on the imaginary part of the refractive index. A smaller refractive index resulted in a smaller value of Q_e, which was inversely related to the number density, resulting in a larger number of particles. The

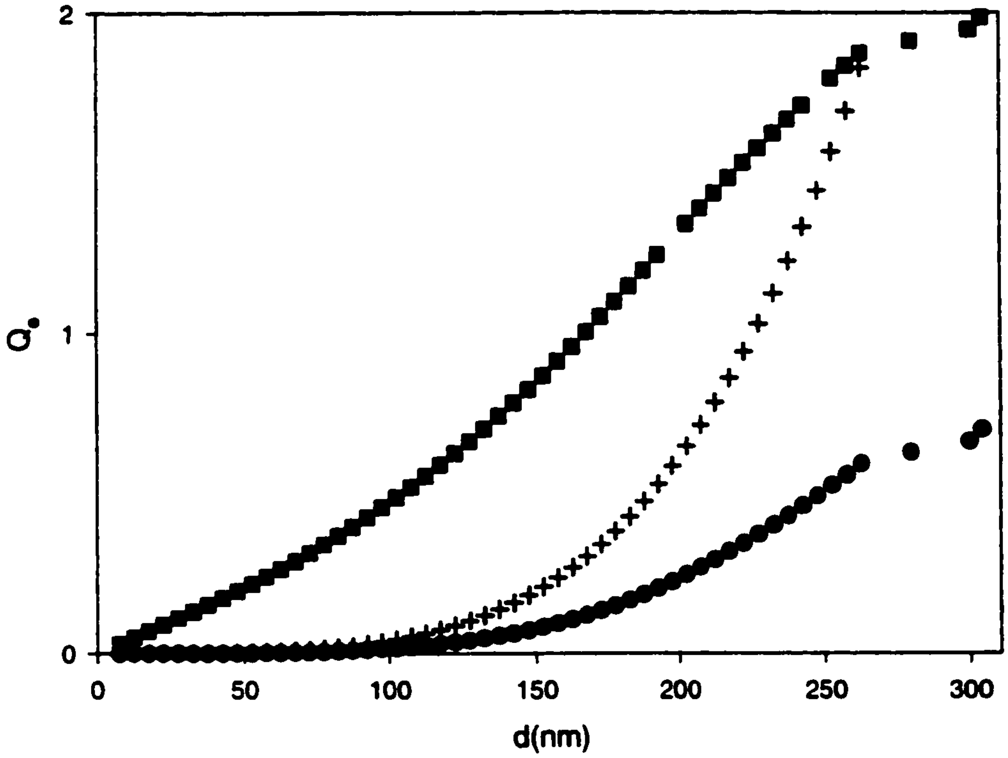

Figure 6-9 The extinction coefficient, Q_e, as a function of the particle diameter calculated from Mie theory. The closed squares and circles represent values calculated using the refractive index for soot (129), 1.62 + 0.47i and the refractive index for naphthalene (130), 1.59, respectively. The crosses are values calculated in the limiting Rayleigh region using equation 6-12 and the refractive index for naphthalene.

number density calculated using the refractive index of naphthalene was a factor of 40 below that calculated in section 6-4.

Again the uncertainties involved in the distribution discussed in section 6-4 will affect these results. In this analysis, as in section 6-4, the small particles, which were not measured, had an insignificant effect. However, uncertainties in large species were expected to have a large affect.

Equation 6-14 provides an attenuation factor, Af_i, which indicates the relative importance of each size range on the attenuation of light.

$$AF_i = (N_{Di}\, Q_{ei}\, \pi\, d_i^2) / 4 \qquad 6\text{-}14$$

Here N_{Di} is the number of species, in the ith size range, calculated in section 6.4. A plot of the attenuation factor as a function of diameter is provided in Figure 6-10. This data illustrates the strong dependence of the light extinction on the particle size showing the data based on few observations had a significant effect on the extinction properties of the system. Neglecting the species on which less than 5 observations were made (white bars in Figure 6-8) had a significant affect on the number density. The upper limit, using the naphthalene extinction efficiency, was now 2.9×10^{18} particles per meter cubed; which corresponds to 21 % of the particles calculated to be in the gas phase by the diffusion method.

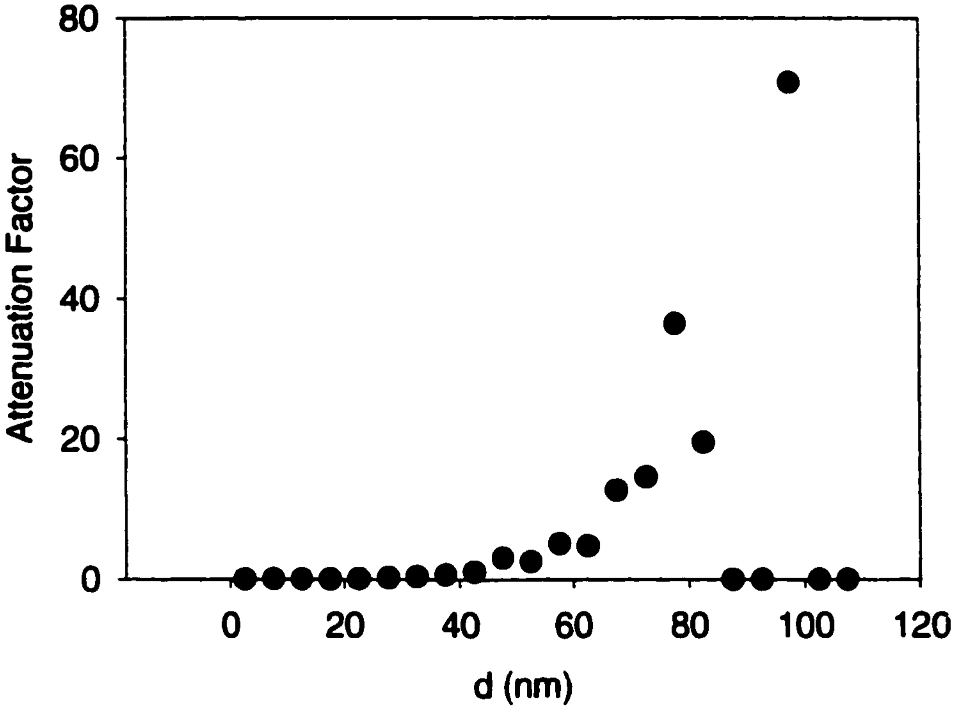

Figure 6-10: The attenuation factor as a function of diameter as calculated from equation 6-14.

6.6 Aerosol Coagulation

In sections 6.3 and 6.5 the rate of mass transport to the reactor surface was examined. For comparison it is interesting to compare this to the rate at which these aerosols contact one another. This process, where particles collide with one another in the gas phase, is called coagulation. The purpose here is not to consider the complex process of coagulation in detail but to consider a reasonable approximation for the average rate at which these particles will make contact with one another. Reference 10 provides a simplified discussion of the topic. This section summarizes some of that discussion and applies it to this work.

The simplest treatment of coagulation, Smoluchowski coagulation, involves a monodisperse population of spherical particles, where it is assumed that every collision results in sticking and the particle size changes slowly. The Smoluchowski approach considers that the particle flux at the surface of a particular particle is described by Fick's first law of diffusion. The rate of collisions can be described by equation 6-15.

$$(dN/dt) = K_0 \; N^2 \qquad \text{6-15}$$

Here K_0 is the coagulation coefficient described in equation 6-16.

$$K_0 = 8 \, \pi \, d_p \, D \qquad \text{6-16}$$

D is the diffusion coefficient of the particles and d_p is the particle diameter.

In this system the particle population size was shown to be polydisperse therefore the Smoluchowski approach is not valid. For the more complicated situation of a polydisperse aerosol there is no explicit solution for the coagulation rate. However if we approximate the continuous distribution with a discreet one and assume the distribution did not change, then the average coagulation coefficient, K_a, for a polydisperse aerosol is given by the double sum in equation 6-17,

$$K_a = \sum_{i=1}^{k} \sum_{j=1}^{k} K_{ij} f_i f_j \qquad 6\text{-}17$$

where,

$$K_{ij} = \pi(d_i D_i + d_i D_j + d_j D_i + d_j D_j) \qquad 6\text{-}18$$

and K_{ij} is the coagulation coefficient for species i contacting species j and f_i and f_j are the fractions of the total number of particles in the ith and jth intervals. Equation 6-12 provides the coagulation coefficient at any given time but, since each collision should result in a change in the distribution, the distribution does not remain constant. However, the equation can be used to provide a 'snap shot' of the system at one particular time.

From sections 6.1 and 6.2 we know the size distribution and the number of species and by using the program in appendix 2 we calculated a value of 5.4×10^{-14} m^3s^{-1} for K_a. Multiplying by 1.34×10^{19} particles per m^3, calculated in section 6-4, gives an effective first order rate constant of 7.2×10^5 s^{-1}, which is orders of magnitude greater than that for flow through the reactor or diffusion to the reactor surface. This analysis then indicates that newly formed droplets will likely contact one another before reaching the reactor wall. It is expected that the larger particles we observed will act as “sinks” for very small particles, leaving few small particles to contact the surface directly.

7.0 Deposition onto a Metal Substrate

Metal surfaces have been shown to increase deposition, indicating a direct surface interaction (17-20, 105-115). Investigators have shown the coke which initially forms on the metal consists of filaments with a higher surface area than the pyrolytic carbon formed in the absence of a metal surface. This enhancement levels off after a short period of coking. This effect has been attributed to the coating of the metal surface. Changes in structure have been correlated with the length and severity of the deposition conditions. Changes in the deposition rate have also been correlated with the length and severity of the deposition conditions. However, the surface structure of the deposited material has not been correlated to the deposition rate. The purpose of this chapter is to extend the results of previous work to the conditions of this research and to establish a link between the surface structure of the deposited carbon and the rate of deposition.

The deposition rate of *pyc* was followed as a function of time for a metal substrate at a temperature and pressure of 1151 K and 40 kPa. A helical stainless steel (Incoloy 800 HT, a typical high temperature metal alloy used in industrial steam cracking furnaces) substrate, which had a surface area of 2.4 cm^2, was used to measure the deposition rate as a function of residence time. In contrast to deposition onto a quartz substrate the rate of deposition onto the metal substrate was substantially faster and was variable over a 120 minute period. The rate vs. time profile, illustrated in Figure 7-1 was far greater initially (region I), reached a brief plateau (region II), dropped off (region III) and reached another plateau (region IV) where the deposition rate remained stable for a 60 minute period.

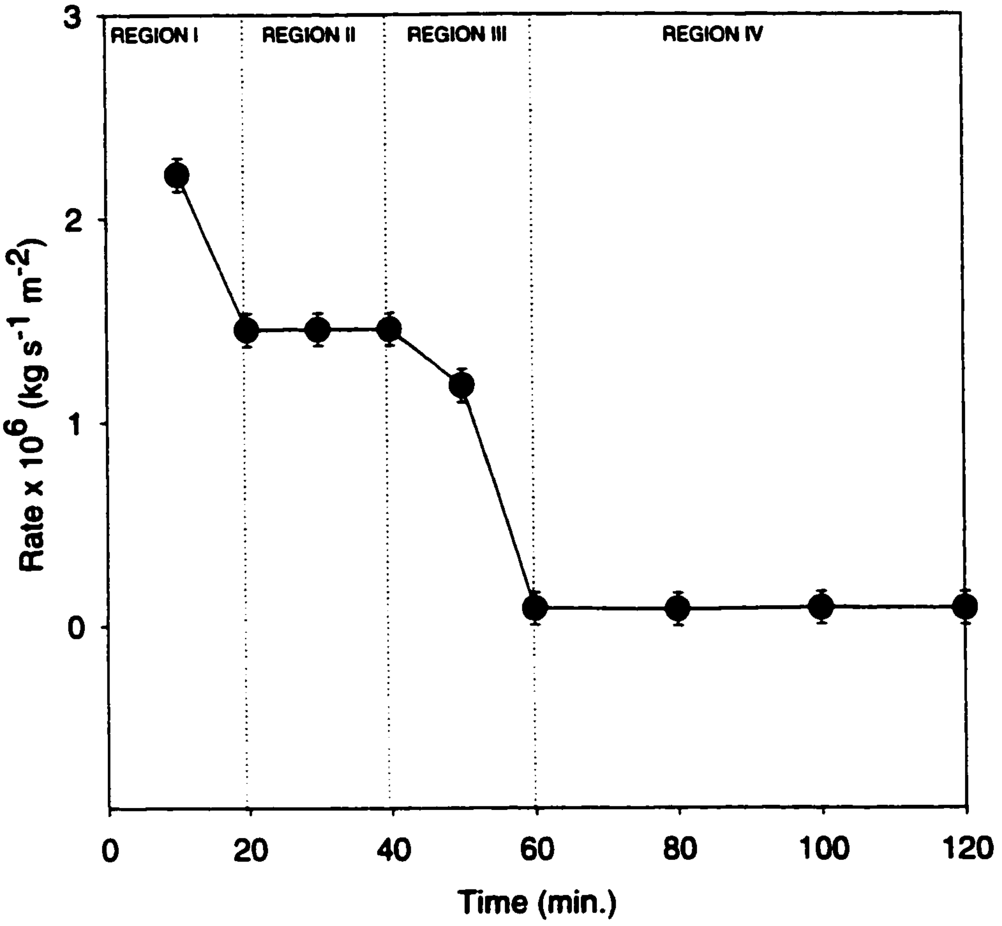

Figure 7-1: The average deposition rate on to a stainless steel substrate (Incoloy 800 HT) as a function of time.

Examination of the topography of the carbon coating formed on the different surfaces aided in providing a qualitative explanation of the deposition profile. Figures 7-2 A and B show a metal substrate before and after coating for 120 min. In Figure 7-2 A a clean metal surface was observed. In Figure 7-2 B the coated surface appeared black and rough indicating a large increase in the surface area. The thickness of the coating ranged from 0.1 to 0.3 mm.

The SEM images of the metal substrate revealed a vastly different topography than was observed for deposition onto a quartz substrate. Before deposition the metal surface, shown in Figure 7-3, was relatively smooth, revealing a number of shallow grooves, which were probably due to the mechanical cutting process that was used in preparing the substrate. In Figures 7-4 and 7-5 SEM images of the surface after deposition revealed that two distinct structures predominated. The outer surface structure of the deposited carbon, shown in Figure 7-4, consisted of spherical globules which were about 500 - 2000 nm in diameter. This outer portion was similar in structure to that observed by a number of researchers on metal surfaces coated with species meant to inhibit the formation of carbon (18). Removing the outer portion and examination of the interior of the coating revealed the distinctly different structure of twisted "tubes" or "wires" illustrated in Figure 7-5. This filamentous structure has been observed on a number of different metal surfaces (105,115) including Incoloy 800.

The structure and mechanism of formation of filamentous carbon and nanotubes have received much attention in the recent literature. The SEM analysis presented here can offer new insight into the observed changes in the deposition rate onto a metal

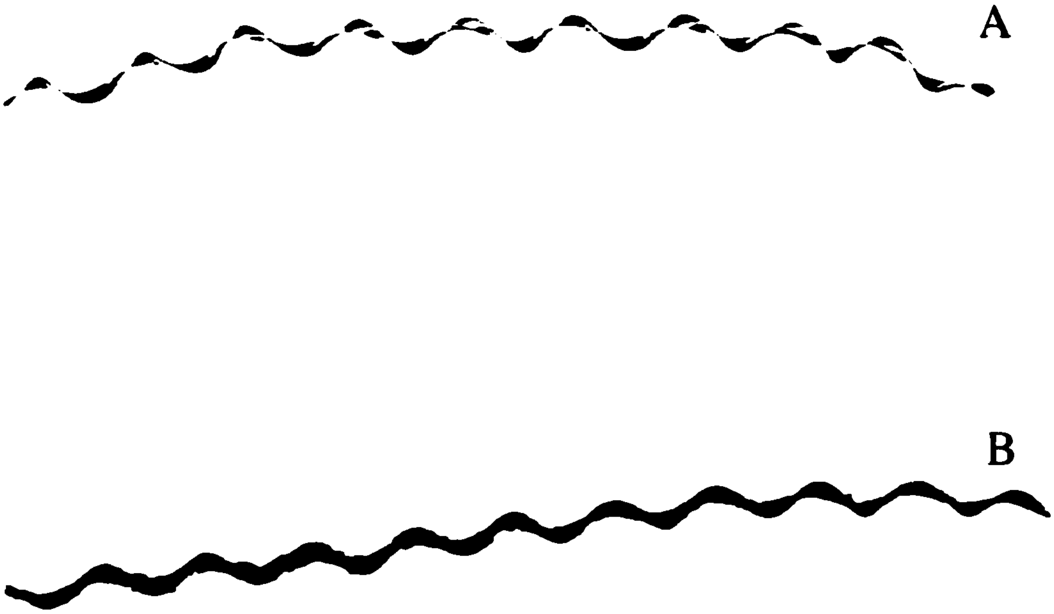

Figure 7-2 : Photographs of the clean metal substrate, A, and the coated substrate (Carbon deposited at 1150 K for 120 minutes with a flow rate of 26 sccm and a pressure of 40 kPa), B.

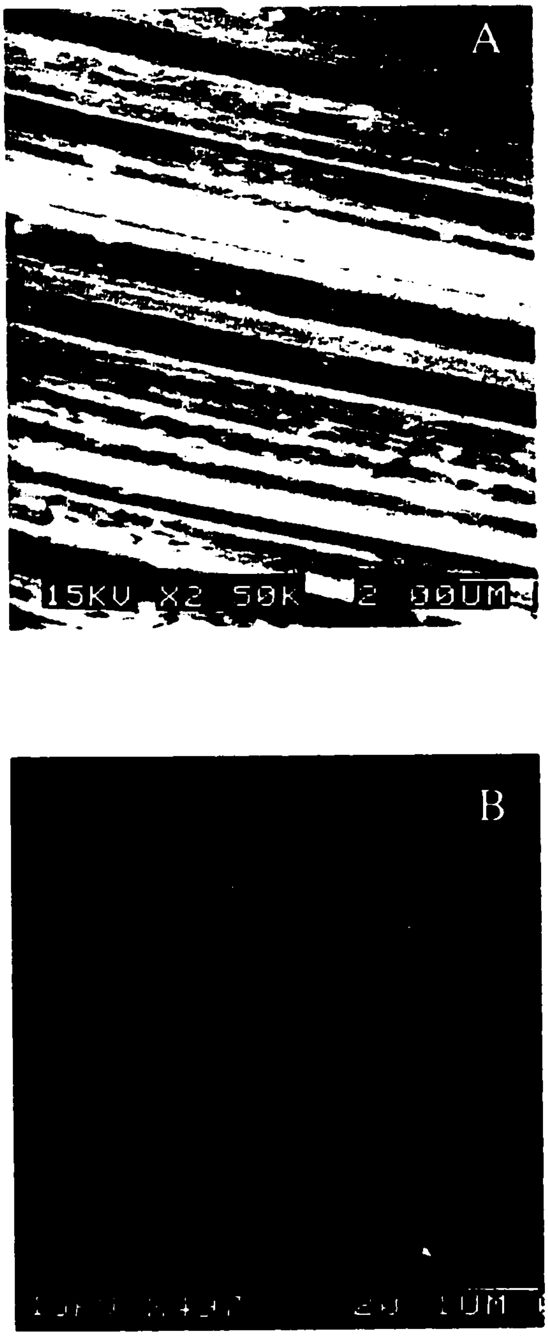

Figure 7-3: SEM image of the clean metal surface. A. 5500X. B. 550X

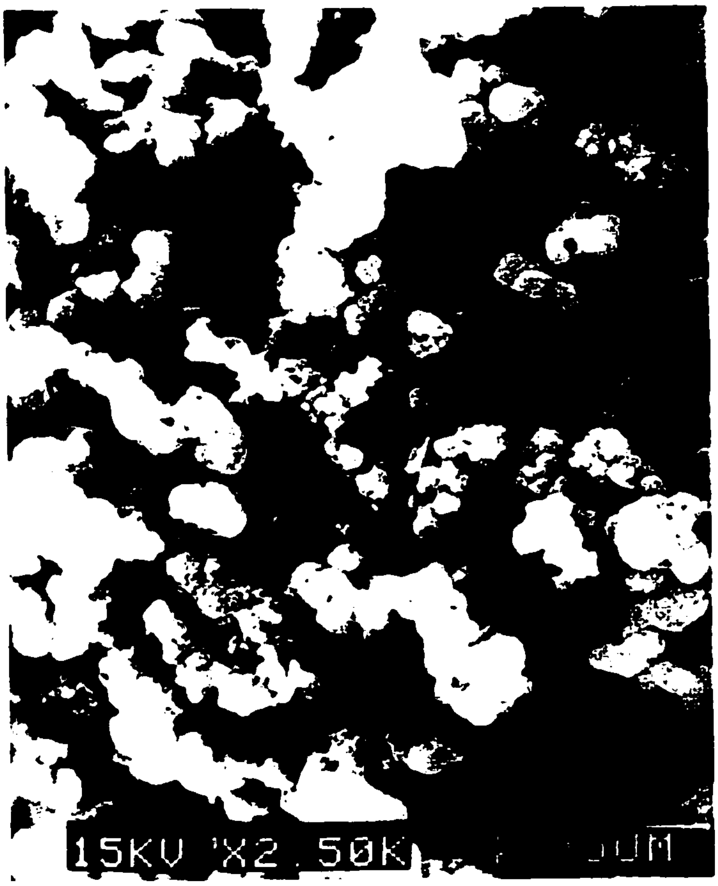

Figure 7-4: SEM image of the outer surface structure of the deposited carbon shown macroscopically in Figure 7-2. Carbon was deposited at 1150 K for 120 minutes with a flow rate of 26 sccm and a pressure of 40 kPa.

Figure7-5: An SEM image of the interior region of the coating. Carbon deposited at 1150 K for 120 minutes with a flow rate of 26 sccm and a pressure of 40 kPa.

substrate. The variation in the rate can be rationalized on the basis of surface structure by making a number of hypotheses. First one must suppose there were two main routes for carbon formation: one which was metal catalyzed, resulting in filamentous carbon and another route which depended only on the gas composition, not the chemical properties of the surface. Chapters 3 to 6 all support a deposition mechanism that does not depend on the chemical properties of the surface. Secondly, it is supposed that the rate of metal-catalyzed, filamentous carbon formation depended on the availability of active sites on the metal surface. The catalytic formation of filamentous carbon has been well studied, supporting the assumption of a metal-catalyzed, surface reaction.

Given these proposals and the observation of filamentous carbon in the interior of the carbon coating, it is reasonable that initially metal-catalyzed decomposition onto the metal surface dominated the deposition process, producing a coating with a high surface area at a relatively high rate. As the metal surface became coated the number of active sites available for growth was reduced and consequently the rate was reduced (region I in Figure 7-1). At the same time, however, an increase in surface area would have provided more space for large aromatic species to collide with the surface. The first plateau (region II in Figure 7-1) may have represented a region where the decrease in the rate of the metal-catalyzed mechanism was balanced by the increase in surface area and increase in the amount of material collected from the gas-phase. After about 40 minutes it is possible there was less metal surface available to catalyze the formation of filamentous carbon and that the rate dropped (region III in Figure 7-1) to a point where metal-catalyzed deposition was insignificant. Finally as the filamentous carbon became coated, the increase in surface area could have become less rapid and the rate relaxed to a steady value in the second plateau (region IV). Coating of the filamentous carbon is supported by the SEM image in Figure 7-5 where the spherical deposits were consistent with a carbon material deposited onto the wires.

In region IV the apparent rate was larger by a factor of 3.5 when depositing onto the metal substrate compared to the quartz substrate. However, when the substrate was removed from the system and examined it was apparent that the surface area of the substrate had increased. If the flat helical structure had been replaced by a cylindrical helical structure then the surface area would have increased by a factor of $\pi/2$. SEM images of the surface also indicated more surface area at the microscopic scale. Assuming the surface area due to the combination of factors tripled, the rate would have actually relaxed to a value very close to that observed for the quartz substrate. Previous studies have indicated the migration of metal particles to the carbon surface occurs in other systems. Therefore, it is also possible that the contribution of the metal-catalyzed mechanism was still significant, even though the metal surface was completely covered.

Further evidence for competition between a metal-catalyzed and gas-phase decomposition is provided by the examination of material deposited on a metal substrate at a higher temperature of 1185 K. For this sample a metal substrate was placed down the entire length of the reactor and the carbon was deposited for 3 hours at a 6 sccm flow rate of ethane. Examination of the substrate surface as a function of the reactor length revealed an interesting trend. Close to the reactor entrance, at the beginning of the hot zone, where the reactor residence time was less than 1 second, material similar to that deposited at 1150 K was observed. Further into the reactor, where the residence time increased to about 3 s, the material was substantially different, in that any remnant of the filamentous carbon structure has been replaced by the valleys and mounds of apparently globular material illustrated in Figure 7-6. In the center of the hot zone where the residence time increased to 6 s the topography was almost devoid of structure (Figure 7-7A), with areas drifting up and down and a small number of large spherical droplets as illustrated in the lower left corner of Figure 7-7B. This area did not appear fundamentally different than that observed on the quartz substrate. This may indicate that at this point in the deposition process the metal was completely coated and the nature of the substrate was no longer relevant to the deposition process.

This effect was further illustrated by removing the carbon coating from the substrate (deposited in a region of approximately 6s residence time) and examining the exterior of the coating, the interior which was against the metal surface and a cross-section of the coating. Figure 7-7 which has already been addressed showed the exterior. Figure 7-8 showed the underside of the coating, indicating a substantially different structure. In this case the material which was in contact with the metal surface appeared to have a structure similar to that observed at lower temperatures in Figure 7-4 but was made up of much smaller filaments. The cross-section of the coating, shown in Figure 7-9 indicated a transition between the two different structures, starting at the rough surface and ending at the smooth surface with spherical protrusions. A string of spheres which was less commonly observed is also illustrated in Figure 7-9.

The cross-section indicated that the coating varied between 2 to 8 µm. This was an order of magnitude lower than that observed for the lower temperature deposition indicated in Figure 7-5. Clearly the severe reaction conditions produced a substantially thinner coating. This observation appears counter-intuitive. Upon closer observation the

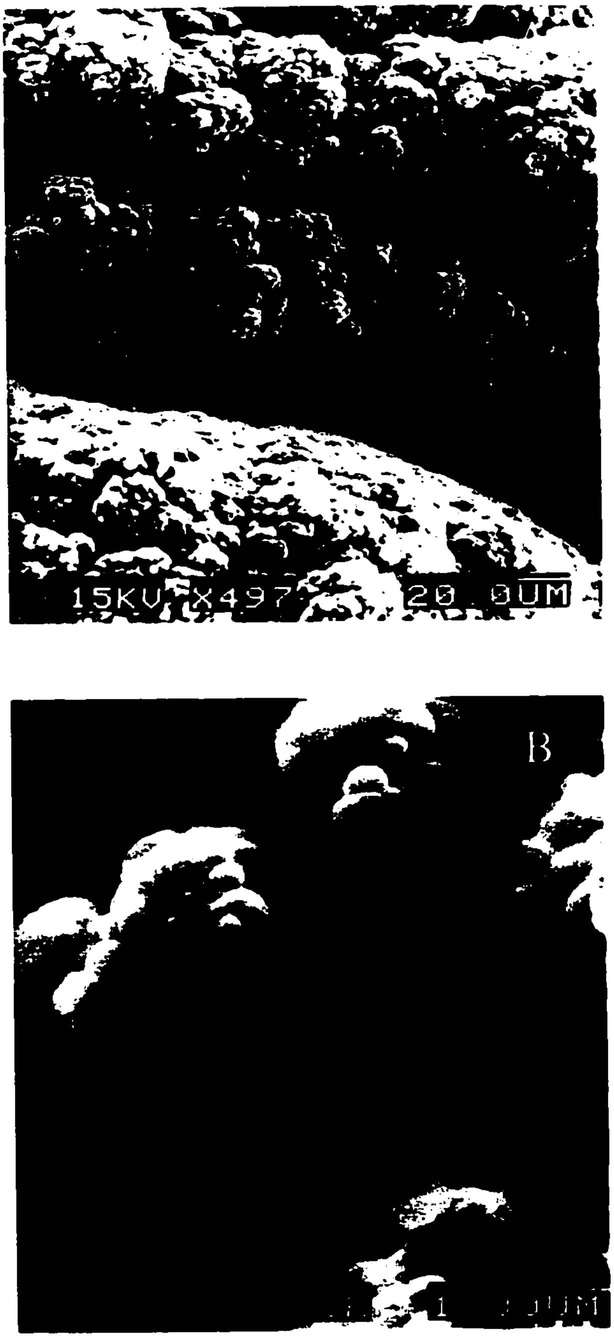

Figure 7-6: SEM images of the coated substrate surface at a residence time of 3 s, a temperature of 1185 K and a pressure of 40 kPa. A. 496X. B. 9950X

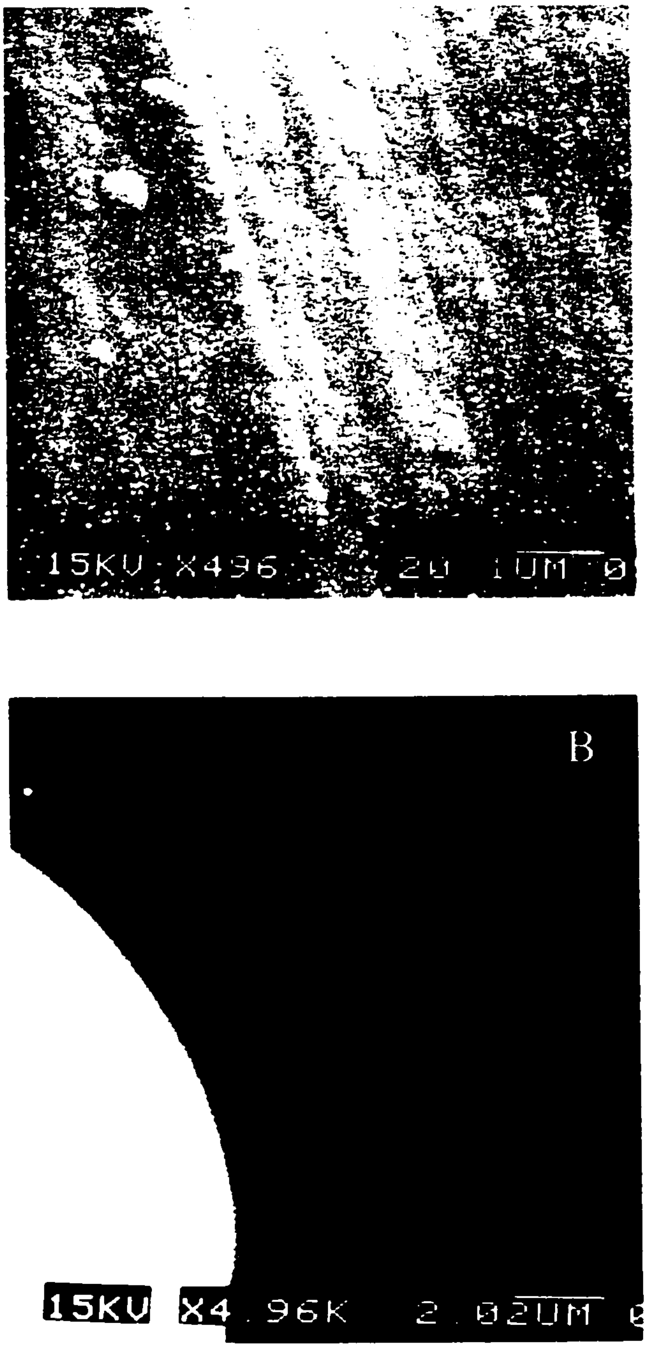

Figure 7-7: SEM images of the substrate surface located in the central region of the hot zone at a residence time of 6 s, a temperature of 1185 K and a pressure of 40 kPa. A. 497X. B. 9950X.

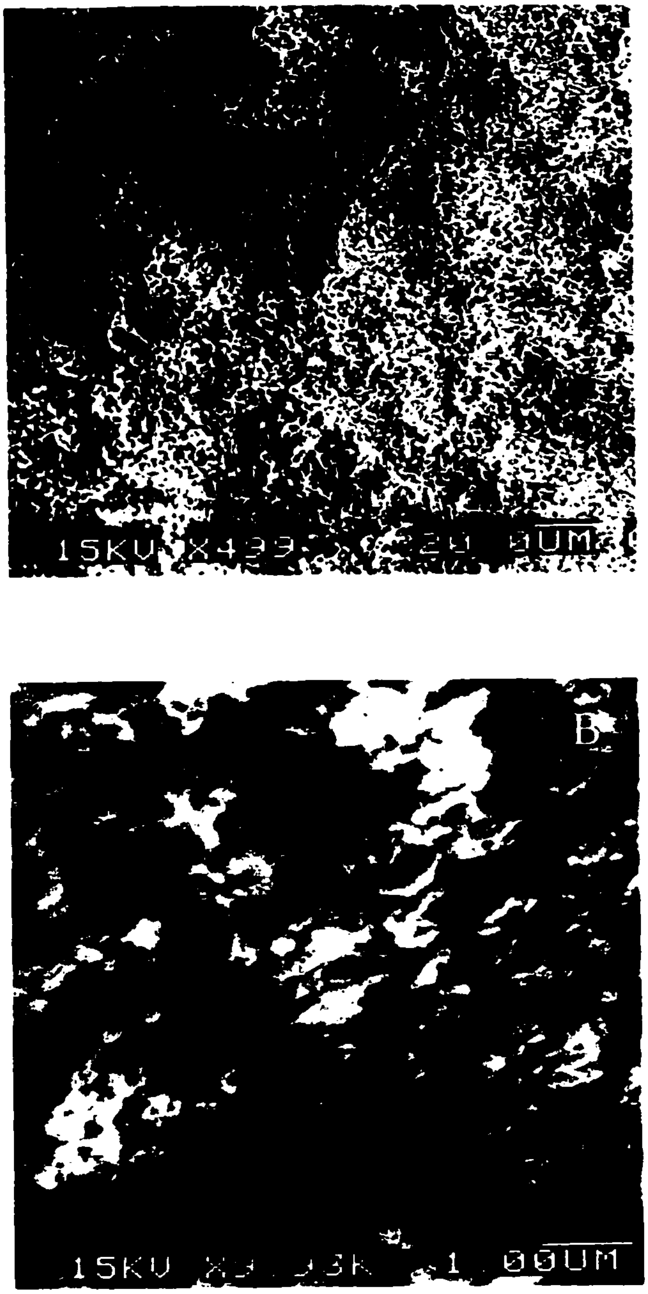

Figure 7-8: SEM image of the underside of a sample of the pyc coating removed from the substrate surface located in the central region of the hot zone at a residence time of 6 s, a temperature of 1185 K and a pressure of 40 kPa. A. 497X. B. 9930X.

Figure 7-9: SEM image of the cross section of the pyc coating removed from the substrate surface located in the central region of the hot zone at a residence time of 6 s, a temperature of 1185 K and a pressure of 40 kPa.

SEM images suggest a qualitative explanation of the results. The predominance of globular material deposited at the higher temperature indicated the steel was coated quickly with a dense layer of *pyc* and further metal-catalyzed carbon filament formation was not possible. On the other hand, at lower temperatures the contribution of gas-phase decomposition may have been much less and the coating was predominantly due to metal-catalyzed formation of filamentous carbon.

8.0 Summary and Conclusions

Ethane is a simple molecule. On pyrolysis, it produces ethylene, the cornerstone of the petrochemical industry. It also produces a spectacular array of aromatic compounds, about which much remains to be learned. Cracking processes dominate at low conversion. However, molecular growth becomes increasingly important as conversion increases. The majority of this work was concerned with molecular growth and the relationship between molecular growth and pyrolytic carbon deposition.

This research has provided an analysis of the main products of ethane pyrolysis coinciding with the surface deposition of pyrolytic carbon. In Chapter 3 a consideration of the product composition revealed that the acetylene concentration reached a maximum early. Benzene concentration reached a maximum at about the same time as the rate of formation of solids on the reactor surface. The rate of benzene formation was found to be third order with respect to acetylene concentration. This implied that, as has been observed for the pyrolysis of pure acetylene, three acetylene molecules may have reacted to form benzene. The rate of carbon deposition was found to be directly proportional to the concentration of benzene in the system. This was consistent with a reaction of benzene (or some other intermediate which had a concentration proportional to that of benzene) representing the bottleneck on the route to *pyc* deposition. In the pyrolysis of pure benzene a first-order dependence on benzene concentration was also observed. In this system the rate constant, k_{ab}, was larger. This was not consistent with a direct reaction of benzene to form carbon but it was consistent with some other intermediate which had a concentration proportional to benzene reacting to form carbon.

In Chapter 4 the yields of ten liquid products were established as a function of residence time. These were small aromatic compounds, most of which reached maximum yields at the same time as the rate of deposition of carbon. Nineteen aromatic compounds were observed and tentatively identified. An additional fifty-three compounds were observed but not identified. Products with even numbers of carbon atoms were found to dominate. The analysis was consistent with the growth of aromatics by addition of acetylene units, accompanied by consolidation and partial dehydrogenation. Species were observed in the 100- to 700-amu range. The observation of these species is consistent with the hypothesis that PAH condensation and dehydrogenation were partially responsible for the deposition of carbon. These results indicated that there were sufficient PAHs present in the system to allow for formation of the observed amount of carbon by one or both of the following methods: direct decomposition on the surface from the gas phase or condensation as a liquid followed by deposition.

Ethane, as demonstrated in Chapter 5, can also be transformed, in part, at high temperatures and long residence times, to form an aerosol. This aerosol could deflect and attenuate a laser beam just as the droplets in fog or a cloud can block the sunlight. When viewed with the naked eye, the aerosol appeared to glow with an orange light because of the scattering of light originating at the furnace and at the reactor walls. The aerosol was collected on a dropped quartz plate and examined by SEM, TEM and fluorescence spectroscopy. The fluorescence spectrum was consistent with the presence of PAHs of high molecular weight. The SEM and TEM analyses indicated the presence of discrete spherical units, which may have partially flattened upon impact with the surface. These results were consistent with the presence of a carbon precursor which was neither a discrete aromatic molecule nor a soot particle, but which had a structure that was in between.

The SEM analysis indicated large species were preferentially collected on the face of the substrate. This observation was consistent with a collection mechanism involving impaction. The analysis also indicated smaller species were preferentially collected on the side of the substrate. The size distribution of particles collected on the side of the substrate was consistent with a collection mechanism involving diffusion.

The side distribution was used to calculate the average rate at which material deposited onto the side of the substrate. These results indicated that a large fraction (36 %) of the deposited carbon in the ethane pyrolysis system could have been formed by deposition of the observed aerosol. Assuming species defused onto the side of the substrate a gas-phase size distribution for the aerosol was established. In order to further examine the role of aerosols in this system the gas-phase number density was also estimated using laser extinction data. This number density was a factor of five to twenty-three less than that calculated by diffusion.

In Chapter 3 it was shown that small, gas-phase species were not direct precursors to carbon under these conditions. By default, then, it is suspected that the majority of deposited material was formed by direct deposition of aromatics on the carbon surface or by condensation of aromatics in the gas-phase to form particles which then deposited on reactor surfaces. The proportion of the carbon originating directly from aromatics to that from particulates could not be established from these results.

Metal surfaces were shown to increase rates of deposition by a surface-catalyzed decomposition. The coke which initially formed on the metal surface was shown to be filamentous. This rate decreased after a short period of coking. The reduction in rate was correlated to a change in the surface from filamentous carbon to *pyc*. After a certain time, the chemical composition of the surface did not appear to have an effect on the rate of deposition or on the topology.

The experimental results provided in this work reveal the dazzling complexity of the ethane pyrolysis system. For several decades the deposition of carbon onto reactor surfaces has been described by a single, simple, first-order decomposition. Over the last two decades, researchers in the combustion field have investigated and are beginning to model the complex molecular-growth steps in soot formation. A number of researchers have shown that similar, gas-phase, molecular growth is important during lower temperature pyrolysis. Ockham's razor would suggest the simplest model which can adequately describe the experimental results is the preferred description. Recent work in the field of carbon formation has vastly increased the complexity of the simplest model which can describe the experimental results. At first sight, perhaps, these complications are not desirable; but with this complexity comes insight into the inhibition, acceleration and control of the formation and structure of pyrolytic carbons. Armed with a knowledge of the processes of molecular growth in pyrolysis, one can began in a more effective manner to combat these processes, when they are unwanted, and to enhance them when they are desired.

9.0 Future Directions

The role of radicals was not established in this work. Modeling can test the viability of suggested pathways. We have started this modeling work and are working in collaboration with H. Bohm to develop a model which can quantitatively describe molecular growth in the pyrolysis system.

The work thus far has provided enough insight into the system that a solid attempt at observing the aromatic radicals at a variety of conditions is warranted. One way to do this would be *in situ* MS analysis. A probe could be modified in such a way that material could flow through the probe and into the source. In order to selectively ionize the material exiting the reactor, an EI source could be used, initially. Eventually various wavelengths of light could be used to selectively ionize radicals. The reactor would have to be extremely small for this analysis. Recent work in Dr. Pacey's group has focused on micro-reactors and it is expected that such a reactor could be constructed. Another problem relates to the pressure-drop associated with an EI source. A number of options are available: one could borrow from molecular beam experiments and sample through a pinhole at the reactor exit, one could flow through a capillary and create a controlled pressure drop experiment and finally one could try flowing directly into an APCI system.

Reviewing and interpreting these experiments, we believe that we have observed an important and unusual type of chemical intermediate, lying between discrete aromatic species and soot. Direct, experimental research on this intermediate is just beginning. We are currently collaborating with mass spectrometrists in order to obtain a mass spectrum of the material. In order to further characterise these droplets, a method of collecting larger samples must be developed. The light-attenuation experiments provided a starting point for the particle-size analysis. A more thorough characterisation should provide the necessary information to better estimate optical properties. Given this information, a scattering experiment could be used to determine more accurate distributions and number densities of the aerosol. This information should aid in the determination of the proportion of carbon which is due to aerosol deposition.

Once a reliable method of determining number densities and distributions is established, it would also be interesting to study the dependence of the size and concentration of the droplets on such experimental parameters as the pressure, temperature and residence time. Transmission electron microscopy and light scattering experiments may also be used to observe smaller, newly-formed droplets and to measure the rates of nucleation and agglomeration of droplets. It would be interesting to study the bulk and surface reactions of these droplets, and their transformation to soot, carbon black or pyrolytic carbon.

Chapters 3 - 6 have all reported a strong correlation between the amounts of acetylene and benzene present in the system and the amounts of large PAHs and pyrolytic carbon. In order to further examine this relationship, the effect of adding these species to the pyrolysis mixture could be examined. Further, the effect of adding species expected to inhibit deposition could also be examined. This work has been started and some of the results are summarized in Appendix1. The addition of hydrogen and hydrogen sulfide inhibited the formation of acetylene, benzene and carbon while enhancing the formation of ethylene, methane and propylene; these effects were greater for the addition of hydrogen sulfide than for hydrogen. The results indicated that species which may donate a hydrogen radical generally reduced the acetylene and aromatic content and coking over a wide temperature range. These results may indicate that a reduction of the vinyl radical concentration by the addition of a hydrogen-donating species reduced unwanted products while increasing the yield of ethylene. Due to the importance of ethylene production, these preliminary experiments indicate further work in this area is warranted.

The origin of the variable microstructure of pyrolytic carbons deposited under different conditions is not well understood. Isotropic (less ordered) carbons are generally the result of more severe conditions, high temperatures and long reaction times; whereas laminar (more ordered) carbons are generally the result of less severe reaction conditions. Due to the industrial importance of carbon materials, it is important to understand why different pyrolysis conditions produce different microstructures. The results of this thesis indicate a competition between direct decomposition of molecular species and deposition of particles formed in the gas phase. The microstructure for carbons could be established as a function of reaction time using standard metallurgical methods. It is quite possible that the changing microstructure could be correlated with the changing nature of the gas phase.

Appendix 1: Raw Data For the Gaseous, Liquid and Solids Analyses.

Table A1-1: Raw data for deposition onto an open substrate (Chapter 3) at a temperature of 1151 K, a pressure of 40 kPa and a flow rate of 26 sccm.

TIME (min.)	RATE (μg min.$^{-1}$ cm^{-2})
12	1.401
26	1.631
47	1.580
67	1.618
87	1.592

Table A1-2: Raw data for deposition onto a closed substrate (Chapter 3) at a temperature of 1151 K, a pressure of 40 kPa and a flow rate of 26 sccm.

TIME (min.)	RATE (μg/min. cm^2)
10	2.123
20	1.699
30	1.486
50	1.471
70	1.482
99	1.490

Table A1-3: The pyrolytic carbon deposition rate for a series of nominal residence times and 3 pressures at a constant temperature of 1185 K (Chapter 3).

PRESSURE (300 TORR)		PRESSURE (200 TORR)		PRESSURE (100 TORR)	
residence time (s)	deposition rate (μg/min.)	residence time (s)	deposition rate (μg/min.)	residence time (s)	deposition rate (μg/min.)
.63	27.0	-	-	-	-
.96	39.0	-	-	-	-
1.1	45.3	1.2	17.5	1.2	6.3
1.6	52.0	-	-	-	-
2.6	72.1	2.4	21.4	2.4	10.3
4.0	88.0	3.6	34.0	3.6	13.0
4.8	102	-	-	-	-
5.2	110	-	-	-	-
7.7	141	7.3	59.0	7.3	18.8
12.8	173	14.7	62.5	14.7	24.4
19.0	146	-	-	-	-

Table A1-4: GC analysis and the assigned mass to charge ratios for all species analyzed in the gas phase (Chapter 3). (, a. 0 °C for all analysis on column 2, b. 50 °C, c. 100 °C, d. 225 °C)

Compound	RETENTION TIME (S)				m/z
	Standard mixture		Product mixture		
	column 1	column 2	column 1	column 2	
hydrogen	-	24^{a}	-	25^{a}	-
methane	90^{b}	47	95^{b}	46	16
ethane	473^{b}	68	474^{b}	70	30
ethylene	330^{b}	94	327^{b}	95	28
acetylene	-	685	-	694	26
propane	533^{c}	-	-	-	-
propylene	472^{c}	354	472^{c}	350	42
butane	1511^{c}	-	-	-	-
butadiene	1644^{c}	-	1630^{c}	-	54
benzene	222^{d}	-	217^{d}	-	78
toluene	364^{d}	-	364^{d}	-	92
styrene	709^{d}	-	694^{d}	-	104

a. Isothermal column temperature, 0 °C for all analysis on column 2.
b. Isothermal column temperature, 50 °C.
c. Isothermal column temperature, 100 °C.
d. Isothermal column temperature, 225 °C.

Table A1-5: Partial pressure of the gas phase components of the product mixture at a constant pressure and temperature of 300 Torr and 1185K for several residence times (Chapter 3).

Residence time (s)	.64	.85	1.1	1.6	3.4	4.8	7.7	9.6	19.1
$P_{hydrogen}$ (Torr)	123	138	129	135	142	146	145	149	152
$P_{methane}$ (Torr)	35.5	40.5	46.5	47.3	53.4	72.4	68.6	81..0	86.6
$P_{acetylene}$ (Torr)	9.28	11.4	12.3	12.2	12.1	10.5	10.6	8.20	7.33
$P_{ethylene}$ (Torr)	115	89.7	92.2	82.6	68.0	48.9	51.8	38.3	37.7
P_{ethane} (Torr)	6.3	6.57	4.53	3.94	3.17	2.72	2.81	2.27	1.84
$P_{propylene}$ (Torr)	1.68	1.71	1.27	1.18	1.00	0.735	0.749	0.569	0.406
$P_{butadiene}$(Torr)	2.37	2.47	1.68	1.53	1.05	0.691	0.416	0.506	0.660
$P_{benzene}$ (Torr)	5.91	6.48	6.22	9.79	13.0	12.8	15.1	14.3	13.2
total	299.0	297.2	293.8	293.9	294.0	295.8	294.8	294.5	300.0

Table A1-6: The mole % of the gas phase components of the product mixture at a constant pressure and temperature of 300 Torr and 1185K respectively for several residence times (Chapter 3).

Residence time (s)^a	.64	.85	1.1	1.6	3.4	4.8	7.7	9.6	19.1
$X_{hydrogen}$ (%)	41.0	46.1	43.0	45.1	47.7	49.0	48.3	49.8	50.8
$X_{methane}$ (%)	11.8	13.4	15.5	15.8	17.8	23.8	22.9	27..0	28.9
$X_{acetylene}$ (%)	3.09	3.80	4.12	4.06	4.03	3.51	3.52	2.73	2.44
$X_{ethylene}$ (%)	38.5	29.9	30.7	27.9	22.7	16.3	17.3	12.8	12.6
X_{ethane} (%)	2.12	2.19	1.51	1.31	1.06	0.91	0.94	0.76	0.61
$X_{propylene}$ (%)	0.56	0.57	0.42	0.39	0.33	0.24	0.25	0.19	0.14
$X_{butadiene}$(%)	0.79	0.83	0.56	0.51	0.35	0.23	0.14	0.17	0.22
$X_{benzene}$ (%)	1.97	2.49	2.41	3.26	4.34	4.27	5.04	4.76	4.40
total	99.7	99.4	98.3	97.9	98.3	98.0	98.3	98.1	100

a. nominal residence time

Table A1-7: **Deposition rate and partial pressure of products measured at the reactor exit for variable total pressure experiments and dilution experiments where the total pressure was constant but the partial pressure of reagent was changed (Chapter 3).**

CONSTANT TOTAL PRESSURE (400 TORR AND 2.2S)			VARIABLE TOTAL PRESSURE (50-350 TORR AND 1.1S)		
deposition rate (μg/min.)	P_{acet} (Torr)	P_{ben} (Torr)	deposition rate (μg/min.)	P_{acet} (Torr)	P_{ben} (Torr)
6.75	5.56	1.89	4.9	2.45	0.17
-	-	-	7.0	4.08	0.64
14.35	7.43	4.40	8.2	5.15	1.22
-	-	-	19.0	9.40	3.06
23.17	8.61	7.45	22.7	10.8	4.13
-	-	-	27.0	12.2	5.48
32.5	9.28	10.24	33.9	12.9	7.27
44.1	10.01	12.56	-	-	-

Table A1-8: **The rate of deposition and the partial pressure and concentration of benzene and acetylene as a function of the temperature (Chapter 3).**

Temp. (K)	acetylene (torr)	benzene (torr)	R_c (ug/min.)	benzene (umol/l)	R_c (umol/ls)
1185				160	3.52
1172	7.6	10.1	28	138.2	2.16
1151	10.06	8.16	12.6	113.7	0.97
1131	5	4.8	5.4	68.1	0.42
1113	4.1	3.2	3.2	45.9	0.25

Table A1-9: The yields of liquid products for several residence times at 300 Torr and 1185 K (Chapter 4). Work performed by Rana Filfil (132).

NOMINAL RESIDENCE TIME (s)	COLLECTION TIME (min.)	MASS OF TARS RECOVERED (g)
1.1	60	0.7860
1.1	60	0.7756
1.1	60	0.8212
1.1	60	0.7866
3.4	44	0.4821
3.4	44	0.4682
5.6	60	0.2980
5.6	60	0.4448
16.8	60	0.1500
16.8	60	0.1680
33.6	60	0.0494
33.6	60	0.0666

Table A1-10: Data used in the calculation of the weight % yield of liquid products for several residence times at constant pressure and temperature of 300 Torr and 1185 K, respectively. Data presented in the third column correspond to average values (Chapter 4). Work performed by Rana Filfil (132).

NOMINAL RESIDENCE TIME (s)	REAGENT FLOW RATE (µg/s)	MASS OF LIQUID PRODUCTS (g)	LIQUID FLOW RATE OUT OF THE REACTOR (µg/s)	YIELD EQ. 7 (%)
1.1	2009	0.794 ± 0.02 [a]	220.6	10.4
3.4	709.8	0.475[b]	175.9	24.8
5.6	425.9	0.445[b]	123.6	28.9
16.8	142.0	0.159[b]	44.2	31.0
33.6	71.0	0.0581[b]	16.1	22.7

a. reported error is estimated from one half the standard deviation for three samples

b. samples were taken in duplicate and the average is reported

Table A1-11: Retention times for standards analyzed by HPLC under the conditions described in Chapter 2. Work performed by Rana Filfil (132).

COMPOUND	STANDARD RETENTION TIME (MIN.)
Benzene	5.17
Toluene	6.14
Styrene	6.55
Indene	6.64
Xylene	7.30
Naphthalene	7.25
α-methyl styrene	7.77
Acenaphthylene	8.04
Fluorene	9.60
Phenanthrene	10.59
Anthracene	11.50
Fluoranthene	12.32
Pyrene	12.94

Table A1-12: Composition of liquid samples collected. Reported uncertainties are the standard deviations calculated from the repeated chromatograms of different samples formed at the same experimental conditions (Chapter 4). Work performed by Rana Filfil (132).

RESIDENCE TIME (S)	1.1	3.4	5.6	16.8	33.6
Benzene	53.0±1.1	47.9±5.4	37.3±1.1	47.0±3.8	43.0±6.7
Styrene/Indene[a]	5.87±0.50	3.79±0.20	3.72±0.25	2.36±0.20	3.18±0.40
Naphthalene	5.18±1.79	12.3±0.6	17.3±3.0	6.94±0.18	12.9±2.0
Acenaphthylene	2.49±0.35	4.29±0.23	5.62±0.54	4.92±0.22	4.56±0.87
Fluorene	0.73±0.07	1.12±0.18	1.06±0.19	0.66±0.05	0.65±0.12
Phenanthrene	1.20±0.33	2.48±0.17	3.92±0.50	3.12±0.25	2.72±0.54
Anthracene	0.60±0.08	1.64±0.19	1.91±0.34	1.47±0.27	1.74±0.09
Fluoranthene	0.84±0.25	2.47±0.37	3.69±0.20	3.22±0.25	3.03±0.62
Pyrene	0.42±0.5	1.82±0.17	3.00±0.27	2.94±0.30	2.76±0.60
Total	70.3	77.8	77.5	72.6	74.5

a. Peak contained styrene and indene but was quantified using only a styrene standard.

Table A1-13: Yield (weight %) of individual liquid products. Errors associated with the calculations of yields of individual liquid products were calculated from the repeated runs of different samples formed at the same experimental conditions (Chapter 4). Work performed by Rana Filfil (1992).

RESIDENCE TIME (S)	1.1	3.4	5.6	16.8	33.6
Benzene	5.49 ± 0.27[a]	12.1 ± 1.6	12.6 ± 2.2	15.2 ± 0.7	9.55 ± 0.48
Styrene/Indene[b]	0.55 ± 0.01	0.97 ± 0.03	1.08 ± 0.10	0.78 ± 0.01	0.61 ± 0.03
Naphthalene	0.65 ± 0.06	3.10 ± 0.1	4.07 ± 0.54	4.46 ± 0.16	2.86 ± 0.05
Acenaphthylene	0.26 ± 0.03	1.09 ± 0.07	1.34 ± 0.24	1.53 ± 0.13	1.01 ± 0.02
Fluorene	0.08 ± 0.01	0.28 ± 0.05	0.24 ± 0.03	0.21 ± 0.02	0.14 ± 0.01
Phenanthrene	0.09 ± 0.02	0.63 ± 0.03	0.61 ± 0.12	1.01 ± 0.01	0.60 ± 0.02
Anthracene	0.06 ± 0.01	0.38 ± 0.07	0.42 ± 0.02	0.43 ± 0.07	0.33 ± 0.03
Fluoranthene	0.08 ± 0.02	0.40 ± 0.07	0.73 ± 0.07	1.06 ± 0.10	0.67 ± 0.03
Pyrene	0.04 ± 0.01	0.63 ± 0.10	0.64 ± 0.10	0.97 ± 0.02	0.61 ± 0.03
Total	7.30	19.6	21.7	25.7	16.4

a, represents the standard deviation of a total of 9 LC runs on 4 separate samples. b, mass spec analysis indicates a mixture of styrene and indene but the material was quantified using a styrene standard.

Table A1-14: Data from HPLC-APCI-MS and DLI-APCI-MS analysis for the calculation of weight % (Chapter 4) of a sample collected at a temperature of 1185 K, a pressure of 40 kPa and a residence time of 3.4 s.

m/z	intensity	int*MWT	wt %
2.02E+02	9.30E+05	1.88E+08	6.30E-01
2.26E+02	7.68E+05	1.74E+08	5.82E-01
2.26E+02	1.02E+06	2.30E+08	7.70E-01
2.54E+02	2.94E+05	7.46E+07	2.50E-01
2.52E+02	1.70E+05	4.27E+07	1.43E-01
2.52E+02	9.04E+04	2.28E+07	7.63E-02
2.52E+02	9.04E+04	2.28E+07	7.63E-02
2.52E+02	5.65E+04	1.42E+07	4.77E-02
2.52E+02	6.44E+05	1.62E+08	5.44E-01
2.76E+02	2.00E+05	5.51E+07	1.85E-01
2.78E+02	3.76E+05	1.05E+08	3.50E-01
2.76E+02	5.88E+05	1.62E+08	5.43E-01
2.76E+02	3.53E+05	9.73E+07	3.26E-01
2.76E+02	2.23E+05	6.16E+07	2.06E-01
2.76E+02	4.35E+05	1.20E+08	4.02E-01
2.78E+02	2.59E+05	7.19E+07	2.41E-01
2.76E+02	9.64E+05	2.66E+08	8.91E-01
3.00E+02	4.23E+05	1.27E+08	4.25E-01
3.02E+02	1.86E+05	5.61E+07	1.88E-01
3.02E+02	5.57E+04	1.68E+07	5.63E-02
3.02E+02	4.18E+04	1.26E+07	4.22E-02
3.00E+02	1.28E+05	3.83E+07	1.28E-01
3.26E+02	3.25E+04	1.06E+07	3.55E-02
3.26E+02	5.80E+04	1.89E+07	6.33E-02
3.26E+02	5.34E+04	1.74E+07	5.83E-02
3.26E+02	4.18E+04	1.36E+07	4.56E-02
3.26E+02	4.64E+04	1.51E+07	5.07E-02
3.28E+02	1.55E+05	5.10E+07	1.71E-01
3.28E+02	1.16E+05	3.80E+07	1.27E-01
3.26E+02	8.12E+04	2.65E+07	8.87E-02
3.28E+02	2.78E+04	9.13E+06	3.06E-02
3.50E+02	9.60E+03	3.36E+06	1.13E-02
3.50E+02	7.20E+04	2.52E+07	8.44E-02
3.50E+02	2.52E+04	8.82E+06	2.95E-02
3.26E+02	2.28E+04	7.43E+06	2.49E-02
3.50E+02	9.60E+03	3.36E+06	1.13E-02
3.74E+02	1.20E+04	4.49E+06	1.50E-02
3.74E+02	9.10E+03	3.40E+06	1.14E-02

3.78E+02	1.08E+03	4.10E+05	1.37E-03
4.00E+02	2.17E+03	8.67E+05	2.90E-03
3.98E+02	1.95E+03	7.76E+05	2.60E-03
3.02E+02	1.20E+05	3.62E+07	1.21E-01
3.14E+02	5.50E+04	1.73E+07	5.79E-02
3.26E+02	1.05E+05	3.42E+07	1.15E-01
3.40E+02	3.80E+04	1.29E+07	4.33E-02
3.52E+02	6.00E+04	2.11E+07	7.08E-02
3.66E+02	2.00E+04	7.32E+06	2.45E-02
3.76E+02	2.30E+04	8.65E+06	2.90E-02
3.90E+02	1.00E+04	3.90E+06	1.31E-02
4.00E+02	1.30E+04	5.20E+06	1.74E-02
4.16E+02	4.20E+03	1.75E+06	5.85E-03
4.26E+02	4.50E+03	1.92E+06	6.42E-03
4.40E+02	2.66E+03	1.17E+06	3.92E-03
4.52E+02	2.66E+03	1.20E+06	4.03E-03
4.64E+02	1.80E+03	8.35E+05	2.80E-03
4.78E+02	1.60E+03	7.65E+05	2.56E-03
4.90E+02	1.00E+03	4.90E+05	1.64E-03
5.00E+02	6.36E+02	3.18E+05	1.07E-03
5.14E+02	4.09E+02	2.10E+05	7.04E-04
5.27E+02	3.41E+02	1.80E+05	6.02E-04
5.38E+02	2.59E+02	1.39E+05	4.67E-04
5.52E+02	1.82E+02	1.00E+05	3.36E-04
5.65E+02	1.70E+02	9.63E+04	3.23E-04
5.80E+02	1.36E+02	7.91E+04	2.65E-04
5.94E+02	8.18E+01	4.86E+04	1.63E-04
6.06E+02	1.56E+02	9.43E+04	3.16E-04
6.18E+02	8.89E+01	5.49E+04	1.84E-04
6.32E+02	1.06E+02	6.67E+04	2.23E-04
6.45E+02	8.78E+01	5.66E+04	1.90E-04
6.54E+02	4.44E+01	2.91E+04	9.74E-05
6.68E+02	4.44E+01	2.97E+04	9.95E-05
6.82E+02	4.44E+01	3.03E+04	1.02E-04

Table A1-15: Data for the estimation of the concentration of all observed molecular species (Chapter 4) of a sample collected at a temperature of 1185 K, a pressure of 40 kPa and a residence time of 3.4 s.

species	mol%[a]	wt%	mol%[b]	mass (amu)	partial pressure (torr)	conc. (mol/m^3)
H2	4.77E+01	5.72E+00	4.86E+01	2.00E+00	1.46E+02	1.97E+00
CH4	1.78E+01	1.71E+01	1.81E+01	1.60E+01	5.44E+01	7.37E-01
C2H2	4.03E+00	6.29E+00	4.11E+00	2.6E+01	1.23E+01	1.67E-01
C2H4	2.27E+01	3.81E+01	2.31E+01	2.8 E+01	6.94E+01	9.40E-01
C2H6	1.06E+00	1.91E+00	1.08E+00	3.0 E+01	3.24E+00	4.39E-02
C3H6	3.30E-01	8.32E-01	3.36E-01	4.2 E+01	1.01E+00	1.37E-02
C4H6	3.50E-01	1.13E+00	3.57E-01	5.2 E+01	1.07E+00	1.45E-02
C6H6		1.26E+01	2.74E+00	7.8 E+01	8.23E+00	1.11E-01
C8.5H8		1.08E+00	1.67E-01	1.10 E+02	5.00E-01	6.77E-03
C10H8		4.07E+00	5.40E-01	1.28 E+02	1.62E+00	2.19E-02
C12H8		1.34E+00	1.50E-01	1.52 E+02	4.49E-01	6.08E-03
C13H10		2.40E-01	2.46E-02	1.66 E+02	7.37E-02	9.97E-04
C14H10		6.10E-01	5.82E-02	1.78 E+02	1.75E-01	2.36E-03
C14H10		4.20E-01	4.01E-02	1.78 E+02	1.20E-01	1.63E-03
C16H10		7.30E-01	6.14E-02	2.02 E+02	1.84E-01	2.49E-03
C16H10		6.40E-01	5.38E-02	2.02 E+02	1.61E-01	2.19E-03
		5.82E-01	4.37E-02	2.26E+02	1.31E-01	1.78E-03
		7.70E-01	5.79E-02	2.26E+02	1.74E-01	2.35E-03
		2.50E-01	1.67E-02	2.54E+02	5.01E-02	6.79E-04
		1.43E-01	9.64E-03	2.52E+02	2.89E-02	3.92E-04
		7.63E-02	5.14E-03	2.52E+02	1.54E-02	2.09E-04
		7.63E-02	5.14E-03	2.52E+02	1.54E-02	2.09E-04
		4.77E-02	3.21E-03	2.52E+02	9.64E-03	1.31E-04
		5.44E-01	3.66E-02	2.52E+02	1.10E-01	1.49E-03
		1.85E-01	1.14E-02	2.76E+02	3.41E-02	4.62E-04
		3.50E-01	2.14E-02	2.78E+02	6.42E-02	8.69E-04
		5.43E-01	3.34E-02	2.76E+02	1.00E-01	1.36E-03
		3.26E-01	2.01E-02	2.76E+02	6.02E-02	8.15E-04
		2.06E-01	1.27E-02	2.76E+02	3.81E-02	5.16E-04
		4.02E-01	2.47E-02	2.76E+02	7.42E-02	1.00E-03
		2.41E-01	1.47E-02	2.78E+02	4.41E-02	5.97E-04
		8.91E-01	5.48E-02	2.76E+02	1.64E-01	2.23E-03
		4.25E-01	2.41E-02	3.00E+02	7.22E-02	9.78E-04
		1.21E-01	6.83E-03	3.02E+02	2.05E-02	2.77E-04
		5.79E-02	3.13E-03	3.14E+02	9.39E-03	1.27E-04
		1.15E-01	5.97E-03	3.26E+02	1.79E-02	2.43E-04
		4.33E-02	2.16E-03	3.40E+02	6.49E-03	8.78E-05
		7.08E-02	3.41E-03	3.52E+02	1.02E-02	1.39E-04
		2.45E-02	1.14E-03	3.66E+02	3.41E-03	4.62E-05
		2.90E-02	1.31E-03	3.76E+02	3.93E-03	5.32E-05
		1.31E-02	5.69E-04	3.90E+02	1.71E-03	2.31E-05

1.74E-02	7.40E-04	4.00E+02	2.22E-03	3.00E-05
5.85E-03	2.39E-04	4.16E+02	7.17E-04	9.71E-06
6.42E-03	2.56E-04	4.26E+02	7.68E-04	1.04E-05
3.92E-03	1.51E-04	4.40E+02	4.54E-04	6.15E-06
4.03E-03	1.51E-04	4.52E+02	4.54E-04	6.15E-06
2.80E-03	1.02E-04	4.64E+02	3.07E-04	4.16E-06
2.56E-03	9.10E-05	4.78E+02	2.73E-04	3.70E-06
1.64E-03	5.69E-05	4.90E+02	1.71E-04	2.31E-06
1.07E-03	3.62E-05	5.00E+02	1.09E-04	1.47E-06
7.04E-04	2.33E-05	5.14E+02	6.98E-05	9.46E-07
6.02E-04	1.94E-05	5.27E+02	5.82E-05	7.88E-07
4.67E-04	1.47E-05	5.38E+02	4.42E-05	5.99E-07
3.36E-04	1.03E-05	5.52E+02	3.10E-05	4.20E-07
3.23E-04	9.70E-06	5.65E+02	2.91E-05	3.94E-07
2.65E-04	7.76E-06	5.80E+02	2.33E-05	3.15E-07
1.63E-04	4.65E-06	5.94E+02	1.40E-05	1.89E-07

a, Calculation includes only gas phase data. B, Calculation includes all data.

Table A1-16: Data for the estimation of the mass transport of all observed molecular species to the reactor surface (Chapter 4) of a sample collected at a temperature of 1185 K, a pressure of 40 kPa and a residence time of 3.4 s.

mass (amu)	dif .coef. (m^2/s)	collision diameter (A)	density (g/ml)	k_d (s^{-1})	rate (mol $s^{-1}m^{-3}$)	rate (kg $s^{-1}M^{-2}$)
2.00E+00	6.41E-04	2.92E+00	-	9.23E+01	4.56E-01	9.12E-04
1.60E+01	2.39E-04	3.80E+00	-	3.45E+01	6.35E-02	1.02E-03
2.6E+01	1.94E-04	4.22E+00	-	2.79E+01	1.16E-02	3.02E-04
2.8 E+01	1.91E-04	4.23E+00	-	2.74E+01	6.44E-02	1.80E-03
3.0 E+01	1.80E-04	4.42E+00	-	2.59E+01	2.84E-03	8.52E-05
4.2 E+01	1.47E-04	5.06E+00	-	2.12E+01	7.24E-04	3.04E-05
5.2 E+01	1.34E-04	5.34E+00	-	1.93E+01	7.00E-04	3.78E-05
7.8 E+01	1.01E-04	6.56E+00	8.76E-01	1.45E+01	4.05E-03	3.16E-04
1.10 E+02	8.98E-05	7.05E+00	9.96E-01	1.29E+01	2.19E-04	2.41E-05
1.28 E+02	8.38E-05	7.38E+00	1.01E+00	1.21E+01	6.62E-04	8.48E-05
1.52 E+02	7.75E-05	7.78E+00	1.02E+00	1.12E+01	1.70E-04	2.58E-05
1.66 E+02	7.98E-05	7.59E+00	1.20E+00	1.15E+01	2.86E-05	4.76E-06
1.78 E+02	7.98E-05	7.57E+00	1.30E+00	1.15E+01	6.79E-05	1.21E-05
1.78 E+02	7.94E-05	7.61E+00	1.28E+00	1.14E+01	4.65E-05	8.28E-06
2.02 E+02	7.38E-05	8.00E+00	1.25E+00	1.06E+01	6.63E-05	1.34E-05
2.02 E+02	7.43E-05	7.96E+00	1.27E+00	1.07E+01	5.85E-05	1.18E-05
2.26E+02	7.28E-05	8.06E+00	1.37E+00	1.05E+01	4.66E-05	1.05E-05
2.26E+02	7.28E-05	8.06E+00	1.37E+00	1.05E+01	6.16E-05	1.39E-05
2.54E+02	6.88E-05	8.38E+00	1.37E+00	9.91E+00	1.68E-05	4.27E-06
2.52E+02	6.91E-05	8.36E+00	1.37E+00	9.95E+00	9.74E-06	2.46E-06
2.52E+02	6.91E-05	8.36E+00	1.37E+00	9.95E+00	5.20E-06	1.31E-06
2.52E+02	6.91E-05	8.36E+00	1.37E+00	9.95E+00	5.20E-06	1.31E-06
2.52E+02	6.91E-05	8.36E+00	1.37E+00	9.95E+00	3.25E-06	8.19E-07
2.52E+02	6.91E-05	8.36E+00	1.37E+00	9.95E+00	3.70E-05	9.33E-06
2.76E+02	6.61E-05	8.61E+00	1.37E+00	9.52E+00	1.10E-05	3.03E-06
2.78E+02	6.59E-05	8.63E+00	1.37E+00	9.48E+00	2.06E-05	5.73E-06
2.76E+02	6.61E-05	8.61E+00	1.37E+00	9.52E+00	3.23E-05	8.92E-06
2.76E+02	6.61E-05	8.61E+00	1.37E+00	9.52E+00	1.94E-05	5.35E-06
2.76E+02	6.61E-05	8.61E+00	1.37E+00	9.52E+00	1.23E-05	3.39E-06
2.76E+02	6.61E-05	8.61E+00	1.37E+00	9.52E+00	2.39E-05	6.60E-06
2.78E+02	6.59E-05	8.63E+00	1.37E+00	9.48E+00	1.42E-05	3.94E-06
2.76E+02	6.61E-05	8.61E+00	1.37E+00	9.52E+00	5.30E-05	1.46E-05
3.00E+02	6.35E-05	8.85E+00	1.37E+00	9.14E+00	2.23E-05	6.70E-06
3.02E+02	6.33E-05	8.87E+00	1.37E+00	9.11E+00	6.32E-06	1.91E-06
3.14E+02	6.21E-05	8.99E+00	1.37E+00	8.94E+00	2.84E-06	8.92E-07
3.26E+02	6.09E-05	9.10E+00	1.37E+00	8.77E+00	5.32E-06	1.74E-06
3.40E+02	5.97E-05	9.23E+00	1.37E+00	8.59E+00	1.89E-06	6.41E-07
3.52E+02	5.87E-05	9.34E+00	1.37E+00	8.45E+00	2.93E-06	1.03E-06
3.66E+02	5.75E-05	9.46E+00	1.37E+00	8.28E+00	9.57E-07	3.50E-07
3.76E+02	5.68E-05	9.55E+00	1.37E+00	8.17E+00	1.09E-06	4.08E-07

3.90E+02	5.57E-05	9.66E+00	1.37E+00	8.03E+00	4.64E-07	1.81E-07
4.00E+02	5.51E-05	9.75E+00	1.37E+00	7.93E+00	5.95E-07	2.38E-07
4.16E+02	5.40E-05	9.87E+00	1.37E+00	7.77E+00	1.89E-07	7.85E-08
4.26E+02	5.33E-05	9.95E+00	1.37E+00	7.68E+00	2.00E-07	8.51E-08
4.40E+02	5.25E-05	1.01E+01	1.37E+00	7.56E+00	1.16E-07	5.11E-08
4.52E+02	5.18E-05	1.02E+01	1.37E+00	7.46E+00	1.15E-07	5.18E-08
4.64E+02	5.11E-05	1.02E+01	1.37E+00	7.36E+00	7.66E-08	3.55E-08
4.78E+02	5.04E-05	1.03E+01	1.37E+00	7.25E+00	6.70E-08	3.20E-08
4.90E+02	4.97E-05	1.04E+01	1.37E+00	7.16E+00	4.14E-08	2.03E-08
5.00E+02	5.09E-05	1.03E+01	1.47E+00	7.33E+00	2.70E-08	1.35E-08
5.14E+02	5.02E-05	1.04E+01	1.47E+00	7.24E+00	1.71E-08	8.79E-09
5.27E+02	4.79E-05	1.07E+01	1.37E+00	6.90E+00	1.36E-08	7.17E-09
5.38E+02	4.74E-05	1.08E+01	1.37E+00	6.83E+00	1.02E-08	5.50E-09
5.52E+02	4.68E-05	1.09E+01	1.37E+00	6.74E+00	7.08E-09	3.91E-09
5.65E+02	4.63E-05	1.09E+01	1.37E+00	6.66E+00	6.56E-09	3.71E-09
5.80E+02	4.57E-05	1.10E+01	1.37E+00	6.58E+00	5.18E-09	3.01E-09
5.94E+02	4.51E-05	1.11E+01	1.37E+00	6.50E+00	3.07E-09	1.82E-09

Table A1-17: Raw data for laser attenuation as a function of reaction time for the pyrolysis of Ethane at 1185 K and 40 kPa (Chapter 5).

residence time (s)	% attenuation
17.4	36.249
17.4	37.641
10.4	39.965
10.4	40.42
7.2	39.553
7.2	39.730
7.2	37.913
7.2	38.650
4.8	30.995
4.8	34.054
4.8	33.034
4.8	32.254
2.4	15.495
2.4	14.755

Table A1-18: Distribution data from the image analysis of individual regions of the substrate (Chapter 6).

size (nm)	A	C	DE	F	B	B	D
15	31	4	10	47	12	10	114
20	44	4	2	38	14	12	114
25	37	4	11	48	7	6	113
30	54	4	8	35	10	7	118
35	38	7	9	38	8	6	106
40	43	4	9	20	7	4	87
45	42	1	2	12	9	4	70
50	48	5	4	8	4	14	83
55	23	4	4	10	2	3	46
60	22	3	3	4	7	3	42
65	23	1	0	4	7	12	47
70	10	3	1	2	8	4	28
75	22	6	1	3	6	9	47
80	9	5	2	2	5	10	33
85	10	4	4	3	6	2	29
90	9	4	2	1	8	4	28
95	4	4	4	0	5	9	26
100	6	3	3	0	1	3	16
105	6	1		1	2	4	14
110	5			0	3	2	10
115		2		0	6	4	12
120				0	9	1	10
125				0	8	2	10
130	2			0	3	1	6
135	1		2	0	4	1	8
140				0	3	1	4
145	1			0	0	1	2
150				0	1	0	1
155					2	1	3
160	1				1	0	2
165	1				2	0	3
170	1				1	1	3
175	1	1			1	1	4
180					0	0	0
185					2	1	3
190					0		0
195					0		0
200					3		3
205					1		1
210					1		1
215					0		0
220					0		0
225					0		0
230					1		1
235					2		2

Table A1-19: Data for the calculation of the rate of deposition onto the side of the dropped substrate described in Chapter 6 and the calculation of the number density in the gas phase assuming only diffusion onto the side of the substrate.

Freq.	d_i (nm)	m_{drop} (kg)	rate (kg $m^{-2}s^{-1}$)	rate (part $m^{-2}s^{-1}$)	D ($m^2\ s^{-1}$)	k_d (s^{-1})	Num. Den. (part. M^{-3})
80[a]	7.5	2.87E-22	2.8E-09	9.75E+12	1.9E-06	4.73E-05	2.06E+17
65[a]	12.5	1.33E-21	9.29E-09	6.99E+12	6.83E-07	1.71E-05	4.1E+17
47	20	3.65E-21	2.06E-08	5.65E+12	3.49E-07	8.72E-06	6.48E+17
38	25	7.75E-21	5.54E-08	7.14E+12	2.12E-07	5.28E-06	1.35E+18
48	30	1.41E-20	7.37E-08	5.21E+12	1.42E-07	3.54E-06	1.47E+18
35	35	2.34E-20	1.32E-07	5.65E+12	1.02E-07	2.54E-06	2.23E+18
38	40	3.59E-20	1.07E-07	2.98E+12	7.65E-08	1.91E-06	1.56E+18
20	45	5.22E-20	9.33E-08	1.79E+12	5.97E-08	1.49E-06	1.20E+18
12	50	7.29E-20	8.68E-08	1.19E+12	4.78E-08	1.19E-06	9.96E+17
8	55	9.84E-20	1.46E-07	1.49E+12	3.92E-08	9.8E-07	1.52E+18
10	60	1.29E-19	7.7E-08	5.95E+11	3.27E-08	8.18E-07	7.28E+17
4	65	1.66E-19	9.89E-08	5.95E+11	2.78E-08	6.93E-07	8.58E+17
4	70	2.09E-19	6.23E-08	2.98E+11	2.38E-08	5.95E-07	5.00E+17
2	75	2.59E-19	1.16E-07	4.46E+11	2.07E-08	5.17E-07	8.64E+17
3	80	3.17E-19	9.43E-08	2.98E+11	1.81E-08	4.53E-07	6.57E+17
2	85	3.82E-19	1.71E-07	4.46E+11	1.6E-08	4E-07	1.11E+18
3	90	4.56E-19	6.78E-08	1.49E+11	1.43E-08	3.57E-07	4.17E+17
1	95	5.38E-19	0	0	1.28E-08	3.19E-07	0
0	100	6.31E-19	0	0	1.15E-08	2.88E-07	0
0	105	7.33E-19	1.09E-07	1.49E+11	1.05E-08	2.61E-07	5.7E+17
1	110	8.45E-19	0	0	9.52E-08	2.38E-07	0

a. Calculated from the exponential fit provided in Chapter6.

Table A1-20: Data for the calculation of the number density from extinction experiments described in Chapter 6 using the distribution obtained by assuming only diffusion onto the side of the substrate and the refractive index for naphthalene.

Diam. (nm)	$Q_{1.58}$	x_i	N_i (part/m^3)
7.5	4.64E-07	0.011908140	4.71562E+15
12.5	3.58E-06	0.023684839	9.37920E+15
17.5	1.38E-05	0.037475356	1.48402E+16
22.5	3.77E-05	0.078131253	3.09400E+16
27.5	8.41E-05	0.084973542	3.36495E+16
32.5	0.000164	0.128657347	5.09483E+16
37.5	0.000291	0.090013494	3.56453E+16
42.5	0.000481	0.069263647	2.74284E+16
47.5	0.000752	0.057590905	2.28060E+16
52.5	0.001124	0.087806306	3.47713E+16
57.5	0.001619	0.042066142	1.66582E+16
62.5	0.002264	0.049623383	1.96509E+16
67.5	0.003085	0.028895591	1.14427E+16
72.5	0.004113	0.049925202	1.97704E+16
77.5	0.00538	0.03797374	1.50376E+16
82.5	0.006922	0.064447611	2.55213E+16
87.5	0.008775	0.024127973	9.55468E+15
92.5	0.01098	0	0
97.5	0.013578	0	0
102.5	0.016614	0.03295591	1.30505E+16

Table A1-21: Data for the calculation of the number density from extinction experiments described in Chapter 6 using the distribution obtained by assuming only diffusion onto the side of the substrate and the refractive index for soot.

Diam. (nm	Q_{soot}	x_i	Ni (part/m^3)
12.5	0.050186	0.023684839	1.52057E+14
17.5	0.070503	0.037475356	2.40592E+14
22.5	0.091071	0.078131253	5.01603E+14
27.5	0.111972	0.084973542	5.45530E+14
32.5	0.133288	0.128657347	8.25980E+14
37.5	0.155109	0.090013494	5.77887E+14
42.5	0.177527	0.069263647	4.44673E+14
47.5	0.200637	0.057590905	3.69734E+14
52.5	0.22454	0.087806306	5.63716E+14
57.5	0.249337	0.042066142	2.70065E+14
62.5	0.275135	0.049623383	3.18582E+14
67.5	0.302042	0.028895591	1.85510E+14
72.5	0.330167	0.049925202	3.20520E+14
77.5	0.359621	0.03797374	2.43791E+14
82.5	0.390516	0.064447611	4.13754E+14
87.5	0.422961	0.024127973	1.54902E+14
92.5	0.457063	0	0
97.5	0.492925	0	0
102.5	0.530644	0.03295591	2.11577E+14

Table A1-22: Raw data for deposition onto a metal substrate (Incoloy 800 HT) (Chapter 7) at a temperature of 1151 K, a pressure of 40 kPa and a flow rate of 26 sccm.

TIME (min.)	RATE (μg/min. cm^2)
10	13.278
20	8.714
30	8.720
40	8.710
50	7.054
60	4.979
80	4.564
100	5.062
120	4.888

Table A1-23: Partial pressures of methane, ethane, ethylene, acetylene and benzene in the product stream with a flow rate of 60 sccm and the carbon deposition rate in the center of the hot zone with a flow rate of 30 sccm as a function of temperature for 20 % mixtures of Ar, H_2S and H_2 with ethane at a pressure of 40 kPa and at 1113 K for 20 % mixtures of CO_2, C_3H_6, C_2H_2, and C_6H_6 with ethane. Errors are calculated from the standard deviation among 3 runs.

Product	Temperature	neat		Ar		H_2S		H_2	
methane	1151	40.51 ±	4.8	31.21 ±	1.2	35.90 ±	0.8	30.60 ±	4.6
	1113	25.80 ±	1.1	22.00 ±	1.4	22.50 ±	1.0	23.50 ±	0.5
	1053	12.10 ±	1.0	10.48 ±	0.2	9.944 ±	0.6	11.12 ±	0.8
ethane	1151	4.930 ±	0.6	3.720 ±	0.1	4.960 ±	0.2	4.540 ±	0.6
	1113	13.20 ±	0.1	10.70 ±	0.5	10.40 ±	0.5	12.70 ±	0.2
	1053	49.53 ±	0.2	39.78 ±	1.0	49.28 ±	2.5	41.31 ±	0.9
ethylene	1151	85.46 ±	6.6	73.36 ±	1.0	76.43 ±	2.6	73.78 ±	6.8
	1113	99.20 ±	2.2	86.80 ±	1.5	94.60 ±	3.0	85.90 ±	0.1
	1053	106.4 ±	4.0	96.64 ±	2.0	96.01 ±	0.1	95.98 ±	0.7
acetylene	1151	10.06 ±	1.0	8.560 ±	0.5	7.37 ±	0.7	7.500 ±	0.7
	1113	4.10 ±	0.1	3.700 ±	0.2	2.80 ±	0.2	2.890 ±	0.2
	1053	0.83 ±	0.1	0.762 ±	0.1	0.29 ±	0.1	0.641 ±	0.1
benzene	1151	8.16 ±	0.4	7.550 ±	0.4	7.18 ±	0.3	7.010 ±	0.5
	1113	3.18 ±	0.1	3.166 ±	0.1	2.12 ±	0.01	2.890 ±	0.2
	1053	1.01 ±	0.1	0.773 ±	0.05	0.30 ±	0.01	0.720 ±	0.01
R_c	1151	12.60 ±		10.27 ±	0.9	8.08 ±	0.50	8.750 ±	0.60
	1113	3.60 ±	0.2	3.200 ±	0.2	2.80 ±	0.10	2.800 ±	0.30
	1053	< 0.10		< 0.10		< 0.10		< 0.10	

Table A1-24: Partial pressures of methane, ethane, ethylene, acetylene and benzene in the product stream with a flow rate of 60 sccm and the carbon deposition rate in the center of the hot zone with a flow rate of 30 sccm for 20 % mixtures of CO_2, C_3H_6, C_2H_2, and C_6H_6 with ethane at a temperature of 1113 K and a pressure of 300 torr. Errors are calculated from the standard deviation among 3 runs.

Product	CO_2	C_3H_6	C_2H_2	C_6H_6
methane	23.53 ± 5.2	59.46 ± 7.8	33.4 ± 1.0	21.2 ± 0.2
ethane	11.42 ± 0.2	15.88 ± 2.5	16.5 ± 1.6	12.8 ± 0.2
ethylene	96.50 ± 8.0	115.4 ± 8.0	110 ± 4.0	100.5± 1.2
acetylene	2.905 ± 0.2	3.005 ± 0.3	4.9 ± 0.2	2.5 ± 0.2
benzene	3.005 ± 1.4	5.327 ± 1.8	6.7 ± 0.4	29.1 ± 1.0
Rc	2.500 ± 0.6	4.250 ± 0.9	8.1 ± 0.6	6.0 ± 0.6

Appendix 2

Code for the calculation of Q_e by Mie theory modified from reference 102:

```
      PROGRAM CALLBH
      IMPLICIT REAL*8 (A-H,O-Z)
      COMPLEX*16 REFREL,S1(200),S2(200)
      PII=3.14159265358979D0
      WRITE(*,11)
      REFMED=1.0D0
      REFRE=1.55D0
      REFIM=0.10D0
      REFREL=DCMPLX(REFRE,REFIM)/REFMED
      WRITE(*,12) REFMED,REFRE,REFIM
      RAD=1.0D0
      WAVEL=0.55D0
      X=2.D0*PII*RAD*REFMED/WAVEL
      WRITE(*,13) RAD,WAVEL
      WRITE(*,14) X

      NANG=11
      DANG=PII/(2.D0*DBLE(NANG-1))
      CALL BHMIE(X,REFREL,NANG,S1,S2,QEXT,QSCA,QBACK,G,QEXT1)
      SSA=QSCA/QEXT
      WRITE(*,65) QSCA,QEXT,QBACK
      WRITE(*,66) QEXT1,SSA,G
      WRITE(*,17)

      S11NOR=0.5D0*(ABS(S2(1))*ABS(S2(1))+
     1ABS(S1(1))*ABS(S1(1)))
      NAN=2*NANG-1
      DO 355 J=1,NAN
      AJ=J
      S11=0.5D0*ABS(S2(J))*ABS(S2(J))
      S11=S11+0.5D0*ABS(S1(J))*ABS(S1(J))
      S12=0.5D0*ABS(S2(J))*ABS(S2(J))
      S12=S12-0.5D0*ABS(S1(J))*ABS(S1(J))
      POL=-S12/S11
      S33=DBLE(S2(J)*CONJG(S1(J)))
      S33=S33/S11
      S34=IMAG(S2(J)*CONJG(S1(J)))
      S34=S34/S11
      S11=S11/S11NOR
      ANG=DANG*(AJ-1.D0)*57.2958D0
```

```
355  WRITE(*,75) ANG,S11,POL,S33,S34
65   FORMAT(//,1X,'QSC = ',E13.6,3X,'QEXT = ',E13.6,3X,
    2'QBACK = ',E13.6)
66   FORMAT(/,1X,'QEXT1 = ',E13.6,3X,'SSA = ',E13.6,3X,
    2'g = ',E13.6)
75   FORMAT(1X,F6.2,2X,E13.6,2X,E13.6,2X,E13.6,2X,E13.6)
11   FORMAT(/'SPHERE SCATTERING PROGRAM'//)
12   FORMAT(5X,'REFMED = ',F8.4,3X,'REFRE = ',E14.6,3X,
    3'REFIM = ',E14.6)
13   FORMAT(5X,'SPHERE RADIUS = ',F7.3,3X,'WAVELENGTH = ',F7.4)
14   FORMAT(5X,'SIZE PARAMETER = ',F8.3/)
17   FORMAT(//,2X,'ANGLE',7X,'S11',13X,'POL',13X,'S33',13X,'S34'//)
     STOP
     END

     SUBROUTINE
BHMIE(X,REFREL,NANG,S1,S2,QEXT,QSCA,QBACK,G,QEXT1)
     IMPLICIT REAL*8 (A-H,O-Z)
     DIMENSION AMU(100),THETA(100),PI(100),TAU(100),PI0(100),PI1(100)
     COMPLEX*16 D(3000),Y,REFREL,XI,XI0,XI1,AN,BN,S1(200),S2(200)
     COMPLEX*16 AN1,BN1
C    REAL*8 PSI0,PSI1,PSI,DN,DX
     PII=3.14159265358979D0
     DX=X
     Y=X*REFREL

     XSTOP=X+4.D0*X**0.3333+2.0D0
     NSTOP=XSTOP
     YMOD=ABS(Y)
     NMX=MAX(XSTOP,YMOD)+15
     DANG=PII/(2.0D0*DBLE(NANG-1))
     DO 555 J=1,NANG
     THETA(J)=(DBLE(J)-1.D0)*DANG
 555 AMU(J)=COS(THETA(J))

     D(NMX)=DCMPLX(0.0D0,0.0D0)
     NN=NMX-1
     DO 120 N=1,NN
     RN=NMX-N+1
 120 D(NMX-N)=(RN/Y)-(1.D0/(D(NMX-N+1)+RN/Y))
     DO 666 J=1,NANG
     PI0(J)=0.0D0
 666 PI1(J)=1.0D0
     NN=2*NANG-1
     DO 777 J=1,NN
```

```
    S1(J)=DCMPLX(0.0D0,0.0D0)
777  S2(J)=DCMPLX(0.0D0,0.0D0)

    PSI0=COS(DX)
    PSI1=SIN(DX)
    CHI0=-SIN(X)
    CHI1=COS(X)
    APSI0=PSI0
    APSI1=PSI1
    XI0=DCMPLX(APSI0,-CHI0)
    XI1=DCMPLX(APSI1,-CHI1)
    QSCA=0.0D0
    QEXT1=0.0D0
    G=0.0D0
    N=1
200  DN=N
    RN=N
    FN=(2.D0*RN+1.D0)/(RN*(RN+1.D0))
    PSI=(2.D0*DN-1.D0)*PSI1/DX-PSI0
    APSI=PSI
    CHI=(2.D0*RN-1.D0)*CHI1/X-CHI0
    XI=DCMPLX(APSI,-CHI)
    AN=(D(N)/REFREL+RN/X)*APSI - APSI1
    AN=AN/((D(N)/REFREL+RN/X)*XI-XI1)
    BN=(REFREL*D(N)+RN/X)*APSI - APSI1
    BN=BN/((REFREL*D(N)+RN/X)*XI - XI1)
    QSCA=QSCA+(2.D0*RN+1.D0)*(ABS(AN)*ABS(AN)+ABS(BN)*ABS(BN))
    QEXT1=QEXT1+(2.D0*RN+1.D0)*DBLE(AN+BN)

    IF (N .GT. 1) THEN
    GN1=(RN-1.D0)*(RN+1.D0)/RN
    GN2=(2.D0*RN-1.D0)/((RN-1.D0)*RN)
    G=G+GN1*DBLE(AN1*CONJG(AN)+BN1*CONJG(BN))
    G=G+GN2*DBLE(AN1*CONJG(BN1))
    END IF
    AN1=AN
    BN1=BN

    DO 789 J=1,NANG
    JJ=2*NANG-J
    PI(J)=PI1(J)
    TAU(J)=RN*AMU(J)*PI(J) - (RN+1.D0)*PI0(J)
    P=(-1.D0)**(N-1)
    S1(J)=S1(J)+FN*(AN*PI(J)+BN*TAU(J))
    T=(-1.D0)**N
```

```
      S2(J)=S2(J)+FN*(AN*TAU(J)+BN*PI(J))
      IF(J.EQ.JJ) GO TO 789
      S1(JJ)=S1(JJ) + FN*(AN*PI(J)*P+BN*TAU(J)*T)
      S2(JJ)=S2(JJ)+FN*(AN*TAU(J)*T+BN*PI(J)*P)
789   CONTINUE

      PSI0=PSI1
      PSI1=PSI
      APSI1=PSI1
      CHI0=CHI1
      CHI1=CHI
      XI1=DCMPLX(APSI1,-CHI1)
      N=N+1
      RN=N
      DO 999 J=1,NANG
      PI1(J)=((2.D0*RN-1.D0)/(RN-1.D0))*AMU(J)*PI(J)
      PI1(J)=PI1(J)-RN*PI0(J)/(RN-1.D0)
999   PI0(J)=PI(J)
      IF (N-1-NSTOP) 200,300,300
300   QSCA=(2.D0/(X*X))*QSCA
      QEXT1=(2.D0/(X*X))*QEXT1
      QEXT=(4.D0/(X*X))*DBLE(S1(1))
      QBACK=(4.D0/(X*X))*ABS(S1(2*NANG-1))*ABS(S1(2*NANG-1))
      G=(4.D0/(X*X))*G/QSCA
      RETURN
      END
```

Code for the calculation of the average coagulation coefficient using MATLAB:

```
[m,n] = size(x);

Kbar = 0;
for i = 1:m
        for j = 1:m
                Kij = pi*( x(i,1)*x(i,3) + x(i,1)*x(j,3) + x(j,1)*x(i,3) + x(j,1)*x(j,3) );
                Kbar = Kbar + Kij*x(i,2)*x(j,2);
        end %FOR j
end % FOR i

disp('Kbar value ...')
disp(Kbar)
```

References

1. Parker, W.G.; Wolfhard, H. G.; *J. Chem. Soc.*, 2038, (1950).

2. Grisdale, R. O.; *J. Appl. Phys.*, **24,** 1082, (1953).

3. Palmer, H.B.; Cullis, C.F.; *Chemistry and Physics of Carbon*, **1,** 265, (1965).

4. Krestinin, A.V.; *Twenty-Seventh Symposium (International) on Combustion, The Combustion Institute*, Pittsburgh, PA, 1557, (1998)

5. Prado, G.; Lahaye, J.; *Particulate Carbon Formation*, D.C. Siegla, G.W. Smith, Eds., Plenum, New York, 143, (1981).

6. Benish, T.G.; LaFleur, A. L.; Taghizadeh, K.; Howard, J. B.; *Twenty-Sixth Symposium (International) on Combustion*, The Combustion Institute, Pittsburgh, PA, 2319, (1996).

7. Kennedy, I. M.; *Prog. Energy Combust. Sci.*, **23**, 95, (1997).

8. Homann, K.H.; *Angew. Chem. Int. Ed.*, **37**, 2434, (1998).

9. Moriarty, N. W.; Brown, N. J.; Frenklach, M.; *J. Phys. Chem. A*, **103**, 7127, (1999).

10. Hinds, W. C.; *Aerosol Technology, Properties, Behaviour and Measurement of Airborne Particles*, Wiley, New York, 1-8, 233-257, 312-315, (1999).

11. Henning, T.; Salama, F.; *Science*, **282**, 2204, (1998).

12. Hiyashi, S.; Hisaeda, Y.; Asakuma, Y.; Aoki, H.; Miura, T.; Yano, H.; Sawa, Y.; *Combust. Flame*, **117**, 851, (1999).

13 Benzinger, W.; Huttinger, K. J.; *Carbon*, **37**, 931, (1999).

14. Feron, O.; Langlais, F.; Naslain, R.; Thebault, J.; *Carbon* , **37**, 1343, (1999).

15. Vandendorpe L.; *R and D Chemical and Petrochemical Research*, 23, Dec., (1996).

16. Bodke, A.S.; Olschki, D.A.; Schmidt, L.D.; Ranzi, E.; *Science*, **285**, 712, (1999).

17. *Nova Chemicals Corporation 1999 Annual Report*, 25, (1999).

18. Brown, D.E.; Clark, J.T.K.; Foster, A.I.; McCarrol, J.J.; Sims, M.L.; *Coke Formation on Metal Surfaces*, Ed. L.F. Albright and R.T.K. Baker, ACS Symposium Series 202, American Chemical Society, Washington, D.C., 23, (1982)

19. Sundaram, K.M.; VanDamme, P.S.; Froment, G.F.; *AIChE*, , **27**, 946-951, (1981).

20. Marec J.C.; Albright L.F.; *Coke formation on metal surfaces*, ACS symposium series 202, American Chemical Society, Washington, DC, 123 (1982).

21. McCarty, J.G.; Hou, P.Y.; Sheridan, D.; Wise, H.; *Coke Formation on Metal Surfaces*, Ed. L.F. Albright and R.T.K. Baker, ACS Symposium Series 202, American Chemical Society, Washington, D.C., 253, (1982).

22. Figueiredo, J.L.; *Materials and Corrosion*, **50**, 696,(1999).

23. Trimm, D.L.; *Pyrolysis: Industrial Theory and Practice*, Acedemic Press inc., 203-232, (1983).

24. Trimm, D.L.; *Catalysis Today*, **49**, 3, (1999).

25. Tong, Y.; *Symposium on the Chemistry of Coking, Desirable and Undesirable*, 216th National Meeting, American Chemical Society, Bosten, MA, 637-642, (1998).

26. Rahimi, P.; Ge,ntzis, T.; Fairbridge, C.; Khulbe, C.; *Symposium on the Chemistry of Coking, Desirable and Undesirable*, 216th National Meeting, American Chemical Society, Bosten, MA, 634-636, (1998).

27. Chan, G.; Inal, F.; Senkan, S.; *I and EC Research*, **37**, 3, 901, (1998).

28. Williamson, K.D.; Davis H.G.; *Proceedings of the Fourth World Petroleum Congress*, 308, (1973).

29. Pacey, P.D.; Wimalasena, J.H.; *J. Phys. Chem.*, 5657, **88**, (1984).

30. Pilling, M.J.; Smith, I.W.M.; *Modern Gas Kinetics, Theory, Experiment and Application*, Blackwell, Palo Alto, 316 (1987).

31. Roscoe, J.M.; Jayaweera, I.S.; Mackenzie, A.L.; Pacey, P.D.; *Int. J. Chem. Kin.*, **28**, 181, (1996).

32. Johnson, G. L.; Anderson, R. C.; *Proc. Conf. Carbon*, 5th, 395, (1961).

33. Fitzer, E.; Mueller, K.; Schaefer, W.; *Chemistry and Physics of Carbon*, **7**, 237, (1971).

34. Pierson, H.O.; Lieberman, M.L.; *Carbon*, **13**, 159, (1975).

35. Lahaye, J.; Prado, G.; *Petroleum Derived Carbons*, ACS symposium series 21, American Chemical Society, Washington, D.C., 335, (1976).

36. Lahaye, J.; Prado, G.; *Chemistry and Physics of Carbon*, **14**, 167, (1978).

37. Lahaye, J; Badie, P; Ducret, J.; *Carbon*, **17**, 175, (1979).

38. Chen, C.J.; Back M.H.; *Carbon*, **17**, 175, (1980).

39. Kaae, J.L.; *Carbon*, **23**, 6, 665, (1985).

40. Lucas, P.; Marchand A.; *Carbon*, **28**, 207, (1990).

41. Blekkan, E.A.; Myrstad, R.; Olsvik, O.; Rokstad, O.A.; *Carbon*, **30**, 665, (1992).

42. Murphy, D.B.; Carroll, R. W.; *Carbon*, **30**, 1, 47, (1992).

43. Pfefferle, L.D.; Bermudez, G.; Boyle, J.; *Soot Formation in Combustion*, H. Bockhorn, Ed. Springer-Verlag, Berlin, 26-48 (1994).

44. Dupel, P.; Bourrat, X; Pailler, R.; *Carbon*, 1995, **33**, 9, (1193).

45. Fau-Canillac, F.; Carrere, F.; Reynes, A.; Vahlas, C.; Maury, F.; *Journal De Physique II*, **5**, C5-89, (1995).

46. Benzinger, W.; Becker, A.; Huttinger, K.J.; *Carbon*, **34**, 957, (1996).

47. Shi, R.; Li, H.J.; Yang, Z.; Kang, M.K.; *Carbon*, **35**, 1789, (1997).

48. Murphy, D.B.; Carroll, R. W.; Klonowski, J.E.; *Carbon*, **35**, 1819, (1997).

49. Lewis, J.S.; Lackey, W.J.; Vaidyaraman, S.; *Carbon*, **35**, 103, (1997).

50. Becker, A.; Huttinger, K.J.; *Carbon*, **34**, 177 (1998).

51. Becker, A.; Huttinger, K.J.; *Carbon*, **34**, 201, (1998).

52. Becker, A.; Huttinger, K.J.; *Carbon*, **34**, 213, (1998).

53. Becker, A.; Huttinger, K.J.; *Carbon*, **34**, 225, (1998).

54. Bokros, J.C.; *Chemistry and Physics of Carbon*, **5**, 1, (1969).

55. Cullis, C.F.; *Petroleum Derived Carbons*, ACS symposium series 21, American Chemical Society, Washington, D.C., 348, (1976).

56. Tesnor, P.A.; *Chemistry and Physics of Carbon*, **19**, 65, (1984).

57. Frenklach, M.; Clary, D.W.; Gardiner, W.C.; Stein, S.E.; *Twentieth Symposium (international) on Combustion*, The Combustion Institute, 887, (1984).

58. Bohm, H.; Jander H.; *Phys. Chem. Chem.Phys.*, **1**, 3775, (1999).

59. Tesner, P.A.; Polyakova, M.M.; Mikheeva, S.S.; *Doklady Akademii Nauk SSSR*, **203**, 402, (1972).

60. Tesner, P.A.; Denisavich, E.V.; *Khimya Tverdogo Topliva*, **11**, 126, (1977).

61. Tesner, P.A.; Borodina, L.M.; *Khimya Tverdogo Topliva*, **17**, 157, (1983).

62. Tesner, P.A.; Aref ' eva, E.F.; *Fizika Goreniyai Vzryva*, **22**, 73, (1985).

63. Tesner, P.A.; Gorodetskii, A.E.; Borodina L.M., *Kinetikai Kataliz*, **23**, 990, (1982).

64. Tesner, P.A.; Denisevich, E.V.; *Khimya Tverdogo Topliva*, **8** , 142, (1974).

65. Tesner, P.A.; Gorodetski, A.E.; Denisevich E.V., *Khimya Tverdogo Topliva*, 107, **14**, (1980).

66. Tesner, P.A.; Rafal ' Kes, I.S.; Zhedeneva, O.B.; *Khimya Tverdogo Topliva*, 120, **18**, (1984).

67. Tesner, P.A.; Tekunova, T.V.; Snegireva, T.D.; *Khimya Tverdogo Topliva*, 114, **14**, (1980).

68. Gay, I. D.; Kistiakowsky, G. B.; Michael, J. V.; Niki, H.; *J. Chem. Phys.*, **43**, 1720, (1965).

69. Wu, C. H.; Singh, H. J.; Kern, R. D.; *Int. J. Chem. Kinet.*, **19**, 975, (1987).

70. Griesheimer, J.; Homann, K.-H.; Twenty-Seventh Symposium (International) on Combustion, The Combustion Institute, Pittsburgh, PA, 1753, (1998).

71. Frenklach, M.; Wang H. J.; *Phys. Chem.*, **98**, 11465, (1994).

72. Brooks, M. A.; Scott, L. T.; *J. Am. Chem. Soc.*, **121**, 5445 (1999).

73. LaFleur, A. L.; Taghizadeh, K.; Howard, J. B.; Anacleto, J. F.; Quilliam M. A.; *J. Amer. Soc. Mass Spectrom.* **7**, 276, (1996).

74. Munoz, R. H.; Charalampopoulos, T. T.; Twenty-Seventh Symposium (International) on Combustion, The Combustion Institute, Pittsburgh, PA, 1471, (1998).

75. Weilmunster, P.; Keller, A.; Homann K.-H.; *Combustion and Flame*, **116**, 62-83, (1999).

76. Mitchell, P.; Frenklach, M.;. *Twenty-Seventh Symposium (International) on Combustion*, The Combustion Institute, Pittsburgh, PA, 1507, (1998).

77. Richter, H.; Grieco, W. J.; Howard, J. B.; *Combust. Flame*, **119**, 1, (1999).

78. Frenklach, M.; Taki, S.; Durgaprasad, M.B.; Matula, R.A.; *Combustion and Flame*, **54**, 81, (1983).

79. Tanzawa, T.; Gardiner, W.C.; *J. Phys. Chem.*, **84**, 236, (1980).

80. Stein, S.E.; Fahr, A.; *J. Phys. Chem.*, **89**, 3714, (1985).

81. Frenklach, M.; *Twenty-second Symposium (International) on Combustion*, The Combustion Institute, 1075, (1988).

82. Frenklach, M.; Clary, D.W.; Gardiner, W.C.; Stein, S.E.; *Twenty-first Symposium (International) on Combustion*, The Combustion Institute, 1067, (1986).

83. Kern. R.D; Chen, H.; Kiefer, J.H.; Mudipalli, P.S.; *Combustion and Flame*, **177**, 100, (1995).

84. Miller, J.A.; Melius, C.F.; *Combustion and Flame*, **91**, 21, (1992).

85. Westmoreland, P.R.; Dean, M.A.; Howard, J.B.; Longwell, P.; *J. Phys., Chem.*, **93**, 8171, (1989).

86. Homann, K.H.; *Twentieth Symposium (International) on Combustion*, The Combustion Institute, 857-980, (1984).

87. Hanes, B.S.; Wagner, H. G.; *Prog. Combust. Sci.*, **7**, 229-273, (1981).

88. Bittner, J.D.; Howard, J.B.; *Particulate Carbon Formation*, D.C. Siegla, G.W. Smith, Eds., Plenum, New York, 109, (1981).

89. Anacleto, J.F.; Boyd, R.K.; Pleasance, S.; Quilliam, M.A.; Howard, J.B.; Lafleur, Y.; Makarovsky, T.; *Can. J. Chem.*, **70**, 2558-2568, (1992).

90. Anacleto, J.F.; Boyd, R.K.; Pleasance, S.; Quilliam, M.A.; Howard, J.B.; Lafleur, A.L.; Yadav, T.; *Rapid Commun. Mass. Spectrum*, **7**, 229-234, (1993).

91. Prado, G.; Jagoda, J.; Neoh, K.; Lahaye, J.; *Twenty-FourthSymposium International) on Combustion, The Combustion Institute*, Pittsburgh, PA, 1127, (1981).

92. Vander Wal, R. L.; Jensen, K. A.; Choi, M. Y.; *Combust. Flame*, **109**, 399, (1997).

93. Dobbins, R.A.; Megaridis, C.M.; *Langmuir*, **3**, 254-259, (1987).

94. Dobbins, R.A.; Subramaniasivam, H.; *Soot Formation in Combustion*, H. Bockhorn, Ed., Springer-Verlag, Berlin, 291-300, (1994).

95. Dobbins, R. A.; Fletcher, R. A.; Lu, W.; *Combust. Flame*, **100**, 301, (1995).

96. Fletcher, R. A.; Dobbins, R. A.; Lu, W.; *Anal. Chem.*, **70**, 2745, (1998).

97. Dobbins, R. A.; Fletcher, R. A.; Chang, H.C.; *Combust. Flame*, **115**, 285, (1998).

98. Graham, S. C.; *Proc. R. Soc. London A*, **377**, 119, (1981).

99. D'Alessio, A.; D'Anna, A.; D'Orsi, A.; Minutola, P.; Barbella, R.; Ciajolo, A.; *Twenty-Fourth Symposium (International) on Combustion, The Combustion Institute*, Pittsburgh, PA, 973, (1992).

100. Minutolo, P.; Gambi, G.; D'Alessio, A.; Carlucci, S.; *Atmospheric Environment* **33**, 2725, (1999).

101. Ciajolo, A.; Barbella, R.; Tregrossi, A.; Bonfanti, L.; *Twenty-Seventh Symposium (International) on Combustion*, The Combustion Institute, Pittsburgh, PA, 1481, (1998).

102. Tregrossi, A.; Ciajolo, A.; Barbella, R.; *Combust. Flame*, **117**, 553, (1999).

103. Homann, K.-H.; *Soot Formation in Combustion*, H. Bockhorn, Ed., Springer-Verlag, Berlin, 300, 301, (1994).

104. Schutzenberger, P.; Schutzenberger, L.C.R.; *Acad. Sci.*; **111**, 774, (1890).

105. Baker, R.T.K.; Harris, P.S.; *Chemistry and Physics of Carbon*, **14**, 83,(1978).

106. Rostrup-Nielsen, J.R.; Trimm, D.L.; *J. Catal.*, **48**, 155,(1977).

107. Terrones, M.; Hsu, W.K.; Kroto, H.W.; Walton, D.R.M.; *Top Curr. Chem. Berlin*, Springer-Verlag, Berlin, 189, (1999).

108. Rodriguez, N.M.; Kim, M.S.; Baker, R.T.K.; *J. Phys. Chem.*, **98**, 13108,(1994).

109. Rodriguez, N.M.; Chambers, A.; Baker, R.T.K.; *Langmuir*, **11**, 3862 (1995).

110. Chambers, A.; Rodriguez, N.M.; Baker, R.T.K.; *J. Phys. Chem.*, **99**, 10581 (1995).

111. Krishnankutty, N.; Rodriguez, N.M.; Baker, R.T.K.; *J. Catal.*, **158**, 217, (1996).

112. Park, C.; Rodriguez, N.M.; Baker, R.T.K.; *J. Catal.*, **169**, 212, (1997).

113. Chambers, A.; Baker, R.T.K.; *J. Phys. Chem. B*, **101**, 1621, (1997).

114. Rodriguez, N.M.; Kim, M.S.; Fortin, F.; Mochida, I.; Baker, R.T.K.; *Applied Catalysis*, **148**, 265, (1997).

115. Wu, X.Q.; Yang, Y.S.; He, W.Y.; Zhan, Q.; Hu, Z.Q.; *Journal of Materials Science*, **35**, 855, (2000).

116. Furue, H.; Pacey, P.D.; *J. Phys. Chem.*, **84**, 3139, (1980).

117. Feron, O.; Langlais, F.; Naslain, R.; *Carbon* , **37**, 1355, (1999).

118. Dimitrijevic, S.T.; Paterson, S.; Pacey, P.D., *J. Anal. Appl. Pyrolysis*, **53**, 107, (1999).

119. Biggs, W.R.; Fetzer, J.C.; *T.R.A.C.*, 196, **15**,4, (1996).

120. Lede, J. and Villermaux, J., *Journal De Chimie Physique*, 85, **71**, (1974).

121. Houzelot, J. L., Villermaux, J., *Chemical Engineering Science*, 1465, **32**, (1977).

122. Hirschfelder, J.O.; Curtiss, C.F.; Bird, R.B; *Molecular theory of gases and liquids*, John Wiley and Sons, Inc., NewYork, 14, (1964).

123. Berlman, I.B., Handbook of Fluorescence Spectra of Aromatic Molecules, Academic Press, New York, 108, (1971).

124. Acree, W. E., Tucker, S. A., Fetzer, J. C., *Polycyclic Aromatic Compounds*, 75, **2**, (1991).

125. D. Kim, M. Lee, Y. D. Suh, S. K. Kim, *J. Am. Chem. Soc.*, 4429, **114**, (1992).

126. Cosgrove, S. A., Guite, M. A., Burnell, T. B., Christensen, R. L., *J. Phys. Chem.*, 8118, **94**, (1990).

127. Sarofin, A. F., *Combust. Flame*, **100**:309 (1995).

128. Scion Image 3b, Scion Corporation, Frederick, MD, (1999).

129. Chang, H., Charalampopoulos, T.T., *Proc. R. Soc. Lond. A*, 577, **430**, (1990).

130. *Hand Book of Chemistry and Physics*, C-420, **61**, (1980).

131. Bohren, C.F., *Absorption and Scattering of Light by Small Particles*, New York, Wiley, (1983).

132. Filfil, R., Honers Thesis, Dalhousie Universiy, (1998).